Experimental investigation of the dynamics of S_1 benzene and the development of a new UV femtosecond pulse shaper

Dorian Sebastian Neville Parker

A thesis submitted for the degree of
Doctor of Philosophy

University College London
January 2009

PDF processed with CutePDF evaluation edition www.CutePDF.com

I, Dorian Parker confirm that the work presented in this thesis is my own. Where information has been derived from other sources, I confirm that this has been indicated in the thesis.

Acknowledgements

I would like to thank, firstly Professor Helen Fielding for her unwavering optimism and enthusiasm over the course of my time at UCL. She has always been positive and congratulatory on any progress made which I found a great source of encouragement. Secondly, I would like to thank Dr Russell Minns for his patience with my consistent stream of questions. Also for his almost super natural ability to make any machine or piece of equipment work, which when working with femtosecond lasers is no mean feat by far. I would also like to thank Abigail Nunn, whom I have spent many an hour in the laboratory working on the XFROG and UV pulse shaping experiment and losing our sanity together. I will not forget the many hours spent looking at a piece of paper for a spot of light that never came in our quest for $\tau = 0$. I would like to thank everyone else in the Fielding group at UCL whom have been both entertaining and helpful where possible. I must thank Jim in the work shop for building my pulse shaping apparatus and fulfilling his pledges of having it done yesterday. Also, thank you to everyone in tech support who have helped out over the years. Finally, I would like to thank all my family and my friends for their love and support throughout my studies.

Abstract

Experimental work into the molecular dynamics of excited state benzene and the development of a new ultraviolet pulse shaper are presented.

The non adiabatic non radiative decay process of benzene in its first excited has been determined using pump probe time resolved photoelectron spectroscopy. An ultrafast oscillation has been found at the onset of the channel 3 region which is attributed to intersystem crossing. Our experimental findings contribute to theoretical observations of a higher than previously expected spin orbit coupling in organic polyatomic molecules. The concluding mechanism is mediated by a doorway state and is supported by quantum dynamics simulations.

A pulse shaping capability has been developed to shape the output of a commercial optical parametric amplifier in the visible region using a reflective mode, folded, pulse shaping assembly employing a spatial light modulator. Second harmonic generation is used to frequency double the shaped visible pulse down to the deep ultraviolet energy region. A variety of pulse shapes have been synthesised and characterised using cross-correlation frequency resolved optical gating. The pulse shaping set-up benefits from wavelength tuneability allowing for its application to a range of coherent control schemes.

This thesis is based on the following publications

Chapter 3:

Ultrafast dynamics of the S_1 excited state of benzene

D.S.N. Parker, R.S. Minns, T.J. Penfold, G.A. Worth and H.H. Fielding

Chemical Physics Letters 469 (2009) 43-47

Chapter 4:

Frequency doubling and Fourier domain shaping the output of a femtosecond optical parametric amplifier: easy access to tuneable femtosecond pulse shapes in the deep ultraviolet

D.S.N. Parker, A.D. Nunn, R.S. Minns and H.H. Fielding

Applied Physics B (2009) 94: 181-186

Contents

Figures

Chapter 1:

Chapter 2:

Chapter 3:

Chapter 4:

Chapter 5:

Tables

Chapter 1

Introduction

This chapter provides an introduction to progress in improving our understanding and controlling photochemical and photophysical processes. It begins with a discussion of some of the core concepts of organic photochemistry and leads onto the historical development of following chemical reactions in real time. It then reviews some interesting and important developments in the field of time-resolved photoelectron spectroscopy. The focus is then shifted from observation of excited state processes to their control, with a brief discussion on the approaches to pulse shaping and a description of some examples of coherent control.

1.1 Organic photochemistry

Photochemistry is concerned with the interaction of light with atoms or molecules to cause a chemical reaction. This area of science encapsulates some of the most important processes in nature like photosynthesis and vision. The study of the nature of light and light matter interaction brought about what is arguably one of the most important of all scientific developments in history - quantum mechanics. This theory revolutionised scientific knowledge propelling our understanding down to the atomic and molecular level from the shackles of Newtonian physics.

1.1.1 Jablonski diagram

The processes that are available to an atom or molecule when it absorbs light can be illustrated in a Jablonski diagram as shown in figure 1. The diagram shows the electronic states of an arbitrary molecule and the transitions which can occur between them. The states are arranged vertically by energy and grouped horizontally by spin multiplicity. Initially, a molecule will be in its lowest energy state, its ground state, assuming no prior excitation. From here the molecule can absorb a quantum of light and become excited resulting in an electron in the molecule moving from its highest occupied molecular orbital to its lowest unoccupied molecular orbital. The movement of the electron allows the molecule to absorb the energy of the photon by moving from its lowest energy position to a higher energy orbital and storing it as a potential. The nuclei feel a new set of attractions with a new charge distribution of the electronic orbitals and start to move to take up the lowest energy geometry. The new position of the electron and its new potential energy can bring about a change in the molecular structure, which is classified as a photochemical reaction. Unimolecular reactions of this type are in essence the simplest of all reactions. Reactions resulting in the excited state population moving back to the ground state are photophysical reactions and are also important mechanisms in the dissipation of energy, for example, from harmful ultraviolet radiation in DNA. Since the reactions are mediated by light it provides experimentalists with the opportunity to harness the properties of the light, for example the frequency composition, absorbed and emitted in these reactions to study them on a molecular level. This general field of spectroscopy has now a great range of techniques in its arsenal to observe and help elucidate many fundamental reactions, some of which shall be covered in this thesis.

From the singlet excited state (S_1) the molecule can undertake a radiative decay route back to the ground state through the emission of a photon by fluorescence. These types of processes commonly occur on the nanosecond (ns) timescale and when in the liquid phase always from the lowest vibrational state of the excited state (Kashas rule). The singlet excited state population may also return to the ground state in a non radiative process through an internal conversion. Internal conversions occur through an adiabatic route in an avoided crossing or through a non adiabatic route in a surface crossing. A surface crossing is termed a conical intersection, and has been found to be responsible for excited state decay on ultrafast femtosecond timescales. They will be more thoroughly discussed in a following section. Movement of the excited state population to a triplet state is termed an intersystem crossing (ISC) and involves a change in spin multiplicity. This process involves a surface crossing and is dependant on the spin-orbit coupling between the two states. Timescales for intersystem crossing are generally between nano- and milli- seconds, although ultrafast ISC has been recently observed[1,20]. Generally, spin-orbit coupling can be increased by the presence of a heavy atom[46]. From the excited triplet state the population can decay to the ground singlet state in a radiative process of phosphorescence on a second timescale or in a non radiative process through a surface crossing between the triplet and singlet states. The timescale is long due to the transition being electronically forbidden.

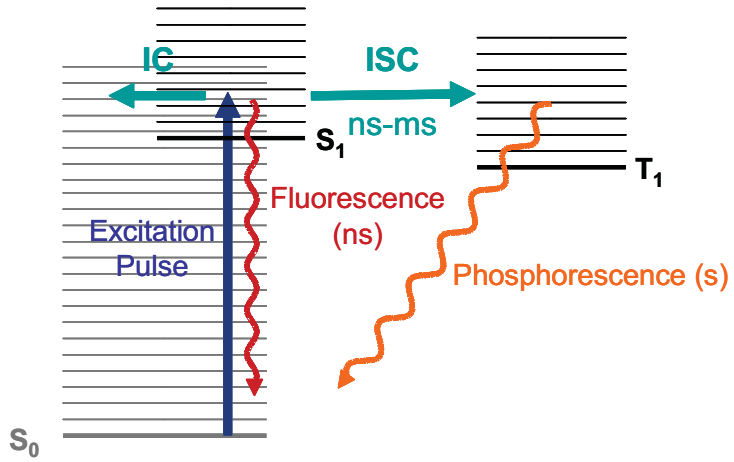

Figure 1: Jablonski diagram illustrating the photophysical and photochemical processes available to a molecule after excitation. The diagram is plotted as a function of spin multiplicity and potential energy. Once a photon is absorbed exciting the ground state population to the first excited state the molecule can: Fluoresce on a nanosecond time scale by emission of a photon, returning the population to the ground state; undergo internal conversion back to the ground state which is generally an ultrafast process; undergo intersystem crossing to the triplet state in nano to milliseconds from here the molecule can phosphoresce in seconds back to the singlet ground state.

These processes account for all the mechanisms available to an isolated molecule moving from one electronic state or spin multiplicity to another. The molecule can also react to form a product. Within an electronic state the molecule can have its population in specific vibrationally excited states. This depends on the wavelength of light whether it is resonant with a transition to a vibrationally excited state. Specifically, if there is a good Franck-Condon overlap with that state. Vibrational states can also overlap and couple with one another which allows the energy be dissipated into other vibrational modes.

1.1.2 Potential energy surface

The Jablonski diagram only views the processes undertaken by the molecule in terms of energy with no indication of how the geometry is altered during this process. A potential energy surface for a molecule is the plot of how the energy varies with co-ordinates. So for a system with N atoms the potential energy is a function of $3N$-6 internal or $3N$ Cartesian co-ordinates. This means for all but the simplest atoms the potential energy is a complicated multidimensional function of the co-ordinates.

The Born Oppenheimer approximation, in which the electron can be thought of as moving instantaneously compared to the nuclei, is used to calculate the potential energies of the molecule to form the surface. This follows from the fact that the masses of the nuclei and electrons are very different. Theoretically this allows for the electronic and nuclear parts of the wave function to be separated. The Born Oppenheimer approximation does however break down in certain areas of the potential energy surface, for example, at a conical intersection.

Each point on the surface corresponds to a different structure. For a molecule with more than two coordinates a surface cannot be plotted in 3D. To overcome this key coordinates need to be picked that are the most important in the process under investigation. Since it is impossible to plot all the coordinates at once, the axes for a potential energy surface will correspond to key changes to the molecules bond lengths or orientation. The third axis, the height corresponds to the energy, of whatever orientation the other two axes specify.

This representation can illustrate in a chemically intuitive fashion how the geometry of a molecule is altered over time, its molecular dynamics. The initial structure of a molecule will be an arbitrary configuration with standard bond lengths and angles on the ground state. The structure will be stable and so exist in a 'well' with a minimum associated with the lowest energy structure. From here excitation of the ground state population can be caused by an ultrashort pulse to create a wave packet on the excited state surface. The movement of a wave packet created on the potential can be thought of like a marble rolling over a surface. The trajectory of the wave packet will depend on the surface topology and the vibrational modes excited by the specific frequencies of the pulse. Features on the potential energy surface, termed critical points, can be calculated using quantum mechanical methods. These included minima, transition states and surface crossings.

1.1.3 Conical intersections

A conical intersection of two potential energy surfaces of the same spatial and spin symmetries is the set of molecular geometry points where the two potential energy surfaces are degenerate (intersect). Conical intersections (CI) are ubiquitous in chemical systems and provide a common mechanism for de-excitation from the lowest excited states in polyatomics. When a molecular excited state wave packet reaches a conical intersection large vibronic coupling induces a non-radiative transition between the two states allowing the population on the upper state to transfer to the lower state. In a polyatomic molecule, two electronic states of the same symmetry are allowed to cross at a CI (a real surface crossing). Radiationless decay from the upper to the lower intersecting state occurs within a vibrational period when the system "travels" in the vicinity of such intersection points. In the gas phase, i.e. an isolated system, movement of the molecular wave packet through a CI is described as a non adiabatic event, in which case the high electronic energy of the excited state is redistributed into other degrees of freedom, namely vibrational energy to obey the law of conservation of energy.

In a system with n coordinates, degenerate points lie in what is called the intersection space, or seam, the dimensionality of which is N-2. For a conical intersection, the remaining two dimensions that lift the energetic degeneracy of the system form the

branching space. The two-degeneracy lifting coordinates are the gradient difference, x_1, and the interstate coupling, x_2. When the potential energy surface is plotted along these two coordinates it forms two cones, of which the upper is inverted, and where they cross is the conical intersection. The remaining N-2 coordinates in this representation form a hyperline, the intersecting space, which consists of an infinite number of crossing points. The shape of the conical intersection can vary, but generally occurs in two distinct forms, as either a sloped intersection or a peaked intersection. The shape of the intersection and the trajectory of the wave packet into it will dictate what area of the lower state the wave packet will access and therefore the molecular dynamics. A conical intersection in a polyatomic has been shown below:

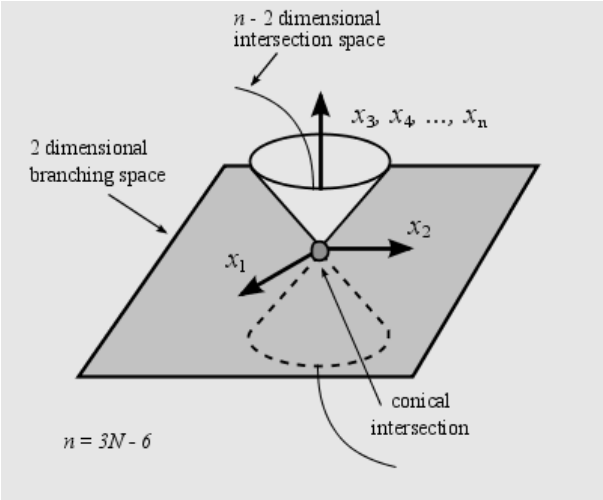

Figure 2: Conical intersection. In a polyatomic molecule two potential energy surfaces are allowed to cross along a $(3N-8)$-dimensional subspace of the $(3N-6)$-dimensional nuclear coordinate space (the intersection space) even if they have the same spatial/spin symmetry. Each point of the intersection space corresponds to a conical intersection. If the energy is plotted against two special internal geometrical coordinates, $\boldsymbol{x}_1$ and $\boldsymbol{x}_2$, which define the so-called branching plane, the potential energy surface would have the form of a double cone in the region surrounding the degeneracy. In the remaining $(3N-8)$ directions, the energies of the ground and excited state remain degenerate; movement in the branching plane lifts the degeneracy.

1.1.4 From kinetics to dynamics

In 1889, Arrhenius gave the seminal description of the change in rates of chemical reactions, the dependence of the rate constant k of chemical reactions on the temperature T, (in kelvin) and activation energy E_a , as:

$$k = A\exp(-E_a / RT) \tag{1.1}$$

where *A* is the pre-exponential factor, *R* is the gas constant. This description is remarkably accurate for values of T that are above 20 K but is limited to an average of all molecular reactions in the ensemble measured. When T is very low the quantised nature of the molecule under study becomes into play. Equation (1.1) gives no insight into how the molecules approach, collide, exchange energy, break or make bonds, or how they may separate into products. Molecular dynamics has the aim to answer these elementary questions. The first approach to answering some of these questions used a quantum mechanical theoretical method developed by Heitler and London[41] to describe the potential energy surface of H_3 in terms of the Coulombic and exchange energies of the diatomic pairs. Eyring and Polanyi[33], in 1931, used this equation to obtain the first potential energy surface using a semiempirical calculation which described the reaction of H + H_2. They were able to show how the reactants formed the products on a potential energy surface by illustrating the trajectory of the reactants and products on in it as a function of time. In 1935, Eyring, and, separately, Polanyi and Evans re-formulated the Arrhenius equation giving an expression of the pre-exponential factor as part of their transition state theory (TST)[42, 43]. TST gave a structure to the intermediate step in a chemical reaction and also its first timescale. The transition state was viewed as any structure other than the reactant or product. The equation gave a lower limit to the time taken through the transition state which as a frequency came to $\sim 6 \times 10^{12}$ s^{-1} which corresponded 170 fs.

1.1.5 A history of short timescales

The observation of a fast event is dictated by the speed of the technique by which it is imaged. In 1877, Edweard Muybridge used a series of cameras to photograph a horse galloping in order to answer the question whether all four hooves left the ground at the same time. Unknowingly, it could be said that he was the first to conduct a pump-probe experiment to answer a question on a process that was too fast for vision to discern. This technique was picked up in 1950, where the first pump-probe experiments involving chemical reaction kinetics were made[44, 45]. The time delay between the pump and probe is altered through the introduction of a change in path length between the pump and probe beams. Flash photolysis experiments were undertaken by Norrish and Porter in which an intense burst of light from a flash lamp

initiated a chemical reaction to produce radicals in the pump step[34]. The spectrum of the radicals was then recorded using a second pulse of light in the probe step. They were able to gain kinetic information on the reactions undertaken by short lived radicals down to the microsecond time scale. For example information was gained on ClO, I_2 and formation of halogenated cyclopentadienyl radicals. For this contribution Norrish and Porter and separately Eigen, shared the 1967 Nobel Prize. This marked the onset of ever shortening timescales in which the time resolution of the dynamics they could view was dictated by the duration of the flashes of light which could be produced. The 1960's saw the invention of the pulsed laser which gave the leap into the nanosecond and later picosecond regime. From here the focus moved to non radiative processes where timescales for internal conversion, intersystem crossing and orientation relaxations were obtained.

The field of study concerned with understanding how molecules change as a function of time can be generally termed as molecular dynamics. Conventional spectroscopy, which occupies the frequency domain strictly, was being revolutionised with the development of lasers in the 1960's, and allowed for the further understanding of molecular dynamics by rationalising the spectroscopy available to molecules. Nanosecond resolution enabled the observation of firstly intersystem crossing and later rotational motion but it was not until the femtosecond timescale was reached in the 1980's that vibrational motion could be resolved. In 1999, Ahmed Zewail[2] received a Nobel Prize for his work in propelling the field of molecular dynamics into the femtosecond realm from its realisation in the 1980's. In his early work he was able to observe the process of intramolecular vibrational energy redistribution in anthracene[3] using the recently developed molecular beam techniques. He and co-workers observed the excited state population of NaI oscillating backwards and forwards with a defined period on a picosecond timescale. This brought about the evidence that the induced vibrations by a coherent pulsed laser source were themselves also coherent. The concept of quantum coherence was now experimentally verified and ideas about how the phase of the excitation pulse could be manipulated to alter the vibrational make up of a non stationary superposition of states were seeded.

The year of 1987 saw the first observation of the change in molecular structure in a chemical reaction as a function of time, specifically the breaking of a bond, using

lasers with femtosecond resolution. The photodissociation reaction of NaI was observed and from this confirmed a range of concepts: that the wave packet was localised in space, that the wave packet remained localised and coherent over time, that the wave packet could be thought of as a marble rolling on a potential energy surface along a reaction co-ordinate from reactant to product passing through the TST[3]. This set the precedent for many molecular dynamics experiments and a variety of techniques were developed to this end, such as resonance enhanced fluorescence spectroscopy and ion – time of flight techniques.

1.2 Time-resolved photoelectron spectroscopy

1.2.1 Introduction

The advent of femtosecond time-scale laser pulses has enabled the real time observation of chemical dynamics. Since then a flurry of research has been undertaken using a variety of techniques, such as photoionisation, laser-induced fluorescence and coherent anti-Stokes Raman spectroscopy. Gas-phase time resolved photoelectron spectroscopy (TRPES) emerged from the available techniques as a particularly versatile and sensitive technique. Its contributions to photochemistry and photophysics, and more recently photobiology have been summarised in a number of review articles[4-8]. TRPES utilises the pump-probe method where the dynamical process to be studied is initiated with a pump pulse which is then imaged *via* ionisation at certain times after its inception with a probe pulse.

The excitation by the pump pulse creates a non stationary state, or wave packet (see section 1.2.3), which evolves over the excited potential energy surface. By detecting, or rather probing, the wave packet at different stages along its reaction coordinate, a picture can be built up of the excited state potential energy surface and the chemical dynamics unravelled. . The probe pulse ionises the species under investigation and the photoelectrons emitted are collected and analysed. A variety of techniques exist to collect photoelectrons, namely time-of-flight tubes, magnetic bottle spectrometers, and photoelectron imaging. The order in which they have been listed indicates the order of their introduction chronologically. At the heart of excited state chemical dynamics are non-adiabatic processes which dominate the ultrafast photochemistry of

molecules including organic polyatomics, these include internal conversion and intersystem crossing. TRPES has been successfully used to decipher which mechanisms are responsible for characteristic ultrafast photochemistry.

A variety of probes have been used to detect wave packets. In the condensed phase, transient absorption and nonlinear wave-mixing techniques have been used; however, these are impractical in gas phase experiments due to low detection yields. Instead laser induced fluorescence and resonant multiphoton ionisation have been preferred. Multiphoton ionisation techniques suffer from low photoelectron yields when an intermediate state is not available for ionisation from, this is further hampered by the fact that increasing laser intensity can lead to unwanted strong field effects. Use of a resonant state also somewhat restricts viewing the excited state dynamics when a large change in energy is undertaken for example in a non adiabatic process. The resonance conditions will therefore change and could require re-tuning of the probe pulse to view the rest of the reaction coordinate.

These techniques can suffer from a restricted final state in which the probe must be resonant with an electronic transition in the target molecule to yield its observable. In the case of laser induced fluorescence segments of the reaction coordinate can have a poor fluorescence yield causing dark areas. For resonant multiphoton ionisation the ionising photons may not be resonant on every part of the reaction coordinate and so must be tuned. This means at a particular probe wave length there are “dark” areas of the wave packets evolution over the potential energy surface. To improve on this a probe is required that is able to ionise along the entire reaction co-ordinate and that is not restricted to a specific final state. Time resolved photoelectron spectroscopy benefits from being able to ionise along the entire reaction coordinate as long as a good Franck Condon overlap exists with the ionisation continuum

In the work presented in this thesis TRPES is used to study the excited state intramolecular dynamical processes in an isolated gas phase polyatomic molecule, specifically benzene. The probe in this case has a suitably high energy to cause ionization of the excited molecule with one photon, the ejected photoelectrons are collected and their kinetic energies are measured. This removes the resonance conditions potentially allowing the entire reaction coordinate to be accessed *via* the

probe. Ionisation has the advantages of: (1) charged particle detection is extremely sensitive; (2) Single photon ionisation is always an allowed process with relaxed selection rules, there are no 'dark' states; (3) Information can be gathered by analysing the outgoing electron in terms of their kinetic energy and angular distribution; (4) High order multi-photon processes which commonly plague femtosecond studies can be detected through fitting of the photoelectron image with the correct the Legendre polynomials if not saturated; (5) The final state in an ionization process is often a stable cation which can be characterized independently by high resolution photoelectron or infrared spectroscopy or by computational methods[9] .

In TRPES a fundamental concept is that of the Koopmans picture - that upon ionisation an outer valence electron is removed from the molecule with no simultaneous electronic re-arrangement of the ion core. This means TRPES is sensitive to both electronic configurations and vibrational dynamics of molecules making it an optimum technique for studying non-adiabatic processes. TRPES is, however, restricted from viewing the reaction coordinate on the ground state with high resolution. This is due in part to the requirement of high energy photons required to ionise the ground state which in the case of benzene is ~9 eV. To obtain this energy photon would require a vacuum ultraviolet (VUV) source which currently is not commercially available but can be built. As well as this the wave packet upon accessing the ground state would be very vibrationally hot requiring high resolution detection to resolve the high density of states that would be populated. For this reason the wave packet would also likely fragment, causing additional signals to be obtained from the fragments.

The generality of the Koopmans picture - that the structure of the cation ionisation continuum of a molecule closely reflects that of the neutral molecule before ionisation - was consolidated theoretically by Domcke et al in 1991[10, 11]. It was illustrated that if, upon removal of a single active outer electron, a probed electronic configuration correlates well with the ground electronic configuration of the continuum then the photoionisation probability is generally higher than if it does not. This implies that the electronic structure of the continuum can be used as an uninhibited probe of the evolving electronic configuration in the neutral state.

1.2.2 Theory of TRPES

Wave packets are defined as coherent superpositions of molecular eigenstates $|N\rangle$. Eigenstates themselves are stationary since they are solutions of the time-independent Schrödinger equation. The non stationary nature of a wave packet comes from the inclusion of the quantum mechanical energy phase factors $e^{-iE_N t/\hbar}$ associated with the eigenstates in the superposition (refer to equation 1.2). TRPES experiments aim to create and detect these wave packets using the pump-probe method as described above.

Pump-probe experiments consist of three parts: (i) preparation of the excited state wave packet; (ii) the dynamical evolution of the wave packet; (iii) the probing of the wave packet. This is illustrated in figure 3. The full range of excited eigenstates created by the broad bandwidth pump pulse are shown in this figure (dark arrows) but in the following description of the relationship between the three steps only two states shall be considered $|N\rangle$ and $|M\rangle$ for simplicity. Also to note is that the final state in this figure is reached by a broad bandwidth probe pulse (light arrows) which would overlap all excited eigenstates with a particular final state. What is not shown, for simplicity, is that other final states would also have an overlap with some or all of the excited and probed eigenstates. The following description focuses on one final state which includes the interference experienced between the coherent transitions ending in the same final state.

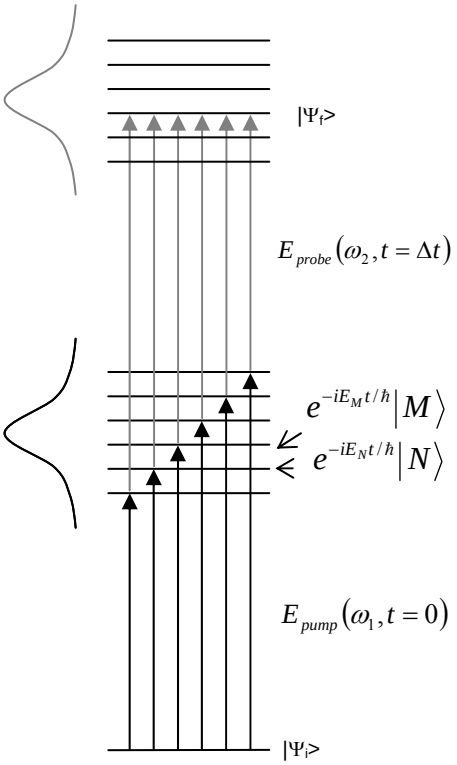

Figure 3: Preparation, evolution and projection onto a final state of the excited state wave packet. The pump pulse creates a non-stationary superposition of excited eigenstates, in this case two have been illustrated, $|M\rangle$ and $|N\rangle$ out of the initial state $|\Psi_i\rangle$. The difference in the quantum mechanical energy phase factors $e^{-iE_N t/\hbar}$ between the eigenstates in the superposition determines the wave packets evolution over the potential energy surface. Once the pump pulse is over the probe pulse projects the wave packet onto a final state $|\Psi_f\rangle$.

From a frequency domain perspective, the final state reached in the pump probe experiment is caused by coherent two photon transitions from the pump (dark arrows) and probe (light arrows) photons. The signal measured is proportional to the population in the final state at the end of the two pulse sequence. The transition probability to the final state is calculated by squaring the sum of all these two photon transitions. The signal is affected by interferences between the two photon transitions which manifest themselves as modulations. The amplitudes and initial phases of the set of the initially prepared excited eigenstates are determined by the amplitudes and phases of the pump laser field frequencies and the transition dipole amplitudes between the initial state and the excited state of interest. The characteristic modulations in the signal are determined by the phase relationship between the eigenstates. The excited state wave packet created by the pump pulse is given by:

$$|\Psi(t)>=\sum_N A_N e^{-iE_N t/\hbar}\,|N> \qquad (1.2)$$

In (1.2), the phase and amplitude of the molecular eigenstates $|N\rangle$ are contained in the complex coefficients A_N, and the E_N are the excited state eigenenergies. After the pump pulse has created the excited state wave packet, it is free to evolve depending

on the relative energy phase factors in the superposition. The wave packet will move out from the Franck Condon region and into another area of the surface marking the onset of the chemical dynamics. After a time interval, Δt, from the wave packets inception, in which time it evolves, the probe pulse interacts with it and projects it onto the final state Ψ_f. The final state represents the viewing window used to observe the excited state wave packet. The difference between the signals at these time intervals builds up a picture of how the wave packet is evolving over the excited state potential energy surface.

Each photoelectron spectrum obtained using photoelectron imaging is resolved in energy and is referred to as a differential signal. Where, conversely, for a detection technique such as ion yield or fluorescence spectroscopy, the total signal, $S(\Delta t)$, corresponds to the sum of all energetically allowed final states $\Sigma S_f(\Delta t)$ and is referred to as a integral detection technique. The set of photoelectron spectra obtained by the pump-probe photoelectron imaging process thus gives the time dependence of the differential signal, $S_f(\Delta t)$. The time dependence of the differential signal, $S_f(\Delta t)$ obtained from TRPES, for projection onto the final state is:

$$S_f(t) = |< \Psi_f \mid E_{probe}(\omega).d \mid \Psi(t) >|^2 = \left| \sum_N B_N e^{-iE_N t/\hbar} \right|^2 \tag{1.3}$$

In (1.3) the complex coefficients B_N contain the wavepacket amplitudes A_N and the complex probe transition dipole matrix elements, d. The transition dipole matrix elements connect each eigenstate in the superposition $|N\rangle$ to the final state. The complex coefficients are shown below:

$$B_N = A_N < \Psi_f \mid E_{probe}(\omega).d \mid N > . \tag{1.4}$$

Equation (1.3) can be re-written, excluding the imaginary part, for a wave packet comprising two eigenstates $|N\rangle$ and $|M\rangle$ as:

$$S_f(t) = 2\sum_N \sum_{M \le N} |B_N||B_M| \cos\left[(E_N - E_M)t/\hbar + \Phi_{NM}\right] \tag{1.5}$$

The phase factor Φ_{NM} contains the differences in phase of the molecular eigenstates and the phase difference of the probe transition dipole matrix elements connecting states $|N\rangle$ and $|M\rangle$ to the final state. The differential signal, $S_f(t)$, contains in it detailed information about the final state. It is determined by the coherent sum over all two photon transition amplitudes and contains the interferences between any degenerate two photon transitions. The modulations contained in the signal at frequencies $(E_n - E_m)/\hbar$ relate to the set of level spacings in the superposition. When the time domain signal is Fourier transformed to the frequency domain, the frequencies obtained indicate what the set of levels spacings are in the excited state. This gives the relationship between the wave packet dynamics and the observed pump probe signal. The Fourier amplitudes for each frequency correspond to the overlap of each excited state eigenfunction with a specific final state. Each final state will give a specific signal, S_f from having unique transition dipole moment matrix elements with the eigenstates $|N\rangle$ and $|M\rangle$ that constitute the wave packet. So the choice of probe and in turn the choice of final state will determine what information is gleaned from the excited state wave packet. This also allows the experimentalist to select areas of dynamics of interest.

1.2.3 Photoelectron energy relation to ion energy distribution

An isolated molecule rests in the ground state, $\widetilde{X}$, with a distribution of vibrational states, v', as represented by $p(E)$ which possess energies $E^X(v')$. An example distribution is shown in the bottom left of figure 4. The ground state population is defined in this summary to be on a vibrational state with internal energy E_{v0}. A broad bandwidth femtosecond pulse excites the ground state population to a number of vibrational levels in $\widetilde{B}$, to form a non stationary superposition of states with energy, $E_B(v')$. The energy width of $E_B(v')$ is characterised by the frequency width of the laser pulse.

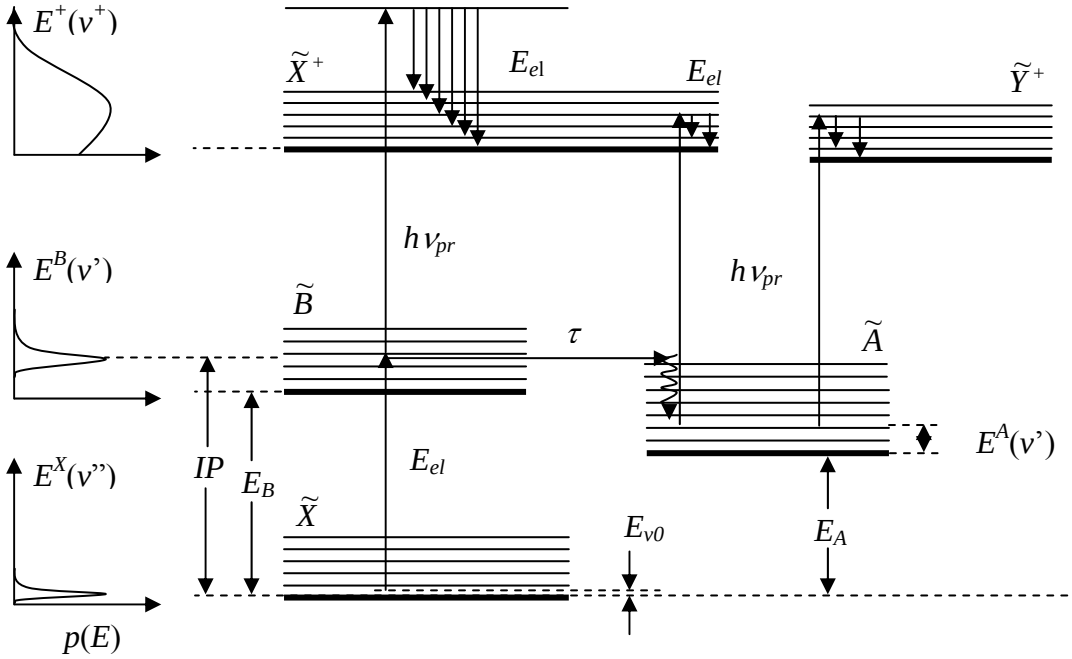

Figure 4: Energy level diagram illustrating the relation between photoelectron energy and the vibrational and electronic energy of the system. To the left of the figure are example energy distributions of the ground, intermediate and ionic states.

The probability of a transition occurring between the ground and excited states from excitation by the pump photon, $h\nu_{pr}$ is determined by the corresponding Franck-Condon factors. At time intervals after the pump pulse excitation, the molecule is ionised by absorbing a second probe photon, $h\nu_{pr}$. The energy of the system at this point is calculated by $E_{v0} + h\nu_{pu} + h\nu_{pr}$. If this energy is above the ionisation potential, IP, then ionisation can be caused. The distribution of states with internal energy $E^+(v^+)$ in the ionic state $\widetilde{X}^+$ is dependent on the Franck-Condon factors of the ionisation process. These are the Franck-Condon factors between the vibrational levels v^+ in the ionic state, $\widetilde{X}^+$ and the vibrational levels v' in the intermediate state, $\widetilde{B}$. The energy of the emitted electrons, E_{el}, represents the surplus energy not retained by the ion. The energy balance is expressed in equation 1.6, with it re-written in equation 1.7 to give the photoelectron energies, E_{el}:

$$E_{v0} + h\nu_{pu} + h\nu_{pr} = E_{el} + IP + E^+(v^+) \tag{1.6}$$

$$E_{el} = h\nu_{pu} + h\nu_{pr} - IP - (E^+(v^+) - E_{v0}) \tag{1.7}$$

The energy of the ion is therefore determined from the energies of the photoelectron, E_{el}. Equation 1.7 can be rewritten once again in terms of the electronic energy E_B and the vibrational energy, $E^B(v')$ of the excited state, so that $E_{vo} + h\nu_{pu} = E_B + E^B(v')$, to give:

$$E_B + E^B(v') - E^+(v^+) = E_{el} + IP - h\nu_{pr} \tag{1.8}$$

This shows that any change in photoelectron energy E_{el} is due to a change in the energy of the ion. This can be due to a change in vibrational energy of the intermediate state population, where the IP, $h\nu_{pr}$ and electronic energy will not change in the weak field limit. This can be accounted for by IVR or some molecular re-arrangement. In the case of an IC, ISC, dissociation or a reaction, the electronic energy will change since the molecule will reside on a new potential energy surface and be reflected in a change in the energy of the photoelectrons, E_{el}. Decoupling the vibrational from electronic dynamics can be difficult but often is resolved through understanding of the spectroscopy of the molecule. Photoelectron spectroscopy for these reasons is able to follow excited non adiabatic processes. The interpretation of the photoelectron spectra rely on some assumptions: (i) the energy of the molecule is conserved, since it is an isolated system in the gas phase. This implies that the reduction in ionisation is due to redistribution of the energy of the molecule into different degrees of freedom in such a way that does not favour ionisation anymore. (ii) The Franck-Condon factors connecting the vibrational levels populated through movement of the wave packet to the ion states will change and can be quantitatively related to the change in the photoelectron spectrum. The loss of signal in the ionisation process can also be caused by decoherence of the wave packet. To help fully resolve photoelectron spectra in these cases modelling of the potential energy surfaces is required using, for example, *ab initio* calculations.

1.2.4 TRPES applications

TRPES has been reviewed extensively by a number of groups (e.g. Radloff[12] and Stolow[4, 6, 13] as well as in references[8, 14-17]). In this section some of the seminal studies will be covered as well as some of those which highlight the depth of information that

can be obtained from TRPES. The examples will include studies that have shone light on non adiabatic processes such as, internal conversion and intersystem crossing, and work on doorway states in IVR, photodissociation and photoisomerisation. TRPES is an extremely powerful technique in resolving molecular dynamics and is utilised to monitor coherent control processes.

The first application of laser photoelectron spectroscopy was conducted on benzene by Reilly *et al*. using a broadband excimer laser[18]. This initial approach was improved on later[19] by this group by using a 1+1' photon scenario in the near ultraviolet region with narrow band lasers of ~1 cm^{-1} bandwidth to obtain high resolution spectra. The 1+1' scheme enabled relaxed selection rules that were previously hampering the one photon ionisation schemes. Knee *et al.* followed up on this work using picosecond resolution to study the nonradiative processes of S_1 benzene[20]. The first study of intramolecular dynamics was conducted by Hayden *et al.* that shall be discussed in further detail in section 1.2.4.2.

1.2.4.1 Observing vibrational motion

Seel and Domcke in 1991, theoretically demonstrated in their seminal work[10, 11] on the vibrational multimode dynamics of pyrazine that the nuclear dynamics are reflected in the temporal variations of their photoelectron spectra. This relationship between the time resolved photoelectron spectra and the time dependent probability in Na_2 was demonstrated by Engel and Meier[21] in 1993. They proposed a three photon scheme as depicted in figure 5 (a). A 620 nm pump laser creates wave packets in the $A^1\Sigma_u^+$ state with a one photon absorption and subsequently a wave packet in the $2^1\Pi_g$ state with a two photon transition, both at their inner turning points. The vibrational motion of the diatomic is tracked through the change in photoelectron energy, where the higher energy photons correspond to a longer bond length and shorter bond lengths to lower photoelectron energies. The time resolved photoelectron spectra as a function of energy, figure 5 (c), can thus be converted to a function of bond length as seen in figure 5 (d). By probing the wave packet at smaller time steps from t=0 than the period of vibration, and that the pulses were of a shorter duration than the vibrational period enabled it to be successfully resolved. In 1996, Baumert *et al*.[22]

verified this prediction experimentally and the time resolved photoelectron spectrum from this work is shown in figure 5 (d). With the experimental results so closely matching that of the theory left the community convinced of the power of photoelectron spectroscopy as an ideal tool for observation of vibrational wave packets and more generally molecular dynamics.

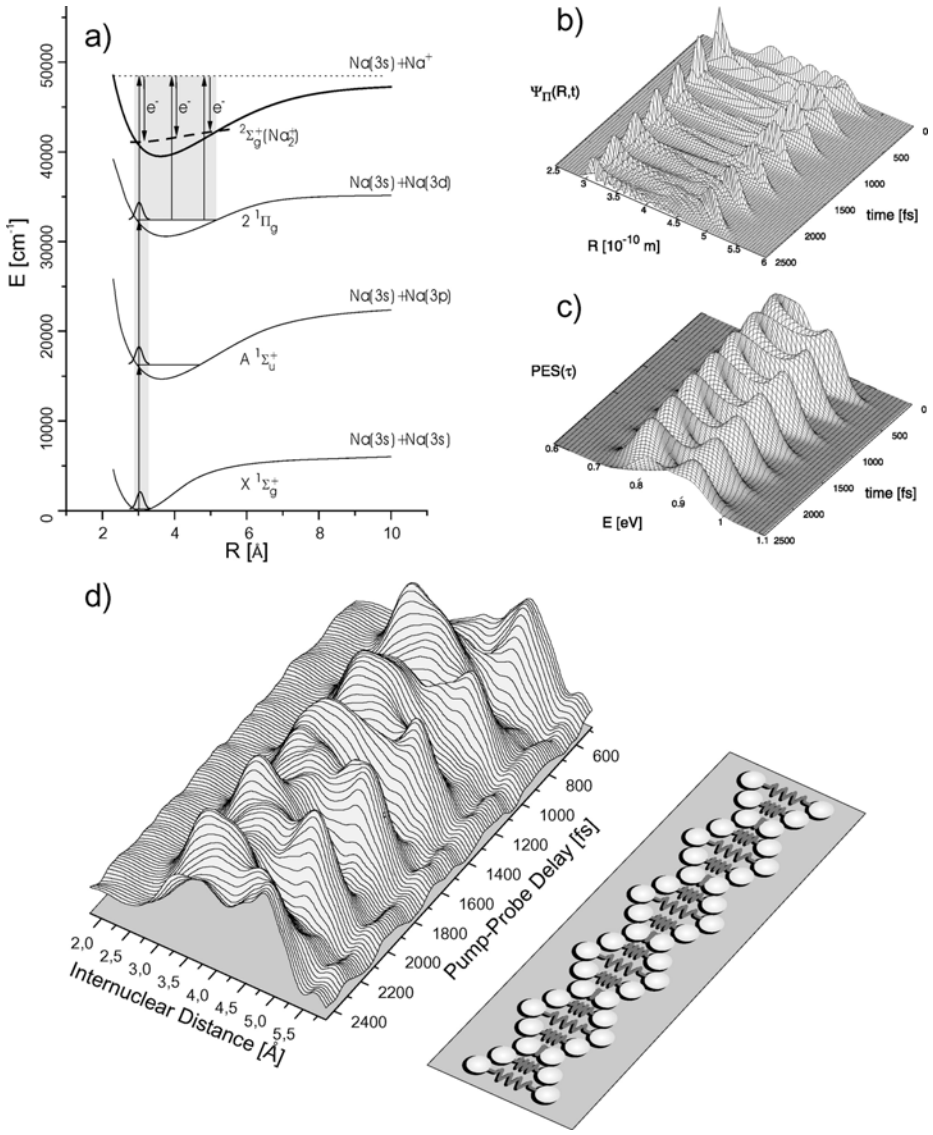

Figure 5: Vibrational dynamics of Na_2. (a) shows the excitation scheme for the Na_2 molecule. The pump laser at 620 nm creates wave packets in the $A^1\Sigma_u^+$ and the $2^1\Pi_g$ states at the inner turning points, these are monitored by a time-delayed probe. (b) is a plot of the absolute square of the vibrational wavepacket in the Π-state created by a two-photon transition from the ground state. (c) shows the photo electron spectrum from a one-photon ionization out of the Π-state. The periodic motion of the wavepacket can be seen here. (d) The same spectrum is plotted with energy against atomic distance and time delay.[11]

1.2.4.2 Internal conversion

In 1996, the first study of non adiabatic intramolecular dynamics in a polyatomic molecule was conducted by Cyr and Hayden[23]. They utilised a combination of time resolved ion yield and photoelectron spectroscopy to observe a fast, 20 fs, internal conversion in 1,3,5-hexatriene from the excited S_2 state to the S_1 state. The excited wave packet on the S_1 state was then seen to access the ground state in 300 fs.

In 1999, Stolow and co workers published findings using TRPES to resolve the non adiabatic intramolecular dynamics in a polyatomic molecule[24]. In their scheme, depicted in figure 6, a 287 nm pump pulse created an excited state wave packet on the $^1B_{1u}$ state of all-trans decatetraene which corresponds to the S_2 surface. From here the wave packet redistributed to S_1 through a conical intersection. The moving wave packet was ionised sequentially, in by now the well established pump probe method, with a 235 nm probe pulse and the photoelectrons were analysed. Linear polyenes possess the interesting property that they photoiosmerise between cis and trans isomers. This mechanism is responsible for photosynthesis and vision. The TRPES show that the wave packet undergoes a rapid change in potential energy, over 400 fs, which was rationalised as internal conversion through a conical intersection. The energies of the prevalent photoelectrons change due to the Franck Condon overlaps being different in the new states. The photoelectrons ε_1 correspond to a good overlap with the D_0 state and the photoelectrons ε_2 with D_1. The excited electronic states of the molecule and radical were calculated theoretically to confirm the proposed excitation scheme. This experiment was an example of a Koopmans type I scenario, whereby, the ionisation of the two excited states studied correlate with two different ionisation continua. This situation is ideal for disentangling the electronic from vibrational dynamics.

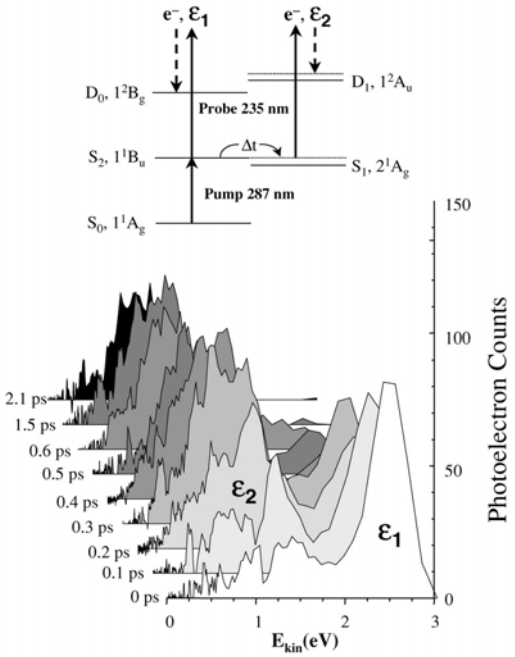

Figure 6: Molecular dynamics of all-trans decatetraene. (Top) Energy level scheme for TRPES of all-trans decatetraene. The pump pulse populates the S_2 state, the wave packet moves to the S_1 state via a surface crossing that gives the wavepacket 0.7 eV of vibrational energy. (Bottom) TRPES spectra of all-trans decatetraene for wavelengths of the pump and probe pulses of 287 nm and 235 nm respectively. The time from which the population transfers from the S_1 to the S_2 state is around 400 fs and is calculated as the time between the band ε_1 at 2.5 eV and growth of the broad band of ε_2.

Systems where the two excited states correlate with the same ionisation continua, Koopmans type II are more difficult to unravel. Phenthrene is a Koopmans type II molecule but owing to its rigidity its vibrational dynamics can still be clearly observed by TRPES[25]. Figure 7 illustrates the excitation scheme used to monitor an internal conversion between the S_2 and S_1 states in phenthrene. A 282 nm pump pulse created a wave packet on the excited state that was probed by a 250 nm probe pulse. The obtained time resolved photoelectron spectra are shown in figure 1.2.7, within them the bands ε_1 and ε_2 correlate to the S_2 1^1B_2 surface and S_1 2^1A_1 surface respectively. Both excited state surfaces have a Franck Condon overlap with the same ionisation continua D_0, 1^2B_1. The photoelectrons of ε_1 and ε_2 differ in energy because when the wave packet moves through the conical intersection it becomes vibrationally hot from the electronic energy being transformed into vibrational energy. The Franck Condon overlap is best with a $\Delta v = 0$ propensity, and so causing ionisation to a vibrationally hot cation state. This is seen in the transfer in energy from 1.5 eV in ε_1 to 0.7 eV in ε_2 which happens at a decay rate of 522±16 fs. The excited state population has moved entirely to S_1 after 1500 fs. The system has uncharacteristically well defined photoelectron peaks because of the rigidity of the structure which causes the geometries in the two excited states are very similar. The similarity means that most of the 0.74 eV of the molecule is transferred to vibrational energy since none is used

in a change in geometry and so allows for a significant shift in photoelectron energy. The internal conversion is aided by the fact that the S_1 state has a high density of vibronic levels which the wave packet on S_2 can couple with. The wave packet once on the S_1 state is unable to travel back to the S_2 state. This causes a substantially long dephasing time.

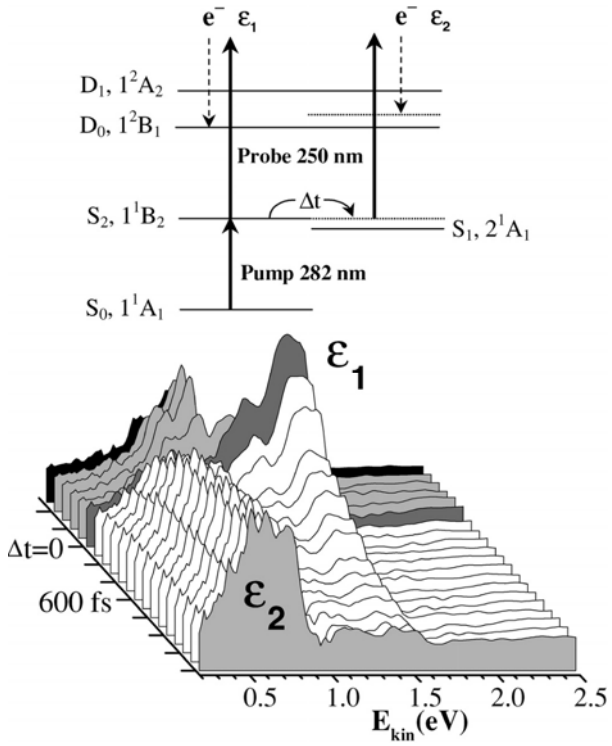

Figure 7: Intramolecular dynamics of phenanthrene. (Top) Energy level scheme for TRPES of phenanthrene. The pump pulse populates the S_2 state, the wavepacket moves to the S_1 state via a surface crossing that gives the wavepacket 0.74 eV of vibrational energy. (Bottom) TRPES spectra of phenanthrene for wavelengths of the pump and probe pulses of 282 nm and 250 nm respectively. The time from which the population transfers from the S_1 to the S_2 state is around 520 fs and is calculated as the time between the band ε_1 at ~1.5 eV and growth of the band at ε_2 at ~0.5 eV.

1.2.4.3 Intersystem crossing

In 1999, Suzuki and co workers presented the first time resolved photoelectron imaging studies[26] where a pair of ion optics create a field which maps the kinetic energy of the photoelectrons to radius on the detector surface. The move to this more efficient detection technique yields not only the kinetic energy of the photoelectrons but also their angular distributions. In this study they were able to experimentally obtain the photoelectron angular distribution of NO $A^1\Sigma^+$ from the photoelectron image. The dynamics of the S_1 state of pyrazine was also studied. The S_1 B_{3u} state was excited by a single photon pump pulse at 320-350 nm and then probed by a two photon pulse centered at 393 nm. Previous work had already been conducted on this system and the biexponential decay indicating dephasing with a decay rate ~100 ps time scale had been attributed to intersyem crossing to T_1. The photoelectron images obtained showed two distinct photoelectron rings of differing energy and anisotropies.

The photoelectrons in the energy range above 630 meV were seen to be lowering in energy and those below increasing in energy and were attributed to the singlet and triplet respectively. This was while the total photoionisation signal remained constant since the probe is able to ionise both the singlet and triplet. The T_1 state lies lower in energy than S_1 and so the wave packet has more vibrational energy after undergoing intersystem crossing. From this data they found the decay rate of the singlet to be 108 ps and the rate of intersystem crossing to be 98 ps from a cross correlation of 450 fs.

1.2.4.4 Intramolecular vibrational energy redistribution

In 2004, the group of Yamada *et al*. studied intramolecular vibrational energy redistribution of the OH/OD stretch vibration of phenol[27]. Both the phenol-d_0(C_6H_5OH) and phenol d_5(C_6D_50H) were compared. In this scheme an infrared (IR) pulse excites the OH/OD stretching vibration in phenol which is then probed by a 1+1 resonance enhanced multiphoton ionisation via the S_1 state using a UV pulse with a duration of 12 ps. Although ions were collected instead of photoelectrons this example serves to illustrate observation of doorway states which are of relevance in chapter 3. A picosecond infrared pump pulse was used to excite the OH stretch vibration in phenol-d_0 and phenol-d_5, which subsequently undertook IVR with lifetimes of 14 ps and 80 ps, respectively. The difference in decay rate is due to the heavy atom causing an increased "OH stretch-bath state" anharmonic coupling constant in phenol-d_0 than in d_5. The IVR process was seen to be mediated by a set of doorway states which selectively couple to the OH/OD vibration and in turn to a dense bath of states. The different energies of the doorway states in the phenol-d_0 and phenol-d_5 molecules were thought to be causing the difference in decay rates. Direct detection of the doorway states was hampered by the significantly increased decay rate between them and the OH/OD vibration than between it and the bath states. The TRPES shown in figure 8 (d) shows three distinct features, bands A and B, which, seem to be out of phase with that of the known OD_1^0 stretch. The bands A and B were concluded to be imaging the doorway state. The two-step tier model that represents the results is shown in the top of figure 8 (b) and its corresponding eigenstate picture at the bottom. The picosecond pulse coherently excites strongly coupled states in the OD stretch region to give the non-stationary states. The non stationary states oscillate

to the doorway states, and at each oscillation lose some intensity to the dense bath states. The eigenstate picture in figure 8 (b) shows the wave packet to be composed of three states, since band A was found to be composed of three oscillations. Their approximate energy level spacings are indicated on the figure. The bottom plot in figure 8 (a) shows band A after the bath state contribution has been removed. A similar quantum beat was also observed in the IVR of the OD stretch of phenol-d_6 and is shown in figure 8 (c). It has only one frequency of oscillation and the two energy levels are indicated inset in the figure. By sampling the available vibrations in the energy region of pump pulse in phenol-d_0, band A and B were assigned as $1_1^0 6a_1^0 12_1^1 18b_1^1$ and $1_1^0 6a_1^1 12_1^1 18b_1^1$ respectively.

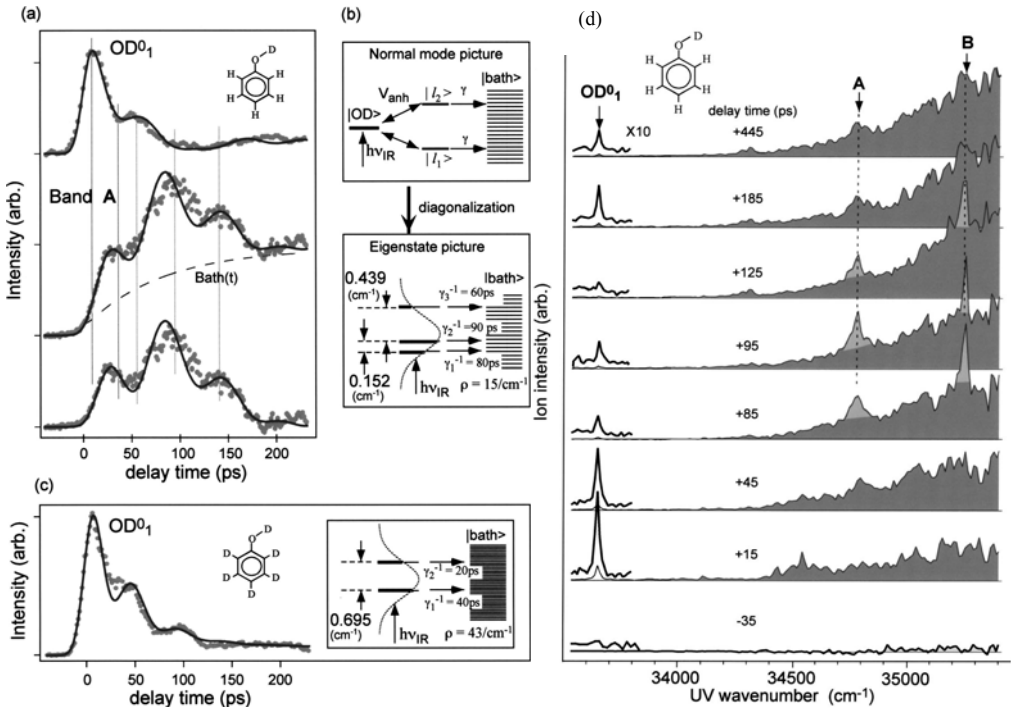

Figure 8: Molecular dynamics of phenol. (a) The time profiles of OD_1^0 and band A of phenol-d_1 . Lower trace is that of band A with the subtraction of the rise function due to dense bath states. The solid curves are the calculated time evolution of the OD level and the doorway state. (b) The coupling scheme for IVR of the OD_1^0 stretch of phenol-d_1. Upper trace: The |OD> state is coupled with the doorway states, $|l_1>$ and $|l_2>$, via V_{anh} and the later states are further coupled with the bath states, |bath>. Lower trace: The diagonalized picture forming three quasistationary states. (c) The time evolution of the OD band ~33 817 cm^{-1} of phenol-d_6, the solid curve is simulated based on the model shown in the right. (d) The transient UV spectra observed at several delay times after exciting the OD stretching vibration of phenol-d_1, bands A and B are out of phase with the OD_1^0 band[21].

A simpler type of IVR was studied by Reid et al. using the prototypical Fermi resonance in toluene[28]. In this study the $6a^1$ + $10b^1 16b^1$ Fermi resonance in S_1 was excited at 457 cm^{-1} with a 1 ps pulse. Using photoelectron imaging they were able

observe an oscillation in the ratio of intensities between the $\nu = 0$ peak associated with the $6a^1$ mode and the $\Delta\nu=0$ peak associated with the $10b^1 16b^1$ mode. They resolved a phase difference of $\pi/2$ between the two states. The oscillation in intensities was measured to be 6 ps which corresponded well with the energy separation of the states measured with dispersed fluorescence.

1.2.4.5 Photoisomerisation

The study of photoisomerisation has attracted attention by the community due to its involvement in photonics and data storage as a molecular switch and as a trigger in protein folding. Azobenzene is a prototypical molecular switch undergoing photoisomerisation between the cis and trans isomers through excitation in the 280-340 nm energy range. The group of Stolow *et al*. collected TRPES data of this process by ionising at 207 nm in a 1+1 photon REMPI scheme[29]. The group of Martinez et al. modelled the data and between them they were able to resolve previously collected seemingly contradictory aspects of the photochemistry. The proposed electronic pathways are shown in figure 9. It shows that two pathways exist to the ground state, one which leads exclusively to the trans isomer and another that travels through two consecutive conical intersections, the last one of which allows the excited state population to access the cis or trans ground state structures. The pathway from $S_{3,4}$ was found to have ring localised character and so suggests a pathway involving phenyl-ring dynamics which would indicate a torsion of the ring to give the trans isomer. The decay of the population from S_2 was found to undertake an inversion about the central bond, to yield a planar geometry on S_1. The planar geometry upon decay to the ground state can then either take the trajectory to the cis or trans isomers. These findings fitted with all the previous observations and highlights the power of TRPES to help identify the two near degenerate states $S_{3,4}$ and S_2 which had until then avoided detection.

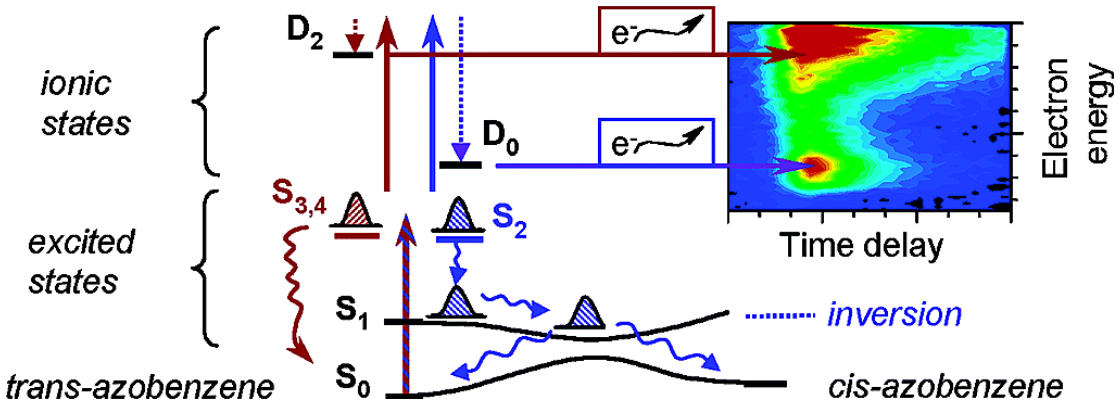

Figure 9: Molecular dynamics of in azobenzene**.** Proposed electronic relaxation pathways for S_2 and $S_{3,4}$: S_2 to S_1 internal conversion occurs with $\tau = 170$ fs at planar geometry. Subsequent relaxation S_1 to S_0 is expected to follow Kasha's rule with a yield of isomerisation of 25%. The $S_{3,4}$ state with a lifetime $\tau = 430$ fs has a different but not fully characterized relaxation pathway to the trans isomer in S_0, explaining the reduced the yield of isomerisation to 12% observed for the $\pi\pi^*$ states.[23]

1.2.4.6 Proton transfer

Proton transfer is an important primary process in many chemical reactions and has been studied using TRPES by Stolow and co-workers[30]. They studied the proton transfer in o-Hydroxybenzaldehyde (OHBA), going from the enol to the keto structure. OHBA represents the simplest aromatic molecule to study. It was found that after excitation by a 326 nm pulse the excited state population moved to the keto form in under 50 fs. From there it decays to the ground state through a conical intersection in 1.6-6 ps over the range 286-346 nm of excitation. The monodeuterated isotope of OHBA, ODHA was also studied and revealed no isotope effect in the rate of proton transfer, which suggests the barrier in the OH stretch coordinate is non existent or very small.

1.2.4.7 Photodissociation

Radloff and co-workers have also made a variety of contributions to the field over the years, a number of which have used photoelectron – photoion coincidence spectroscopy. This technique uses two detection systems for one interaction region, so that the photoelectron emitted is collected at the same time as the photoion. Coincidence detection yields a further wealth of information since the dynamical information is from the molecular frame rather than the laboratory frame. In 1999,

Radloff applied this technique to resolve the photodissociation dynamics of CF_2I_2 which has a broad featureless absorption profile which had hindered any insight into the mechanism[31]. He found that the molecule dissociates into $Cl_2 + I + I$ in 100 fs after undergoing an ultrafast non adiabatic process with a decay rate of 30 fs. The results indicated three electronic states were involved in the process. In 2001, he also studied the photodissociation of ClO_2 at 398 nm and was able to resolve the complex dissociation dynamics since each ion and consequently each associated photoelectron could be analysed. The A^2A_2-A^2A_1 transition was found to have a decay constant of 7 ps. The A^2A_1 decayed to the $^2B_2$ state through internal conversion and dissociation at a time constant of ~ 250 fs. The $^2B_2$ state then decayed through and internal conversion at a time constant of ~750 fs.

Hayden *et al.*[47] in 2000 were able to utilise the difference in photoangular distributions (PADS) to resolve the mechanism of photodissociation of NO_2. They were able to measure the PADS in the molecular frame in a form of coincidence imaging. The NO fragment was ionised and it was found that the PADS evolve from a forward-backward asymmetric with respect to the dissociation axis at short delays (<500 fs) to totally symmetric at long delays (>1ps).

The cases so far have been concerned with neutrals but work has been completed on anions, super excited states and clusters. New techniques have developed like coincidence imaging and molecular alignment which are furthering the field of molecular dynamics as a whole

The work presented in this thesis investigates the non radiative non adiabatic relaxation process in the first excited state of benzene. TRPES is used to observe an ultrafast intersystem crossing. It is found that ISC is facilitated by a doorway state, T_2, which couples to S_1 along the prefulvene coordinate. T_2 subsequently couples to, T_1 a dense bath state where the energy is quickly dissipated.

1.3 Coherent control in the weak field limit

1.3.1 Introduction

The ability to observe excited state processes was naturally followed by the desire to dictate the outcome of such processes. Coherent control is the field of study concerned with manipulating the quantum coherence effects of light to predispose a particular outcome of a photochemical event. The early part of the last century saw the culmination of scientific breakthroughs leading to the idea that energy and matter have wave like properties. The idea that the phases of excited non stationary states dictate the path taken by an excited state wave packet and the realisation that such phases could be controlled by shaping the phase of the exciting light field brought about the field of coherent control. Initial experiments aimed at using coherent light sources set at specific frequencies to break specifc bonds in polyatomic molecules. However these early endeavours were hampered by intramolecular vibrational redistribution of the energy deposited into the vibrational modes of the molecule, leading to unspecific bond breakage. It was realised that interference effects could in fact be used to manipulate chemical dynamics. Brumer and Shapiro demonstrated one of the first control schemes that selected a specific branching channel through the interference of excited state wave packets[32]. By manipulating the phase difference between two narrow bandwidth lasers, two separate excitation pathways interfere with each other to alter populations in different final states. In 1995 Gordon *et al*. achieved a clear demonstration of coherent control using DI molecules[33]. A molecular beam of DI was hit with three photons of 353.69 nm and one photon from the 3rd harmonic of this beam corresponding to 117.90 nm. These created two degenerate transitions, which interfered with each other to reach one of two final states, the final states depending on the phase difference between the excitation paths.

The development of femtosecond light sources gave experimentalists the ability to deposit energy on the timescale comparable to vibrational motion. Tannor, Kosloff and Rice were the first to select a photoproduct through the implementation of the "pump dump" scheme[34]. In this control scheme a vibrational wave packet was created by the broad bandwidth of a femtosecond laser pulse on the excited state. The wave packet was allowed to evolve over the potential energy surface until it reached a

structure that correlated to the ground state of the desired product upon which point a second femtosecond laser pulse was fired into it to deposit it onto the ground state. The dumping to the ground state can cause a range of desired effects, in this case dissociation. This approach was core to the field, since it demonstrated that control schemes could be thought of intuitively in the time domain in terms of manipulating the evolution of wave packets on an excited state potential energy surface. The two approaches brought about the desire to manipulate phase effects as in the Brumer and Shapiro scheme but using an ultrashort pulse such as used in the Tanner, Kosloff and Rice scheme.

1.3.2 Pulse shaping

To have access to control over both the frequency domain interference effects but also to have these on a time scale comparable to molecular vibrations implied the need to shape the "pump" femtosecond light pulses. It was in 1988 that Shi, Woody and Rabitz suggested the excitation pulse shape could be tailored for each photochemical reaction in what was termed optimal control theory[35]. This is the idea of controlling the trajectory of the excited state wave packet by altering the phase and amplitude of the excitation light pulse so specific vibrational modes are excited. Shaping of pulses in electronics was already a developed field and was used to accelerate the progress in shaping of optical electrical fields. In this area they manipulated the frequency profile of electrical pulses in order to control the time domain shape[36]. This is the core idea in pulse shaping in the frequency domain when using spatial light modulators and acousto optic methods. Since femtosecond pulses are too short to gain access to the pulse mechanically (in the time domain) interference effects had to be used instead in the frequency domain to obtain shaped pulses in the time domain.

The crossover between the fields of pulse shaping and TRPES was fuelled by the realisation that this would cause a ubiquitous tool for coherent control to be available that would allow experimentalists to create excited state wave packets with a superposition of eigenstates that they chose. Prior to this laser pulses generally had a uniform shape like a Gaussian, as these were delivered from femtosecond light sources. Manipulation of the pulse shape could be achieved in a confined manner with techniques such as a Michelson interferometer. Shaping of the frequency and

amplitude of femtosecond pulses enabled the field of coherent control to flourish and the most popular of techniques to this end was the use of a spatial light modulator within a 4f zero dispersion set-up.

In 1992 Judson and Rabitz[37] first applied optimal control theory to realise coherent control through the introduction of a learning algorithm as a means to find the optimal phase and amplitude of ultra-fast pulses with which to control a chemical reaction. It was suggested that by creating a feedback loop between a measurement device of the experiment and the shape of the spectral mask, a 'fitness' function could be calculated. This was used as the signal for a learning algorithm that creates arbitrary spectral profiles to be fed into a pulse shaping device. In this way the Schrödinger equation is solved exactly for the system in real time.

1.3.3 Coherent control of chemical reactions

Baumert *et al*[38], first demonstrated coherent control over a chemical reaction using a learning algorithm. The branching ratio of a photodissociation reaction of an organometallic complex $CpFe(CO)_2Cl$ was controlled using a feed-back optimised pulse shaping set-up. Mass spectrometric analysis generated the ratio between the two mass differentiated products, which was used as the fitness function within an evolutionary algorithm. The ratio of $CpFeCOCl^+$ / $FeCl^+$ was minimised as well as maximised, while the other products were ignored. This system proved suitable since the parent molecule and the products all differed in mass aiding in their identification.

A recent example of coherent control in a biological system shows the extensiveness and advancement of the field. The energy flow between two pathways within the light harvesting complex LH_2 present in Rhodopseudomonas acidophila, a photosynthetic purple bacterium, were manipulated by coherent control in order to affect the branching ratio[39]. The phases of the light field mediated the ratio of energy flow between intra- and intermolecular channels in the complexes donor-acceptor system.

Daniel *et al*. were able to use a collaborative study of the theoretical and experimental disciplines in order to follow the reaction dynamics of an organometallic molecule as a function of the optimal control laser field[40]. This study represents the direction in

which the field is likely to advance with the use of computational calculations to elucidate the vibrational dynamics of the wave packet and in so doing affording a complete explanation of why the shaped laser field is optimal for the experiment. In this work an evolutionary algorithm was used to find an optimal pulse shape consisting of two dominant sub pulses followed by a third smaller one, all separated by 85 fs. The first pulse excites the molecule in a 2 photon process, after molecular re-arrangement the second pulse ionises the molecule in a 3 photon process. The molecular yield of $CpMn(CO)_{3+}$ was maximised from CpMn(CO), whilst minimising $CpMn(CO)_{+}$.

1.4 Conclusion

In the first half of this chapter, an overview of molecular dynamics has been presented specifically regarding work done using the time resolved photoelectron spectroscopy detection technique. This technique has enabled a range of nonadiabatic processes to be observed in real time. The work presented in chapter 3 uses this method to observe an ultrafast nonadiabatic process in the channel 3 region of benzene. A range of polyatomic molecules such as benzene undergo rapid non radiative energy dissipation (channel 3) which in the case of benzene has not been fully understood.

The understanding of molecular dynamics is naturally followed by the desire to control those dynamics. The field of coherent control was discussed in the second half of this chapter with an overview of pulse shaping techniques utilising spatial light modulators. In chapter 4, the development of a UV pulse shaping capability is described and the shaped UV pulses obtained are characterised using an XFROG set-up. Chapter 5 discusses some of the potential applications of the pulse shaping apparatus to control the dynamics observed in benzene.

1.5 References

1 J. S. Zugazagoitia, C. X. Almora-Diaz and J. Peon, *Journal of Physical Chemistry A*, 2008, **112**, 358-365.

2 A. H. Zewail, *Angewandte Chemie-International Edition*, 2000, **39**, 2587-2631.

3 A. H. Zewail, *Journal of Physical Chemistry A*, 2000, **104**, 5660-5694.

4 A. Stolow, *International Reviews in Physical Chemistry*, 2003, **22**, 377-405.

5 A. Stolow, *Annual Review of Physical Chemistry*, 2003, **54**, 89-119.
6 A. Stolow, A. E. Bragg and D. M. Neumark, *Chemical Reviews*, 2004, **104**, 1719-1757.
7 D. M. Neumark, *Annual Review of Physical Chemistry*, 2001, **52**, 255-277.
8 T. Seideman, *Annual Review of Physical Chemistry*, 2002, **53**, 41-65.
9 I. Fischer, M. J. J. Vrakking, D. M. Villeneuve and A. Stolow, *Chemical Physics*, 1996, **207**, 331-354.
10 M. Seel and W. Domcke, *Journal of Chemical Physics*, 1991, **95**, 7806-7822.
11 M. Seel and W. Domcke, *Chemical Physics*, 1991, **151**, 59-72.
12 I. V. Hertel and W. Radloff, *Reports on Progress in Physics*, 2006, **69**, 1897-2003.
13 A. Stolow, J. G. Underwood, T. Schultz and J. P. Shaffer, *Abstracts of Papers of the American Chemical Society*, 2002, **223**, C46-C46.
14 K. L. Reid, *Annual Review of Physical Chemistry*, 2003, **54**, 397-424.
15 N. E. Henriksen and V. Engel, *International Reviews in Physical Chemistry*, 2001, **20**, 93-126.
16 T. Suzuki, *Annual Review of Physical Chemistry*, 2006, **57**, 555-592.
17 M. Wollenhaupt, V. Engel and T. Baumert, *Annual Review of Physical Chemistry*, 2005, **56**, 25-56.
18 J. T. Meek, R. K. Jones and J. P. Reilly, *Journal of Chemical Physics*, 1980, **73**, 3503-3505.
19 S. R. Long, J. T. Meek and J. P. Reilly, *Journal of Chemical Physics*, 1983, **79**, 3206-3219.
20 C. E. Otis, J. L. Knee and P. M. Johnson, *Journal of Physical Chemistry*, 1983, **87**, 2232-2239.
21 C. Meier and V. Engel, *Chemical Physics Letters*, 1993, **212**, 691-696.
22 A. Assion, M. Geisler, J. Helbing, V. Seyfried and T. Baumert, *Physical Review A*, 1996, **54**, R4605-R4608.
23 D. R. Cyr and C. C. Hayden, *Journal of Chemical Physics*, 1996, **104**, 771-774.
24 M. Schmitt, S. Lochbrunner, J. P. Shaffer, J. J. Larsen, M. Z. Zgierski and A. Stolow, *Journal of Chemical Physics*, 2001, **114**, 1206-1213.
25 V. Blanchet, M. Z. Zgierski and A. Stolow, *Journal of Chemical Physics*, 2001, **114**, 1194-1205.
26 T. Suzuki, L. Wang and H. Kohguchi, *Journal of Chemical Physics*, 1999, **111**, 4859-4861.
27 Y. Yamada, N. Mikami and T. Ebata, *Journal of Chemical Physics*, 2004, **121**, 11530-11534.
28 C. J. Hammond, K. L. Reid and K. L. Ronayne, *Journal of Chemical Physics*, 2006, **124**.
29 T. Schultz, J. Quenneville, B. Levine, A. Toniolo, T. J. Martinez, S. Lochbrunner, M. Schmitt, J. P. Shaffer, M. Z. Zgierski and A. Stolow, *Journal of the American Chemical Society*, 2003, **125**, 8098-8099.
30 S. Lochbrunner, T. Schultz, M. Schmitt, J. P. Shaffer, M. Z. Zgierski and A. Stolow, *Journal of Chemical Physics*, 2001, **114**, 2519-2522.
31 P. Farmanara, V. Stert, H. H. Ritze and W. Radloff, *Journal of Chemical Physics*, 2000, **113**, 1705-1713.
32 P. Brumer and M. Shapiro, *Chemical Physics Letters*, 1986, **126**, 541-546.
33 L. C. Zhu, V. Kleiman, X. N. Li, S. P. Lu, K. Trentelman and R. J. Gordon, *Science*, 1995, **270**, 77-80.

34 D. J. Tannor, R. Kosloff and S. A. Rice, *Journal of Chemical Physics*, 1986, **85**, 5805-5820.
35 S. H. Shi, A. Woody and H. Rabitz, *Journal of Chemical Physics*, 1988, **88**, 6870-6883.
36 A. M. Weiner, *Review of Scientific Instruments*, 2000, **71**, 1929-1960.
37 R. S. Judson and H. Rabitz, *Physical Review Letters*, 1992, **68**, 1500-1503.
38 A. Assion, T. Baumert, M. Bergt, T. Brixner, B. Kiefer, V. Seyfried, M. Strehle and G. Gerber, *Science*, 1998, **282**, 919-922.
39 J. L. Herek, W. Wohlleben, R. J. Cogdell, D. Zeidler and M. Motzkus, *Nature*, 2002, **417**, 533-535.
40 C. Daniel, J. Full, L. Gonzalez, C. Lupulescu, J. Manz, A. Merli, S. Vajda and L. Woste, *Science*, 2003, **299**, 536-539.
41 W. Heitler, F. London, *Z. Phys*., 1927, **44**, 455.
42 H. Eyring, *J. Chem. Phys*. 1935, 3, 107.
43 M. G. Evans, M. Polanyi, *Trans. Faraday Soc*. 1935, **31**, 875.
44 M. Eigen, *Discuss. Faraday Soc*, 1954 **17**, 194.
45 R. G. W. Norrish, G. Porter, *Nature*, 1949, **164**, 658.
46 T. Suzuki, L. Wang and H. Kohguchi, *Journal of Chemical Physics*, 1999, **111**, 4859-4861.
47 J. A. Davies, R. E. Continetti, D. W. Chandler and C. C. Hayden, *Physical Review Letters*, 2000, **84**, 5983-5986.

Chapter 2

An experiment for time-resolved photoelectron imaging

The experimental apparatus employed to monitor ultrafast non radiative decay processes of excited molecules in the gas phase using time resolved photoelectron spectroscopy is described. A new femtosecond laser system and photoelectron imaging apparatus were designed, built and optimised in order to utilise the pump-probe technique to monitor molecular dynamics. These and the principles and techniques are presented. Also the principles and techniques used to fully characterise ultrashort pulses in both time and frequency are described.

2.1 Laser system and vacuum set-up

2.1.1 The laser system

A commercial laser system was used to provide femtosecond laser pulses of variable wavelength laser light. The laser table layout of the laser system is shown in figure 1. The femtosecond laser pulses were created by a Ti:Sapphire oscillator. They were then amplified in pulse power by a regenerative amplifier. The amplifier seeds two optical parametric amplifiers (OPA) affording wavelength tuneability and the pulse diagnostics. In the following sections the physical principles of the femtosecond oscillator, regenerative amplifier and optical parametric amplifiers will be described.

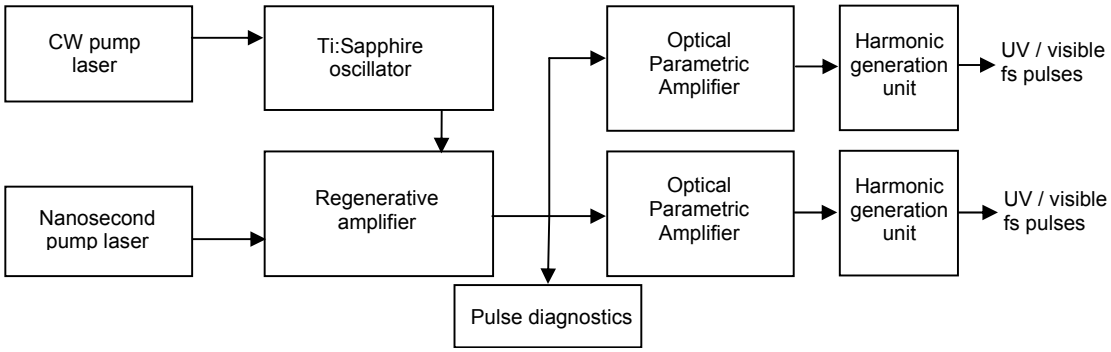

Figure 1: Schematic of the laser system used to generate tuneable wavelength femtosecond pulses. A Ti: Sapphire oscillator is pumped by a continuous wave laser to generate a 30 fs pulse centred at 785 nm. The femtosecond pulses seed a regenerative amplifier which is pumped by a nanosecond Nd:YLF laser. The pulses are amplified to 2.5 μJ and have a repetition rate of 1 kHz. The beam is split into three parts, 1 μJ for each OPA and 0.5 μJ for use in pulse diagnostic apparatus. Each OPA uses two optical parametric generation processes to tune and amplify a signal beam. The signal beam from the OPA is directed to a harmonic unit where sum frequency generation affords pulses in the visible region. The visible pulse is used in a subsequent second harmonic generation process to afford pulses in the ultra violet region.

The Ti:Sapphire oscillator (Coherent Mira) is fundamentally a laser cavity. The cavity has a gain medium at its centre, here Ti:Sapphire (titanium-doped sapphire, Ti^{3+}:Al_2O_3), amidst two laser cavity mirrors, one of which has a reflectivity <100% that is the output coupler. The cavity is pumped by a 5 W continuous wave (CW) laser (Coherent Verdi) at 527 nm. The pump laser increases the population inversion maintaining maximum stimulated emission of photons from the gain medium. The length of the cavity, L, determines the frequencies, ν, that can be supported which are integer or half integer

number, n, of wavelengths. They are related by $\nu = nc/2L$, where c, is the speed of light. The frequencies supported by the cavity are also determined by the gain bandwidth of the gain medium, for our laser cavity the optimum wavelength is centred at 785 nm and has a bandwidth of 32 nm with a pulse duration of 28 fs.

Femtosecond pulse durations are achieved through modelocking of the pulse by manipulation of the optical Kerr effect and the introduction of noise into the laser cavity. Modelocking is the effect by which a continuous wave with random phases is reorganised so all the phases of the frequency components are aligned in time and a pulse is created. These pulses have a very similar time, frequency and spatial profile to a Gaussian and so in the rest of this work shall assume to be Gaussian unless otherwise stated. The width of the pulse in time and frequency is given in terms of its full width at half maximum (FWHM). From the uncertainty principle the time duration Δt and spectral width $\Delta \nu$ of these pulses, are related to each other by the time bandwidth product[5].

$$\Delta \nu \Delta t \geq 0.441 \tag{2.1}$$

The optical Kerr effect is the change in the refractive index of a medium induced by an intense incident electric field. The refractive index of the medium is $n = n_0 + n_2 I$, where n_0 is the linear refractive index, n_2 is the nonlinear refractive index, and I is the laser intensity ($n_2 = 3.1 \times 10^{-16}$ cm^2 W^{-1} in Ti:Sapphire). The phase delay experienced by the propagating optical pulse is proportional to the refractive index[5],

$$\phi(\omega) = n(\omega)\omega L/c, \tag{2.2}$$

where ω is the angular frequency, $n(\omega)$ is the frequency-dependent refractive index, L is the length of the material and c is the speed of light in a vacuum. The time-dependence of the intensity of the laser pulse, $I(t)$, induces a time-dependence to the refractive index, $n(t) = n_0 + n_2 I(t)$, which produces a time-dependent phase delay[5],

$$\Delta\phi(t) = n_2 I(t)\omega L/c \tag{2.3}$$

For a pulse propagating in an optical medium of length L, the accumulated phase results in an instantaneous frequency shift[5],

$$\Delta\omega(t) = -n_2 \frac{dI(t)}{dt}\omega L/c\,, \tag{2.4}$$

which gives rise to new frequency components, broadening the spectrum and therefore reducing the pulse duration, Δt. This phenomenon is called self-phase modulation (SPM). The Kerr effect also causes a change in the spatial profile of the beam and is used to instigate modelocking. The laser pulse has a Gaussian spatial profile of intensity, which induces a positive lens effect in the gain medium from the change in refractive index with laser intensity. The positive lens causes self focusing, increasing the Kerr effect yet further. Within the cavity a slit is used to allow only the middle core of the Gaussian intensity profile to propagate and to remove the CW component. This selects a set number of longitudinal modes with which to make up the pulse spectral bandwidth which is increased through the gain medium. A device is used to introduce a change in path length to the cavity, which amounts to noise. This is achieved through the introduction of a pair of mirrors which increase the path length by around 10 mm without altering its direction periodically and rapidly. The noise causes an overlap of the phases of enough frequencies with which to cause the formation of a pulse through constructive interference. The femtosecond pulses are generated at a repetition rate of 80-100 MHz with a pulse energy of a 0.7 nJ and a beam diameter of 2.5 mm.

2.1.2 Chirped pulse regenerative amplification

The femtosecond pulses formed in the oscillator are amplified by chirped pulse regenerative amplification to afford enough energy for the nonlinear processes used in the OPAs and for use in pulse diagnostics. The amplification process uses a laser cavity with a Ti:Sapphire gain medium very much like the femtosecond oscillator. The population

inversion is seeded by the femtosecond pulses from the oscillator and pumped by a nanosecond laser. The nanosecond laser (Coherent Evolution-30) is a solid state Nd:$LiYF_4$ (Nd:YLF) laser that is pumped by 12 AlGaAs laser diode arrays to afford a pulse centred at 1053 nm. An intra cavity high threshold (lithium triborate – LBO) frequency doubling crystal facilitates pulses centred at 527 nm. The cavity is acousto-optically Q-switched to afford an output pulse with 1 kHz repetition rate, a pulse duration of 300 ns and a pulse energy of 20 mJ.

The power of the pulse produced in the laser cavity of the amplifier without stretching would be sufficiently large to induce unwanted nonlinear processes within the gain medium and damage to the optical components. To avoid these effects the input seed pulse is stretched in time within a stretcher set-up consisting of a gold coated grating and collimation optics. The pulse is chirped to ~10 ps linearly reducing the peak power of each pulse. The introduction of the seed pulse into the cavity is carefully timed by a Pockels cell (an electro-optic switch) which opens for the duration of the pulse. The amplification gain is determined by the number of round trips the pulse takes in the laser cavity. Once the pulse has made enough round trips, commonly 14, to reach a significant power i.e. 2.5 W, a second Pockels cell releases the amplified pulse out of the cavity. Both Pockels cells are controlled externally by timing electronics. The selected output pulse is compressed into the shortest possible pulse length in a compressor set-up, a mirror version of the stretcher. The pulse energy at this point is 2.5 mJ at 800 nm, with a pulse duration of approximately 40 fs and beam diameter of 5 mm. The 2.5 mJ output of the amplifier is split using a beamsplitter into 0.6 mJ used in pulse diagnostics and 1.9 mJ used by the two OPAs.

2.1.3 Nonlinear optics

The effects that light itself induces as it propagates through a medium are described as nonlinear optical phenomena and are utilised in the laser system, frequency upconversion and pulse diagnostics. They are harnessed to convert between different frequencies of light as well as such effects as the Kerr effect and within the electro-optic switches. Crystals with no inversion symmetry and that are transparent to the incident radiation

undergo nonlinear effects. When the induced dipole moment of a material responds instantaneously to an applied electric field **E**, the dielectric polarisation **P** in a medium can be written as a power series in the electrical field[5]:

$$\mathbf{P} = \varepsilon_0 \left[\chi^{(1)}\mathbf{E} + \chi^{(2)}\mathbf{E}^2 + \chi^{(3)}\mathbf{E}^3 + \cdots \right] \tag{2.5}$$

where ε_0 is the permittivity of free space and the coefficients $\chi^{(n)}$ are the *n*th order susceptibilities of the medium. For low light intensities, **P** is linear in the electric field **E**, whereas the higher order nonlinear contributions become important with increasing intensity. In the case of the $\chi^{(2)}$ the electrical field can be expressed as[5]:

$$E(t) = E_1 e^{i\omega_1 t} + E_2 e^{i\omega_2 t} + c.c. \tag{2.6}$$

where E_1 and E_2 are the two incident beams and c.c. denotes the complex conjugate. A medium that is pumped by the fields E_1 and E_2 will radiate a field E_3 with an angular frequency $\omega_3 = \omega_1 + \omega_2$.

The efficiency of the frequency conversion process is determined by the phase matching between the polarisations of the fields and the crystal axis complying with the condition $\mathbf{k}_p = \mathbf{k}_s + \mathbf{k}_i$, where **k** denotes the vector of the field. The nonlinear crystals are birefringent and commonly possess three axes, one that has a different refractive index, the extraordinary (e) axis, from the other two the ordinary axes (o). If the signal and idler have the same polarisation, it is called "Type-I phase-matching", and if their polarisations are perpendicular, it is called "Type-II phase-matching".

2.1.7 Optical parametric amplifier

Each OPA operates with around 0.9 μJ of the fundamental 800 nm beam. An OPA uses a series of nonlinear processes to generate a range of wavelengths whilst maintaining the ultrashort bandwidth of the input fundamental pulse. The processes involved do however create a chirp mainly from propagation through crystals, reflections of mirrors and from propagation through air. Optical parametric amplification, as shown in figure 2, is

obtained through focusing the fundamental pulse and a signal beam into a β–barium borate (BBO) crystal to generate a high electric field intensity to invoke a $\chi^{(2)}$ nonlinearity.

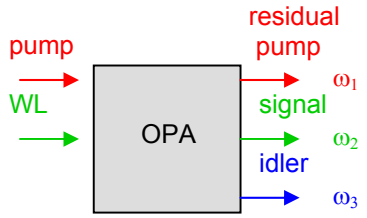

Figure 2: Optical parametric amplification, a three wave mixing process. Optical parametric amplification splits the pump frequency (ω_3) into two frequencies (ω_1 and ω_2) so that $\omega_3 = \omega_1 + \omega_2$ is obeyed. The high intensity of the pump field invokes a dominance of the $\chi^{(2)}$ nonlinearity. The white light generation pulse seeds the process and determines the frequency of the signal beam.

The OPA uses two optical parametric amplification processes, the first to create a tuneable wavelength signal and the second to amplify the tuneable wavelength signal. A small portion of the fundamental is tightly focused into a sapphire crystal to generate white light. This is collinearly focused with 10 % of the fundamental into a BBO crystal. The white light (WL) pulse is used as a variable wavelength seed to the optical parametric amplification process as the signal beam. By varying the temporal overlap between the incident pump pulse and WL pulse and crystal tuning angle, the phase matching conditions for different wavelengths of the WL pulse are satisfied affording wavelength tuneability. Optical parametric amplification is a three wave mixing process where the white light beam is used to seed the operation only. In the second optical parametric amplification process the signal beam from the first optical parametric amplification process is reflected back towards the nonlinear crystal as a seed pulse and is focused collinearly with a further portion of the fundamental pulse to amplify the seed beam to ~30 μJ depending on wavelength.

	Wavelength	Pulse Energy	Polarisation
Fundamental	795 nm	2.5 J	P
Idler	1600-2630 nm	60 mJ at 2.1 mm	S
Signal	1150-1600 nm	120 mJ at 1.3 mm	P
SFG idler	533-613 nm	22 mJ	P
SFG signal	472-533 nm	33 mJ	P
SHG-SFG idler	267-307 nm	5 mJ	S
SHG-SFG signal	235-267 nm	5 mJ	S

Table 1: Laser beam characteristics. Laser beam characteristics including wavelength, pulse energy and polarisation are shown for femtosecond beams in the OPAs. It can be seen that wavelengths can be accessed from the IR through the visible down to the deep UV.

Each OPA has a separate harmonic unit attached which employs further nonlinear processes to obtain shorter wavelengths using either the signal or idler pulses generated in the OPA as seeds. The obtainable wavelengths, pulse energies and polarisations are shown in table 1. A flip mirror is used to select either the signal or idler beam, the selected beam is directed collinearly with the residual pump light used in the amplification process into a second BBO crystal where sum frequency generation (SFG) is achieved. The SFG beam, which is now in the visible region, is frequency doubled in a second BBO crystal to achieve the wavelengths in the UV. A series of dichroic mirrors separate the UV, visible, residual pump and residual signal beams.

2.1.8 Vacuum system

The vacuum system comprises of two chambers, a source chamber where benzene is introduced into the vacuum apparatus, and a detection chamber housing the photoelectron imaging apparatus. Figure 3 shows a schematic of the set-up.

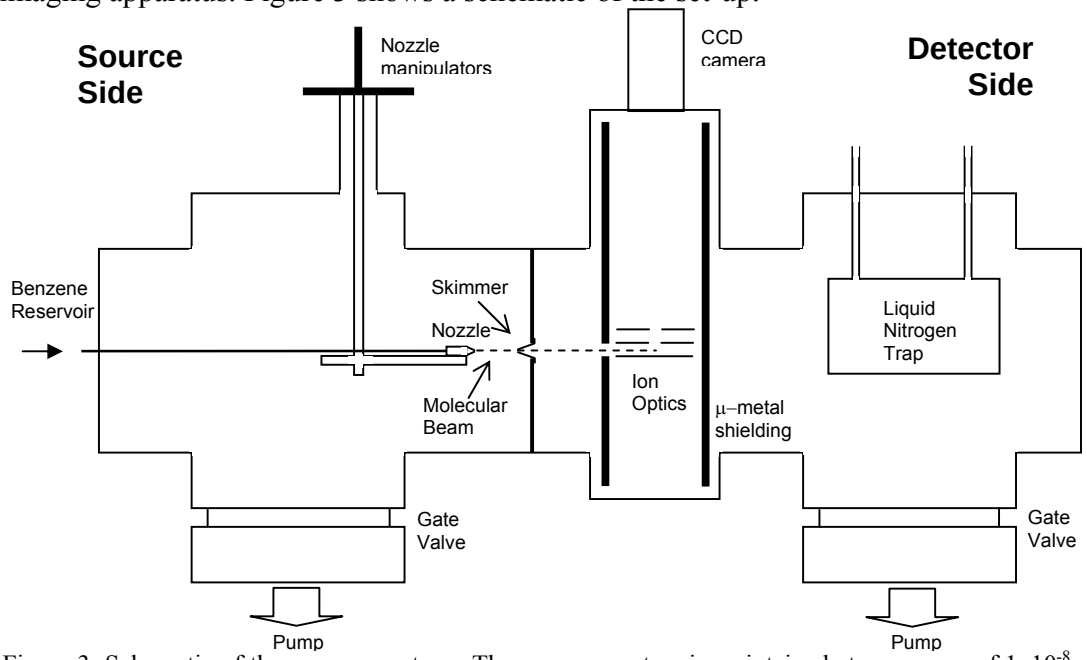

Figure 3: Schematic of the vacuum system. The vacuum system is maintained at a pressure of $1x10^{-8}$ atm on the source side and $1x10^{-8}$ atm on the detector side by a 2200 ls^{-1} diffusion pump backed by a 25 m^3/h rotary and a 1000 ls^{-1} diffusion pump backed by a 25 m^3/h rotary respectively. A benzene reservoir (figure 2.1.4) supplies gaseous benzene at a pressure of ~1 atm. The gas is emitted through a 50 μm nozzle, the inner core of which is selected by a skimmer that is 20 mm away. The skimmed molecular beam travels into the interaction region of the PEI set-up. The PEI set-up is protected by a μ-metal shielding preventing interference form stray fields. A nitrogen trap suspended in the detector side reduces signal noise in the PEI set-up, which can be attributed to freezing of excess gas. Nozzle manipulators in all cartesian axes and rotation allow alignment of the molecular beam into the interaction region.

The source chamber is pumped by a turbo-molecular pump (Leybold Mag W2200) with pumping speed of 2200 L s^{-1} backed by a 25 m^3/h rotary pump. It reaches pressures down to 1×10^{-8} atm with no gas introduction, and below 1×10^{-5} atm with a gas flow. The detector side is pumped by a turbo pump (Leybold Turbovac 1000 C) with a pumping speed of 1000 Ls^{-1} backed by a 40 m^3/h rotary pump. It reaches pressures down to 1×10^{-8} atm with no gas introduction, and below 1×10^{-7} atm with a gas flow. Benzene in the gas phase from the delivery system (see below) is introduced into the chamber through a 50 μm laser cut hole in the tip of the nozzle. The nozzle is aligned using external manipulators that have degrees of freedom in Cartesian co-ordinates as well as rotation. The nozzle was placed around 20 mm from the skimmer and aligned so the photoelectron image was round and maximum photoelectron counts obtained.

The skimmer (Beam Dynamics Model-2) is shaped as an inwards-curved cone, 23.1 mm in height and 22.9 mm in diameter at the base and is made from nickel with a 1.0 ± 0.05 mm hole in its end. It is set between the two chambers to select the middle core of the expanding benzene vapour beam where the molecules are at their coldest. The molecular beam then passes into the interaction region through a hole cut into the μ-metal shielding that houses the photoelectron imaging apparatus and reduces the effect of stray fields on the photoelectrons. It is crossed perpendicularly by the laser beam. A series of baffles placed inside the input and output laser windows were used to minimise scattered laser light generating photoelectrons within the vacuum chamber. The baffles were constructed from 5 black-anodised aluminium 4 mm diameter apertures that are separated by 10 mm and fixed in a co-axial arrangement. The liquid nitrogen trap was used to reduce long term signal fluctuations and noise by freezing excess benzene in the chamber, which would otherwise flow back in to the interaction region. It is formed by a cylinder suspended in the vacuum chamber by the tubes used to fill it.

Benzene (Aldrich ACS Reagent, 99%, used without further purification) was stored in a vessel outside the vacuum chamber and delivered to the nozzle inside the vacuum chamber *via* a series of tubes and valves as depicted in figure 4. The vessel had a stainless steel top allowing for a vacuum tight seal and a glass bottom so the contents could be monitored.

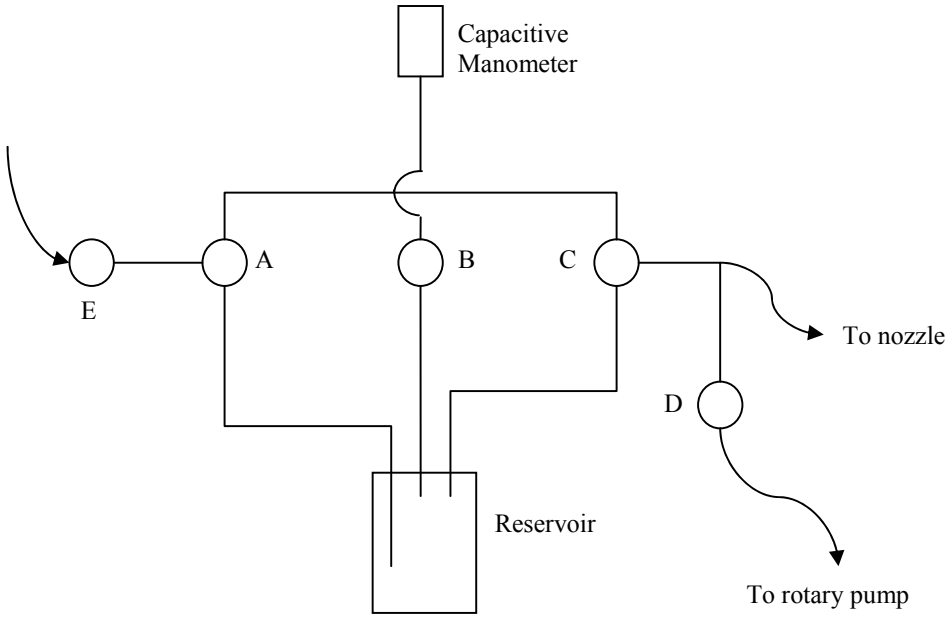

Figure 4: Schematic of the benzene delivery system. The benzene reservoir, constructed from a glass bottom and metal flange top, is filled with 30 mL of benzene. The vapour pressure provides adequate throughput of benzene gas. Valve E is used to flush the apparatus with a bath gas when changing between different molecular species. Valve A allows for either flushing of the gas line in the event of a blockage whilst isolating the benzene reservoir. Valve B provides access to measurement of the pressure of the apparatus. Valve C controls access to the chamber and valve D provides direct access to a rotary pump used in the flushing process.

During an experiment valves C and B were open and valves D and A closed. The vapour pressure of benzene at room temperature was on average 120 mbar and sufficient to create a continuous beam expansion in the interaction region. Valves A, C and D were used for venting the delivery system of gas. Valve B, A and C were closed to isolate the apparatus when refilling with benzene. In the early stages of the experiment Valve E was used to attach a carrier gas but was found to be unnecessary. The benzene container was filled to about 1/5 of its volume to prevent any liquid entering the gas line. When venting the system of gas using the rotary pump the benzene container was vacated of any remaining gas.

2.2 Photoelectron imaging

In the photochemistry experiments presented in this thesis, pump-probe photoelectron spectroscopy was used to observe excited state dynamics in benzene. A femtosecond

pump pulse creates a wavepacket on the first excited state which is subsequently ionised at regular time steps after its inception with another femtosecond pulse. The photoelectrons emitted in this 1+1 photon process were collected and analysed using photoelectron imaging apparatus. A generalised 1+1 photon pump probe energy level scheme is illustrated in figure 5.

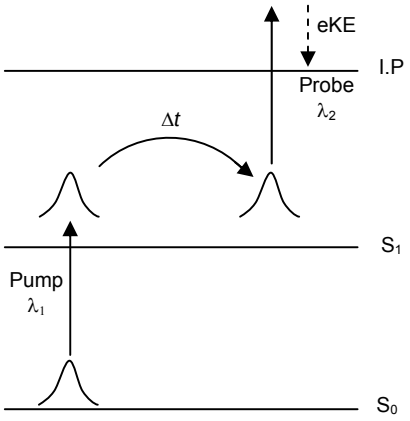

Figure 5: Energy level scheme for photoelectron spectroscopy. The molecule undergoes photon ionisation to yield a photoelectron whose kinetic energy, eKE, and angular momentum can be measured. An excited state wavepacket is created from ionisation of the ground state population with one photon, λ_1. The non-stationary state evolves and is ionised at regular time intervals, Δt, by a second probe photon, λ_2.

2.2.1 Imaging apparatus

The imaging apparatus is set up in a vacuum as described in section 2.1.8 and is based on the Eppink and Parker[1] design. The interaction region is defined by where the collinear pump and probe laser beam (*y* axis) bisects the skimmed molecular beam (*x* axis). The interaction volume is defined as the area of the focused beam at this point. The resulting ionisation is in all three dimensions (*x*, *y* and *z*) but the ion optics direct the photoelectrons in to the *z* axis using ion optics. The ion optics comprises a set of three polished stainless steel discs, nominally 2 mm thick and 105 mm in diameter. The discs are stacked vertically in the vacuum chamber and are separated by 15 mm by polyetheretherketone (PEEK) spacers.

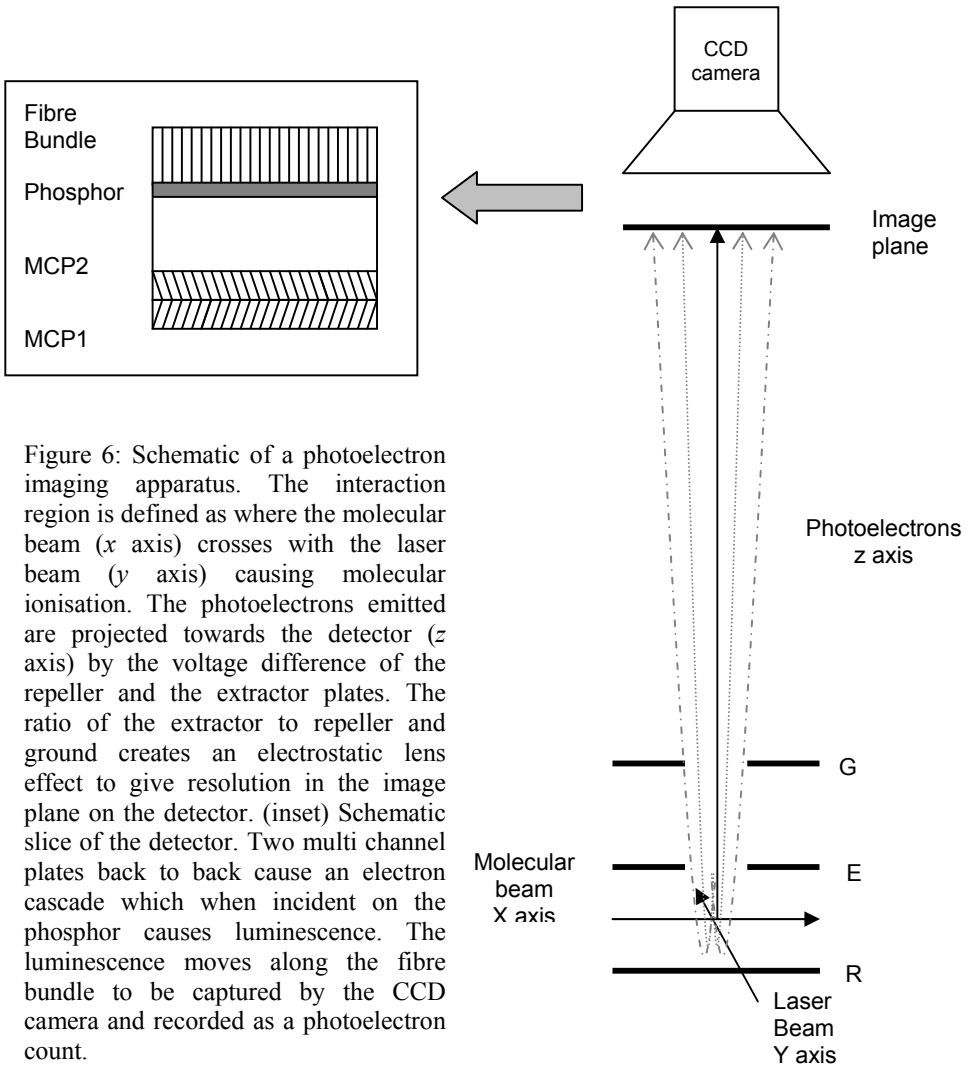

Figure 6: Schematic of a photoelectron imaging apparatus. The interaction region is defined as where the molecular beam (*x* axis) crosses with the laser beam (*y* axis) causing molecular ionisation. The photoelectrons emitted are projected towards the detector (*z* axis) by the voltage difference of the repeller and the extractor plates. The ratio of the extractor to repeller and ground creates an electrostatic lens effect to give resolution in the image plane on the detector. (inset) Schematic slice of the detector. Two multi channel plates back to back cause an electron cascade which when incident on the phosphor causes luminescence. The luminescence moves along the fibre bundle to be captured by the CCD camera and recorded as a photoelectron count.

The plate furthest from the detector and below the interaction region holds a negative voltage and acts as the 'repeller' to the emitted electrons, figure 2.2.2. Another plate on the other side of the interaction region, with a 15 mm hole in the middle acts as an 'extractor' to the ionised electrons. The voltage applied to the repeller is greater than that of the extractor, to repel the electrons out of the interaction region and through the weaker repulsion imposed by the extractor. With sufficient velocity to pass through the extractor plate the electron feels a further repulsion from the extractor which propels it towards the final plate and the detector. 0 V is maintained on the 'ground' plate and is the final part in the configuration of an electrostatic lens. Eppink and Parker[2] found that an electrostatic lens of this sort effectively maps out the charged particles travelling in 3D

from the interaction region to a 2D image in the detector plane, as if they all came from exactly the same place. The electrostatic lens allows photoelectron imaging to potentially detect all electrons ejected from around the full sphere surrounding the interaction region with a high resolution.

The effect of the charges on the first plate is to repel all emitted electrons upwards through the lens. Electrons with the highest kinetic energy maintain some of their velocity in the direction they were first emitted (shown as the dot dashed line in figure 6). These are mapped out onto the outer rings of the detector, while electrons with lower kinetic energy (shown as dotted line in figure 6) are seen closer to the centre of the detector. The ratio of the voltages applied to the repeller and extractor plates depends on the distance between the two plates. Eppink and Parker[2] found this value to be 0.71. The ratio that gave the sharpest images for the apparatus in our experiment was 0.692. Biasing voltages for the repeller and extractor are applied by high voltage DC supplies (Stanford Research Systems PS325/2500V-25W). The ion optics are supported on four insulated stainless steel legs attached to the vacuum flange at the lower end of the 200 mm diameter vertical tube. Magnetic shielding is provided by a 1 mm thick μ-metal tube 385 mm long and with a 110 mm inside diameter. The shielding surrounds the ion optics and the electron flight path from approximately 35 mm below the repeller up to a few millimetres below the photoelectron detector.

The imaging detector set-up is a commercial unit supplied by Photek. The 40 mm diameter double-layer chevron micro-channel plate (MCP) detector is mounted on the vacuum side of a 250 mm vacuum flange at the top of the electron flight tube. The MCP is connected to a block of phosphor which is observed by a charge coupled device (CCD) camera (Basler A312f) mounted around 5 cm away, through a bundle of optical fibres. When a photoelectron hits the MCP an electron cascade is induced which is due to a voltage being held across the plates. The electron cascade crashes into the phosphor block causing luminescence. The bundle of optical fibres which the phosphor block is mounted on transports the luminescence towards the camera vertically without spreading outward horizontally. The CCD camera records the light emitted from the phosphor block on

pixels which are recorded and averaged by the imaging software. The cascade of electrons causes oversized phosphorescence, which is not representative of the one electron that first hit the MCP. This is corrected in the following way: an average of such a group of pixels is taken and recorded as just one count on the central pixel which allows for the ratio of one photoelectron incident on the MCP to be recorded as one electron count by the CCD camera. Photoelectron emission can thus be observed in real time, which is useful in alignment of the interaction region. The counts build up to show intensity, with each frame recorded separately. The CCD camera is triggered at a 1 kHz rate and with a viewing time of 100 ns. The CCD chip has 782 × 580 pixels and the camera was positioned so that the MCP diameter filled its width to give image size of 768 × 576 pixels. Since electrons were collected, the MCP was operated with a continuous bias, with its front face (looking down the electron flight tube) held at 0 V and its rear face held at 2 kV. The phosphor screen was also biased at 4.5 kV. The camera was gated to reduce noise for a period of 100 ns for each laser pulse. This was controlled by external timing electronics.

2.2.2 Image inversion

In the imaging apparatus as described in figure 6, an ionisation event is caused by the molecular beam being crossed by a suitable energy pump-probe laser pulse scheme. The ions created can be emitted in all 3 dimensions creating a sphere of ions known as a Newton sphere. The Newton sphere of electrons is projected upwards towards the detector by the electric field induced by the ion optics around the interaction region. The ion optics map the 3D photoelectron distribution onto a 2D position sensitive detector as shown in figure 7. The photoelectron energy is proportional to the radius from the centre of the detector in the image plane. From this relationship the electron kinetic energy is obtained.

When using an excitation pulse polarised in the image plane, orbital angular momentum information of the emitted photoelectron can be obtained from the anisotropic distribution of the image An example of anisotropic distribution is shown in figure 9 for the ionisation

of xenon's $^2P_{1/2}$ and $^2P_{3/2}$ orbitals. In the case for benzene, no orbital angular information was available since it is a highly symmetric molecule and is not aligned yielding no anisotropy. In order to gain the photoelectron spectrum of the ionisation event the 3D Newton sphere must be reconstructed from the 2D image that is projected onto the detector.

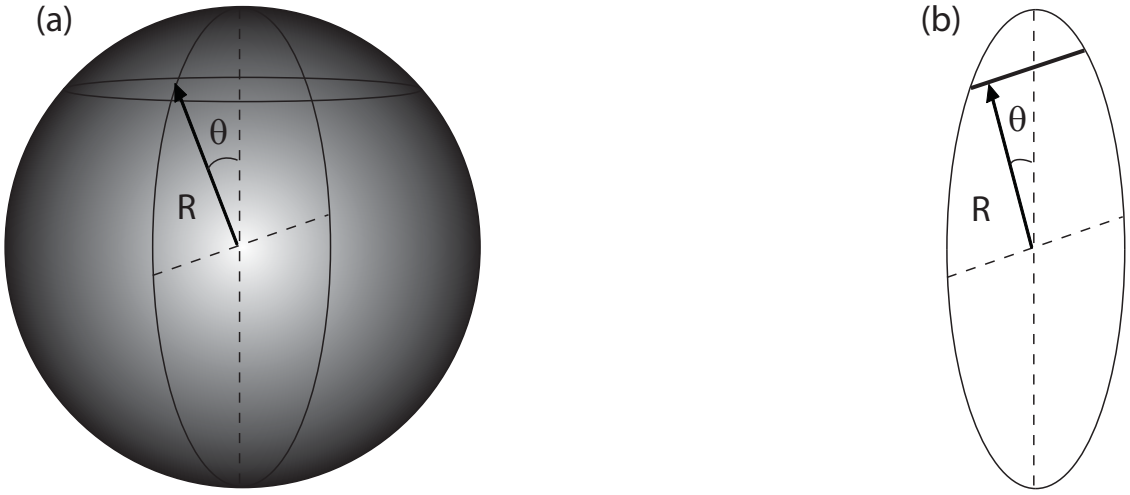

Figure 7: Mapping 3D distributions onto a 2D image. (a) Newton sphere in 3 dimensions representing the photoelectrons given of by the ionisation event. Using polar co-ordinates the 3D sphere is mapped onto a 2D image (b) by the ion optics. (b) A 2D image of the 3D Newton sphere expressed in polar co-ordinates. The 2D image is inverse Abel transformed to afford the photoelectron kinetic energy data which is proportional to the radius, with photoelectrons in the outer radii owning a high kinetic energy.

One of the fastest and most accurate approaches to the numerical solution is the use of the polar basis set expansion Abel transform (pBasex) method[2]. The introduction of using a basis set expansion to model the distribution to allow for easy transformation was first developed by Reisler *et al.* using a Cartesian coordinate system in the Basex method[3]. The inversion problem can be divided into 2 sections. These are the inverse Able transform that must be solved and the form chosen to represent the image to be transformed.

The pBasex method tries to solve the inverse Abel transform integral using a set of forward basis functions with analytical inverse Abel transforms fitted to the image. The image is effectively modelled with these basis functions that are computationally easy to inverse Abel transform. It has been found that the use of polar coordinates has advantages over conventional Cartesian coordinates in this endeavour. Firstly it is a more intuitive

way to describe the cylindrically symmetrical ionisation event that is caused from the field applied to the image being much higher than the kinetic energy of the particle (figure 6). Secondly, polar coordinates allow for noise that is distributed in a Cartesian grid to be smoothed out prior to inversion. The inverse Abel transform expressed in polar coordinates for a system that is cylindrically symmetric is:

$$P(R',\theta') = 2\int_{|x|}^{\infty} \frac{rF(R,\theta)}{\sqrt{r^2 - x^2}}\, dr \tag{2.7}$$

$$x = R'\sin\theta'$$

$$r = R\sin\theta$$

The original distribution $P(R', \theta')$ and projected distribution of the 3D Newton sphere, $F(R, \theta)$ are shown in figure 2.2.3, where R is the radius and θ, the angle from the axis of symmetry. To solve this integral directly for a raw image is numerically challenging due to the formation of singularities, for example when $r = x$, instead a basis set is used to fit to the data which does not suffer from this problem. An expansion in Legendre polynomials in spherical coordinates is used as the basis set to describe the angular distributions of the photoelectrons with respect to the polarisation vector of the light. The energy distribution of the particles is then modelled using a discrete number of Gaussian functions with a width, σ, which is set as the width of a pixel to give the expression:

$$F(R,\theta) = \sum_{k=0}^{k=k_{\max}} \sum_{l=0}^{k=k_{\max}} c_{kl} f_{kl}(R,\theta) \tag{2.8}$$

with

$$f_{kl}(R,\theta) = e^{-(R-R_k)^{2/\sigma}} P_l(\cos\theta), \tag{2.9}$$

Here, θ is measured with respect to the polarisation direction (linearly polarised) of the light, P_l is the Legendre polynomial of order l and R_n represents the centre of the nth Gaussian. R represents the ejection energy and is taken as related to the radius within the

image as explained earlier. The basis function used to model the detector, as shown below, is obtained by combining equations (2.8) and (2.9):

$$g_{kl}(R',\theta') = 2\int_{|x|}^{\infty} \frac{rf_{kl}(R,\theta)}{\sqrt{r^2 - x^2}}\, dr \tag{2.10}$$

This integral of the inverse Able transform of the basis functions corresponding to the image can be expressed now as a linear expansion:

$$P(R',\theta') = \sum_k \sum_l c_{kl} g_{kl}(R',\theta') \tag{2.11}$$

From this equation the coefficients c_{kl} can be taken and substituted into equation (2.8) to reconstruct the original distribution. Equation (2.11) describes a case in which the distribution in the detector is continuous when for an image it is a discrete matrix of Cartesian pixels. For that reason the width of the Gaussian is set to be the width of a pixel and the linear expansion can be converted into terms relating to the pixels:

$$P_{ij} = \sum_k \sum_l c_{kl} g_{ij;kl} \tag{2.12}$$

where i,j are the detector radial and angular pixels respectively, and P_{ij} is obtained by converting the initial Cartesian coordinates of the detector to polar coordinates. Using Legendre polynomials has the benefit of allowing terms in the expansion to be eliminated depending on the distribution expected from the photoionisation event. When the light is linearly polarised as it is in the work described in this thesis the odd Legendre terms are eliminated. The more general rule for number of terms in the polynomial, l_{max}, is $l_{\max} = 2n$, where n is the number of photons.

One of the benefits of the pBasex method is that the noise accumulates towards the centre of the detector where the resolution is lowest anyway rather than spread over all the data. The energy resolution, $\Delta E/E$, of the photoelectron imaging apparatus is determined by the

energy range which the ion optics magnify over as well as the number of pixels in the range. More specifically this can be calculated as the FWHM of a peak divided by the electron kinetic energy of the peak. In the case of the 2+1 photoionisation scheme of xenon as described in the next section (2.2.3) the energy resolution comes to 0.0542. The energy resolution in our experiments however is limited to ~50 meV by the laser bandwidth.

2.2.3 Calibration of the photoelectron imaging apparatus

To calibrate the detector a photoionisation of a known transition was related to the value and ratio of the voltages on the plates of the electrostatic lens[10]. A pulse centred at 249 nm (4.98 eV) was used in a 2+1 resonant photoionisation scheme in Xenon. A two photon absorbtion of the 249 nm pulse is resonant with the $6p[1/2]_0$ state at 9.96 eV. From this level a third photon is absorbed to give a total energy of 14.94 eV which causes ionisation over the ionisation potential at 12.12 eV. The kinetic energy of the photoelectrons, eKE, are calculated from the total of the absorbed photon energies in case, 3(hν), and the ionisation potential, IP, by the relationship 3(hν) – IP = eKE. The atom relaxes to either of the two doublet $^2P_{1/2}$ or $^2P_{3/2}$ states of the Xenon ion. The kinetic energies of the photoelectrons emitted were used to calibrate the detector. The energy level scheme for this is shown in figure 2.2.4. The image shows the outer and inner ring electrons inhabiting the top and bottom of the image but not the edges indicating anisotropy. As explained earlier the anisotropy is caused by the linear polarisation of the ionising laser field.

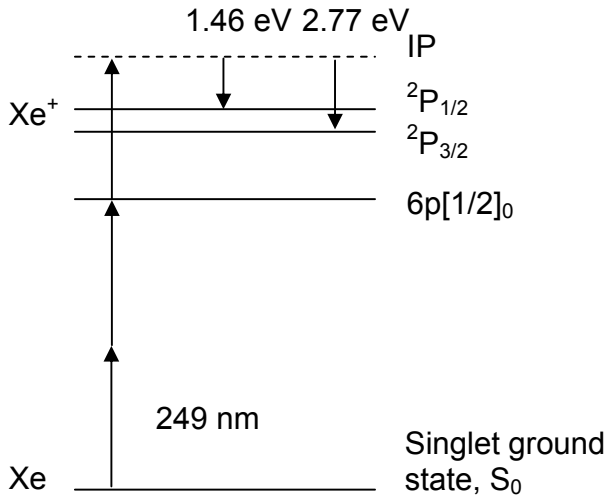

Figure 8: Energy level scheme for the photoionisation of xenon from a 2+1 photon absorption. The $6p[1/2]_0$ state is resonant with two photons of 249 nm. The excited state then absorbs another photon to access the ionisation continuum. The emitted photoelectrons have well known kinetic energies of 1.46 eV for the $^2P_{1/2}$ and 2.77 eV for the $^2P_{3/2}$ and are used to calibrate the detector

The ion optic voltages were set so both of the outer electrons would be captured within the detector radius. The voltages of 2500 V on the repeller and 1745 V on the extractor were used to give the maximum resolution from the outer most ring being as close to the detector edge as possible. Figure 9 (a) shows the raw image obtained.

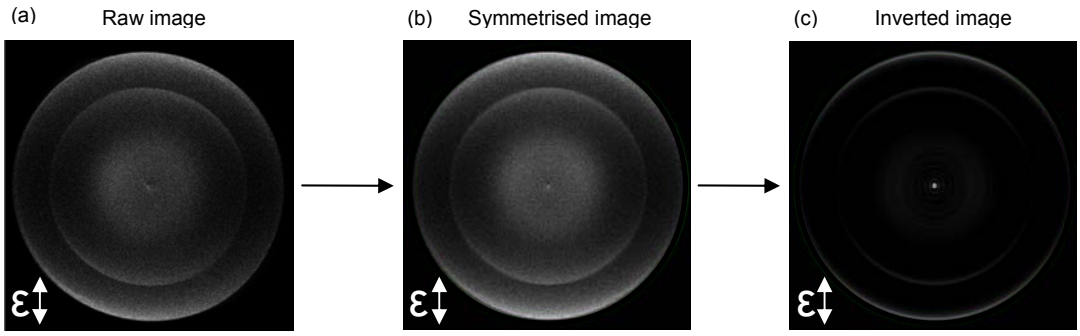

Figure 9: Image inversion. (a) Raw photoelectron image. The two rings from the $^2P_{1/2}$ and $^2P_{3/2}$ can be seen on the inner and outer area of the image, respectively. (b) Symmetrised image. The image is cut in the vertical and horizontal planes and reflected onto itself to give and average of the four quarters. This helps to reduce noise and strengthens predominant features. (c) Inverted image. The matrix arrived at from symmetrisation is inverse Abel transformed using the pBasex method.

The CCD camera is controlled by imaging software which records the photoelectron counts that are incident on the detector every second and stores them as a matrix of integers called a frame. The software sums every image continuously. An image collected for an hour is made up of $60 \times 60 = 3600$ frames. The matrix was reshaped from a rectangle to a square and delivered into the pBasex software. The inversion software

centres a circle around the target area to be inverted using the centre of mass of the image. This spherical section was symmetrised across the horizontal and vertical directions so that all the information is contained in a single quarter of the image, figure 9 (b). This technique helps remove spurious counts and further embolden faint spectra. The image was then inverted by the pBasex method to give an image as shown in figure 9 (c). The pBasex software delivers a photoelectron spectrum of pixel number against normalised intensity as shown below:

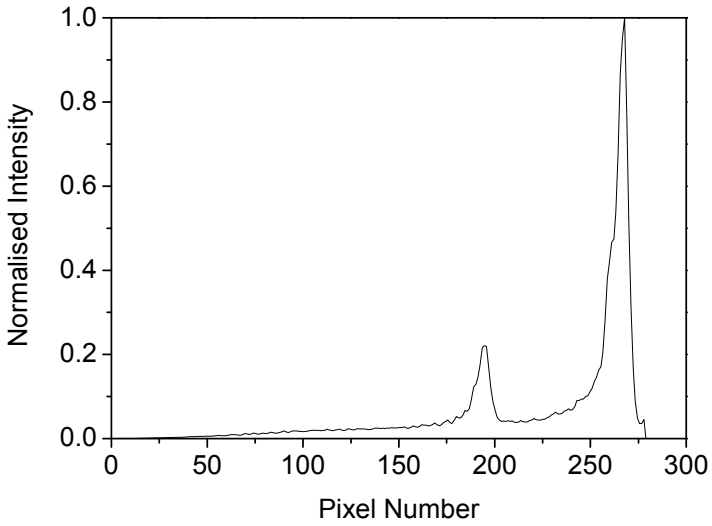

Figure 10: Photoelectron spectrum of normalised intensity as a function of pixel number. The inverse Abel transform integral is solved using the pBasex method. The smaller peak corresponds to the $^2P_{1/2}$ and the larger peak corresponds to the $^2P_{3/2}$.

The pixel number, P was converted to photoelectron energy, eKE by

$$eKE = P^2\left(\frac{E_{peak}}{P_{peak}^2}\right) \tag{2.13}$$

where E_{peak} is the energy in eV of the peak and P_{peak} is the position in pixel number of the peak. Using the energies of $^2P_{1/2,3/2}$ transitions giving rise to the peaks observed in the spectrum of 1.46 eV and 2.77 eV from a 2+1 ionisation by 249 nm photons (4.98 eV) the pixel numbers were converted to electron volts (eV) to give a complete photoelectron spectrum:

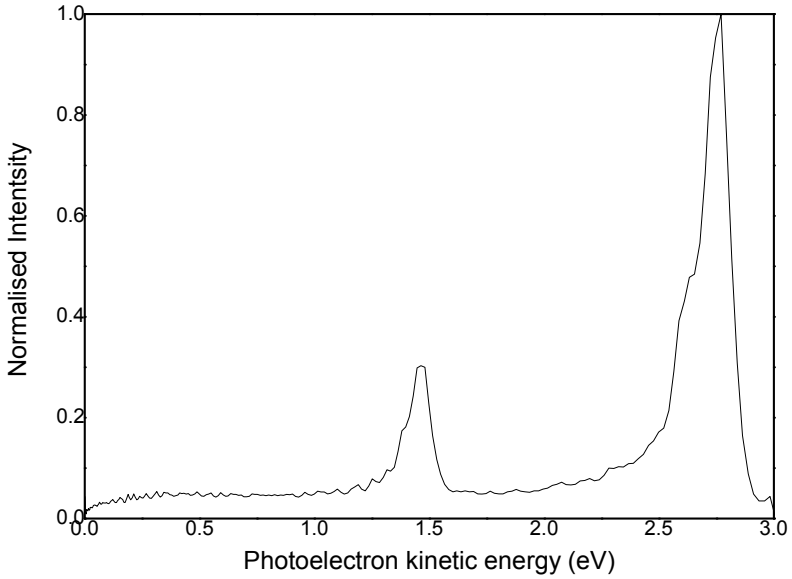

Figure 11: Photoelectron spectrum of normalised intensity as a function of energy (eV). The energies of the $^2P_{1/2}$ and $^2P_{3/2}$ at 1.46 eV (small peak) and 2.77eV (large peak) as well as the radial nature of the image are used to convert pixel number to energy (eV) of the spectrum.

The voltages were then reduced to include the inner ring of xenon as close to the detector edge as possible to enable as high resolution for the lower energy photoelectrons emitted from benzene whilst maintaining the ability of accurate calibration. A repeller voltage of 968 V and extractor voltage of 1400 V gave the best distribution of photoelectrons within the image for benzene and used throughout all experiments described.

The proposed excitation scheme that is detailed in chapter 3 uses two UV pulses enabling a 1+1 excitation scheme. Signals other than this occur and must to the best of efforts be removed from the 1+1 signal. The power of the beam was attenuated to achieve 1+1 ionisation but must be kept at a reasonable level to give a sufficient signal. Measurements of power dependence will be discussed in chapter 3. Remotely controlled shutters were used to block the pump and probe beams. Images from pump only, probe only and a pump and probe were collected. This was achieved by blocking the probe beam and collecting an image then blocking the pump beam and collecting an image then allowing both open to collect a pump and probe signal. The pump only and probe only images were then subtracted from the final pump and probe beam image to obtain a pump probe image. This means a pump probe image was obtained with minimal contributions from pump only and probe only ionisations. An example of the image subtraction is shown in

figure 12. Two shutters (electro-optical products model SH-10-B) were used which operate at 24 V and were interfaced into the Photek IFS32 imaging software, these have been shown in figure 2.1.14. A macro written within the Photek IFS32 imaging software controlled the shutters opening and closing and the collection and storage of the imaging data. Typically for time resolved photoelectron imaging data collection, each image collected photoelectron counts for a period of 20 seconds. The image subtraction was undertaken and the resultant pump probe image stored. The collection loop was continuously run for an hour and the final image composed by addition of all the pump probe images collected for that period.

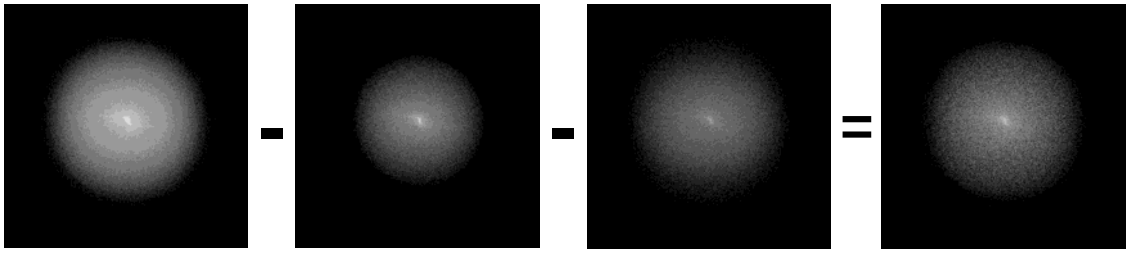

Figure 12: Image subtraction. The pump only image and probe only image were subtracted from the pump probe and pump and probe images to arrive at the image from the pump and probe pulse contributions only. Each of the first three images are recorded for a period of 20 s. Imaging software subtracts the images to give the 1+1 pump and probe image.

The delay between the pump and the probe was controlled by a motorised stage (Physik Instrumente M-510.12) placed in the pump beam path (figure 13). To increase the pump-probe delay the pump path length was decreased. In the case of a decay scan the total photoelectron count over the detector was recorded per second. The stage was run at a speed of 0.0001 mm/s.

The pump and probe beams were aligned through two irises, one either side of the vacuum chamber. These were aligned so the image was cylindrically symmetrical on the detector and bisecting the molecular beam perpendicularly. Once aligned a 250 mm focusing lens was used to weakly focus the beam into the interaction region. A power

density of 4×10^{9} W/cm^{-2} was achieved assuming a mildly focused beam in the interaction region with a volume of 6×10^{-10} m^{3}.

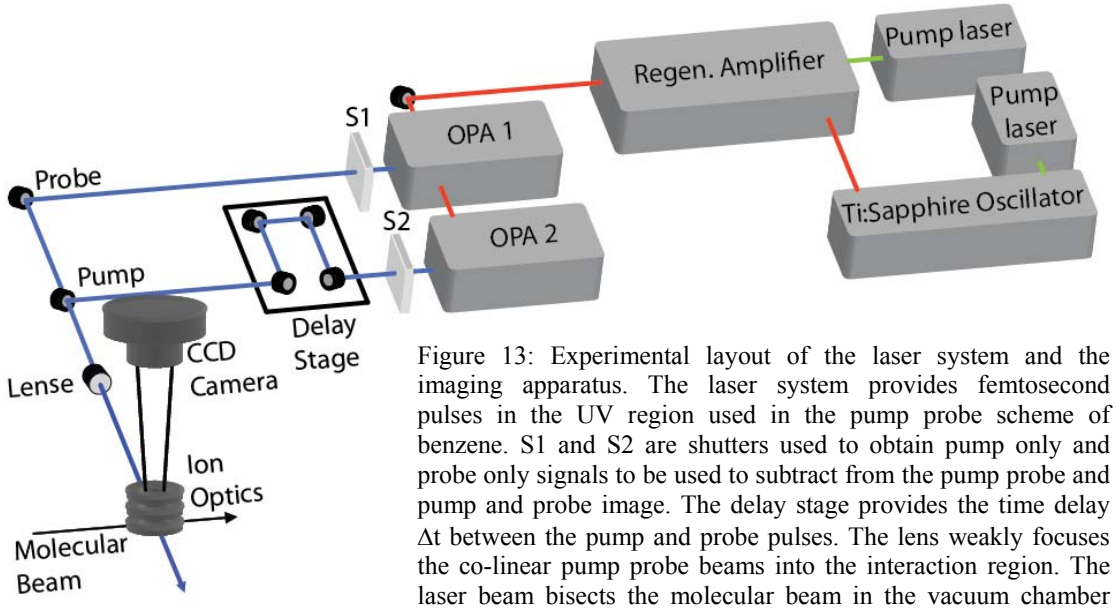

Figure 13: Experimental layout of the laser system and the imaging apparatus. The laser system provides femtosecond pulses in the UV region used in the pump probe scheme of benzene. S1 and S2 are shutters used to obtain pump only and probe only signals to be used to subtract from the pump probe and pump and probe image. The delay stage provides the time delay Δt between the pump and probe pulses. The lens weakly focuses the co-linear pump probe beams into the interaction region. The laser beam bisects the molecular beam in the vacuum chamber and is in between the repeller and extractor plates of the ion optics. The photoelectrons are imaged by a CCD camera and recorded.

2.3 Pulse diagnostics

2.3.1 Pulse characterisation

To fully characterise the electric field of an ultrashort pulse, its phase and intensity in both the time and frequency domain must be known[4]. Frequency, ω, and time, t, are Fourier transform pairs of each other, in the case of the description of an electric field:

$$\tilde{\varepsilon}(\omega) = \int_{-\infty}^{\infty} \varepsilon(t)\exp(-i\omega t)dt \tag{2.14}$$

$$\varepsilon(t) = \int_{-\infty}^{\infty} \tilde{\varepsilon}(\omega)\exp(i\omega t)d\omega \tag{2.15}$$

The pulse electric field in the frequency domain, $\tilde{\varepsilon}(\omega)$, is the inverse Fourier transform the pulse electric field in the time domain $\varepsilon(t)$. The pulse electric field in the frequency domain can be described in intensity and phase as:

$$\tilde{\varepsilon}(\omega) = \sqrt{S(\omega)\exp[-i\varphi(\omega)]} \tag{2.16}$$

Where *S(ω)* is the spectrum and $\varphi(\omega)$ is the spectral phase. The spectrum contains both positive and negative regions. Since we are concerned with observables only the real electric field of the negative component is omitted. This reduces the spectral intensity to:

$$S(\omega) = |\tilde{\varepsilon}(\omega)|^2 \tag{2.17}$$

While the spectral phase is given as:

$$\varphi(\omega) = -\arctan\left\{\frac{\mathrm{Im}[\tilde{\varepsilon}(\omega)]}{\mathrm{Re}[\tilde{\varepsilon}(\omega)]}\right\} \tag{2.18}$$

Here Im refers to the imaginary and Re to the real components. Equation (2.18) can be simplified to:

$$\varphi(\omega) = -\mathrm{Im}\{\ln[\tilde{\varepsilon}(\omega)]\} \tag{2.19}$$

When describing the ultrashort pulse in the time domain the pulse envelope is used to describe the pulse instead of the rapidly varying carrier wave $\exp(i\omega_0 t)$. This assumption is valid for pulses whose features are longer than the carrier wave frequency and accounts for our time scale where pulses are not achieved below 30 fs. The complex conjugate term is removed in the analytical signal approximation, since we are concerned with the

real term only. The pulse electric field in the time domain, $E(t)$ can be written in terms of intensity, $I(t)$, and phase, $\varphi(t)$, as:

$$E(t) = \sqrt{I(t)\exp[-i\phi(t)]} \tag{2.20}$$

The measured temporal intensity is related to the electric field by:

$$I(t) = |E(t)|^2 \tag{2.21}$$

The temporal phase can be described as:

$$\phi(t) = -\arctan\left\{\frac{\mathrm{Im}[\tilde{\varepsilon}(t)]}{\mathrm{Re}[\tilde{\varepsilon}(t)]}\right\} \tag{2.22}$$

And can be simplified to:

$$\phi(t) = -\mathrm{Im}\{\ln[\tilde{\varepsilon}(t)]\} \tag{2.23}$$

2.3.2 Spectral analyser

A spectrometer (Ocean Optics HR 4000) was used to measure the spectral intensity, $S(\omega)$. The spectral analyser diffracts the beam with a grating and records the intensity of each frequency component. The spectrometer was used in all measurements of the beams spectrum and example spectra of the three UV pulses used in chapter 3 are shown in figure 14.

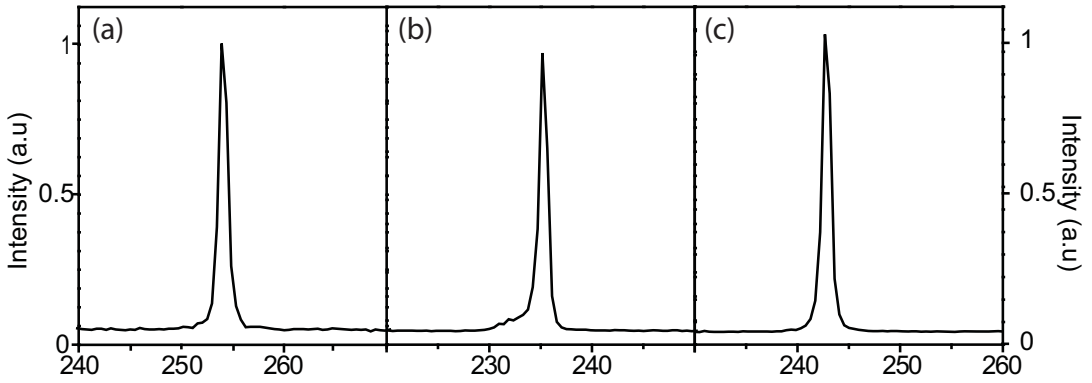

Figure 14: Spectra taken of the UV pulses used in the experiment described in chapter 3. (a) 254 nm. (b) 235 nm. (c) 243 nm.. All spectra have a bandwidth ~ 1 nm.

2.3.3 Autocorrelator

An intensity autocorrelator can be used to measure the time profile of an ultrashort pulse. This provides the amplitude in the time domain of the electric field. The pulse is split into two parts using a beam splitter, where one beam is scanned through the other within a nonlinear crystal by varying the path length of one of the beams. The intensity of the second harmonic generation is measured as a function of delay, τ, to give an autocorrelation function, $A(\tau)$:

$$A(\tau) = \int_{-\infty}^{+\infty} E(t)E^*(t-\tau)dt \tag{2.24}$$

The FWHM of the pulse in the temporal domain, $\Delta\tau$, is related to the width of the autocorrelation function, $\Delta\tau_{AC}$, by:

$$\Delta\tau_{AC} = \Delta\tau\sqrt{2} \tag{2.25}$$

An example of an autocorrelation of the residual 800 nm light is shown in figure 16 (a) and (b). A single shot autocorrelator was used to monitor the pulse length of the

regenerative amplifier and an intensity autocorrelator was used to measure the pulse duration of the beams in the visible region.

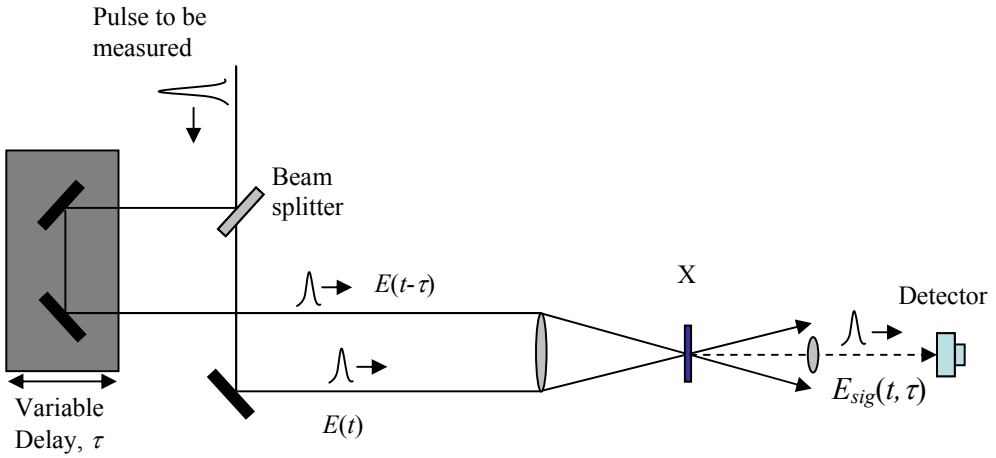

Figure 15: Schematic of autocorrelator / cross-correlator apparatus. In the case of autocorrelation the pulse to be measured is split using a beam splitter to yield two replica pulses $E(t-\tau)$ and $E(t)$. A variable path length is used to apply a variable time delay, τ, between the two pulses. The beams are focused into a SHG crystal, X. The intensity of the signal, $E_{sig}(t,\tau)$ is recorded by a detector to yield the autocorrelation function. For cross-correlation a collinear beam of the UV and fundamental pulses are incident onto the beam splitter. The path is the same and X is now a sum frequency generation crystal. The resulting signal has contributions from the auto-correlation function for the fundamental and two cross-correlation signals. These come from the overlap of the UV on the upper path and fundamental on the lower path and vice versa. The three signals are separated by time gaps and easily identifiable.

To measure the temporal length of the pulses in the UV region a cross-correlation is used. A reference pulse at 800 nm is mixed with a UV pulse to create a difference frequency generation (SFG) signal. The same apparatus as shown in figure 15 is used except X is replaced with a SFG crystal. The two pulses must be within 5 ps of each other temporally. The UV and 800 nm beams are directed into the apparatus collinearly. The autocorrelation signal $A(t)$ is related to the intensity of the reference pulse and intensity of the UV pulse $I(t-\tau)$ by:

$$A(\tau) = \int_{-\infty}^{+\infty} E_{ref}(t) E^*(t-\tau) dt \qquad (2.26)$$

The autocorrelation of the reference 800 nm pulse in the collinear beam is measured prior to taking the cross correlation with an autocorrelator. The temporal width of the reference pulse, $\Delta\tau_{ref}$ is used to deconvolute the SFG signal temporal width, $\Delta\tau_{XC}$:

$$\Delta\tau_{XC} = \sqrt{\Delta\tau^2 + \Delta\tau^2_{ref}} \tag{2.27}$$

Figure 16 shows two cross correlation measurements for the 243nm and 235 nm beams used in chapter 3.

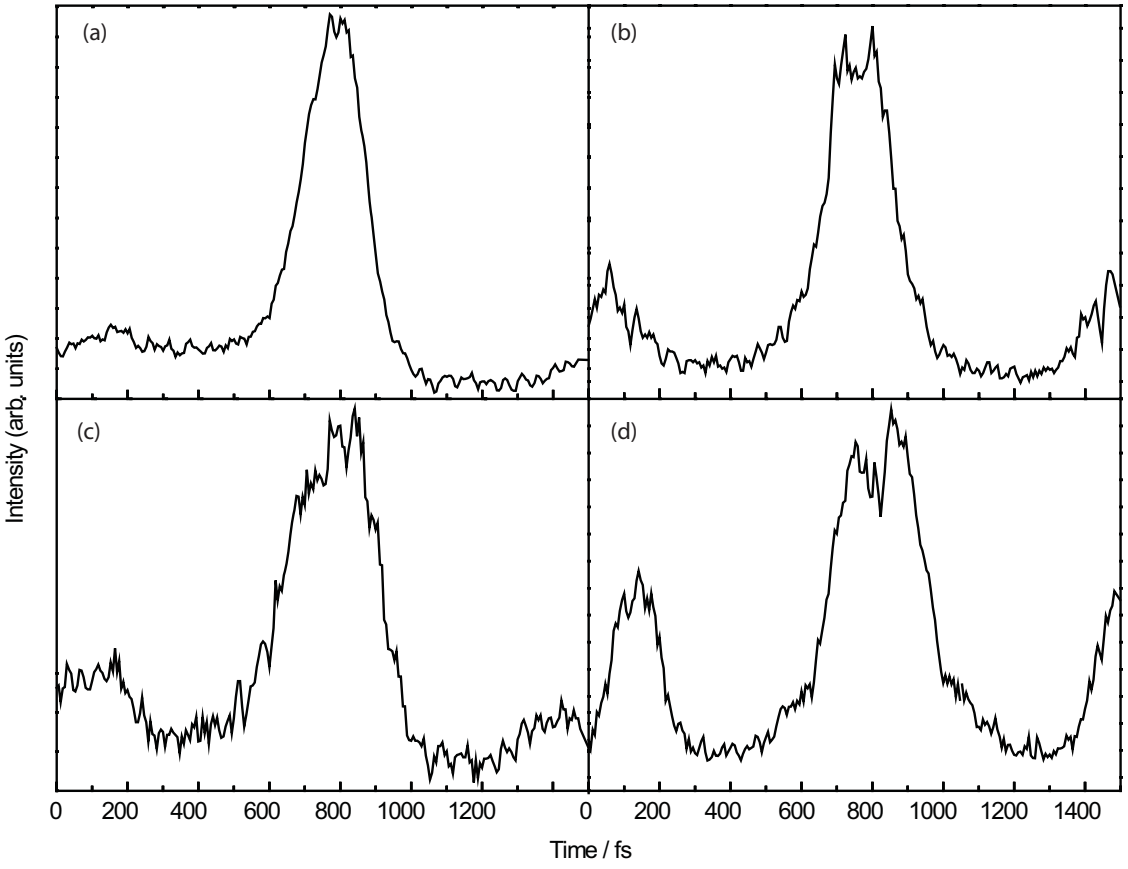

Figure 16: Plot of auto and cross correlations. (a) Autocorrelation of the residual 800 nm light in the 235 nm beam with a τ = 131 fs. (b) Autocorrelation of the residual 800 nm light in the 235 nm beam with a τ = 205 fs. (c) Cross correlation of the residual 800 nm in the 243 nm beam with a τ = 270 fs. (d) Cross correlation of both the residual 800 nm and the 243 nm beam with a τ = 200 fs. These measurements afforded a FWHM of the pulse duration of τ = 104 fs and τ = 133 fs respectively.

Autocorrelators provide an accurate measurement of the time duration of a pulse assuming a Gaussian profile. They do not however give any indication of the relative phases of the frequency components of the pulse. The time domain and spectral profiles give no indication of relative phase so are not capable of providing enough information for the determination of the electric field.

2.3.4 XFROG and inversion algorithm

The most important pulse diagnostics come from a frequency resolved optical gating (FROG) set-up, this provides both temporal and frequency information simultaneously. A conceptual view of this process is that a spectrum of the autocorrelation function is taken for several time intervals. A commercial FROG was used to characterise an 800 nm pulse which is used to frequency mix with segments of the shaped and doubled 254 nm pulse in the time domain. A home-built cross correlation frequency-resolved optical-gating (XFROG) configuration was used to fully characterise the unknown UV pulse. This process provides a series of spectra that can be plotted versus delay, *t*, on a 2D plot of intensity against frequency and delay. Phase and amplitude of the pulse were obtained using a 2D phase retrieval algorithm (Swamp Optics).

2.3.5 GRENOUILLE

GRENOUILLE (Swamp Optics UPM 8-20) is the acronym for GRating-Eliminated Nononsense Observation of Ultrafast Incident Laser Light E-fields[4]. It performs the same operations on the light pulse as a conventional FROG but benefits from minimal alignment through its ingenious use of Fourier optics. This instrument was used to fully characterise the 800 nm reference beam. The nonlinear process utilised is SHG which cannot be used to characterise pulses in the UV. The Fresnel bi-prism performs the task of the beam splitter, delay-line and re-collimation optic. The beam is split into two beamlets that are directed into the thick SHG crystal so they overlap spatially and temporally in the crystal (figure 17 Top View). The two wide beamlets crossing each other at an angle has an effect of mapping relative beam delay onto horizontal position

within the crystal as shown in figure 17. For long pulse durations the width of bandwidth that overlaps increases giving a wider SHG signal, conversely for shorter pulse durations a smaller width overlaps.

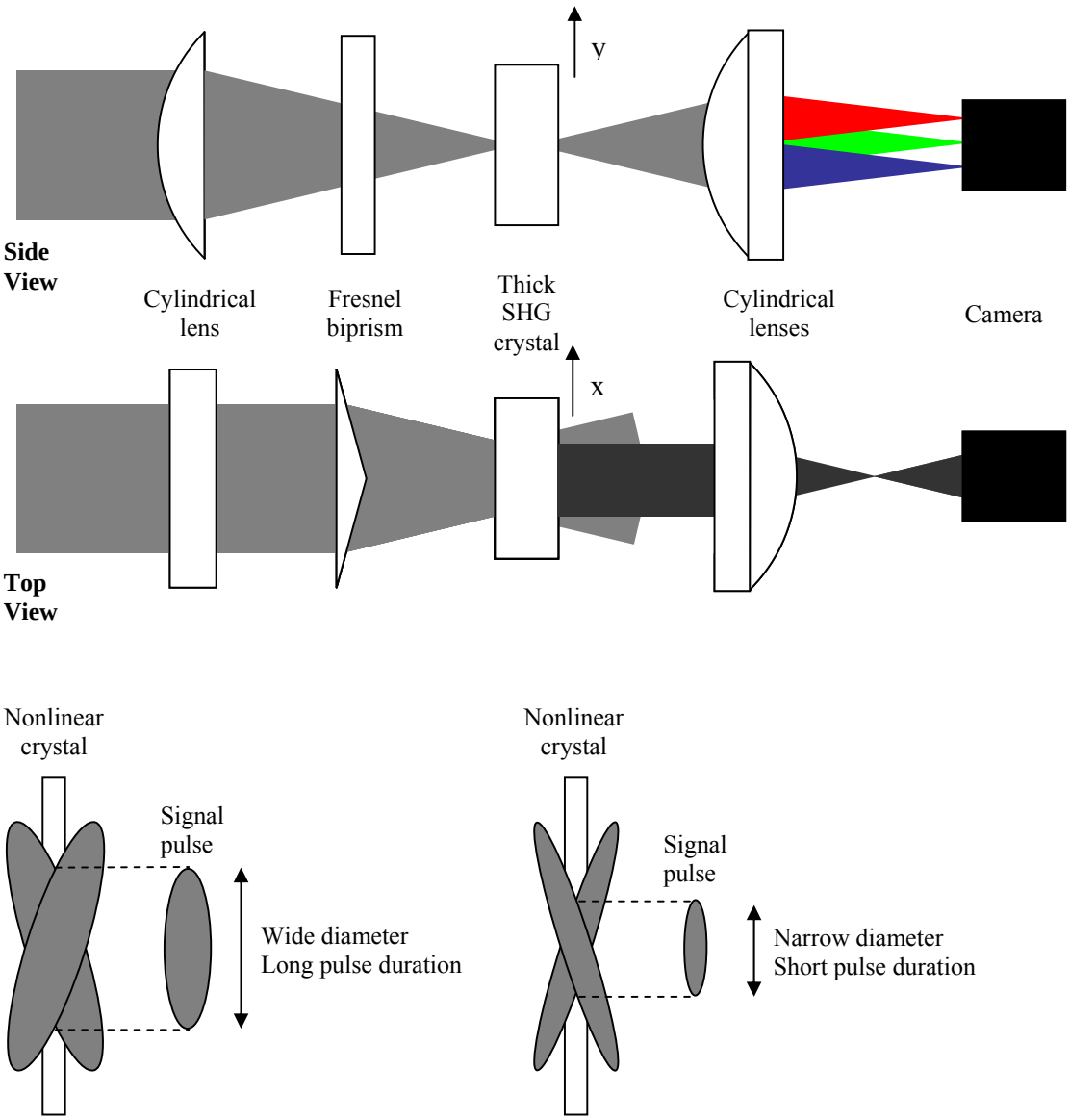

Figure 17: Schematic of the GRENOUILLE apparatus and principal of operation. Top figure: Side view shows the frequency resolving dimension. A cylindrical lens focuses the beam into a thick SHG crystal. The frequency components phase match at different depths in the crystal. The thickness of the crystal effectively diffracts the beam since different frequencies travel through varying amounts of material . The sharp angle of incidence further exaggerates this effect. The signal diverges until reaching a cylindrical lens which focuses the individual frequency components onto a detector. Middle figure: Top view shows time resolving dimension. The beam passes through the cylindrical lens unaffected. A Fresnel bi-prism focuses the beam into the thick. As illustrated in the bottom figure, the pulse duration is proportional to the signal width in the *x* dimension. The longer the pulse is the greater the overlap area within the thick SHG crystal and so the wider the generated signal (bottom left figure). The contrary holds, that the shorter the pulse duration the less overlap in time of the two pulses in the SHG crystal and over a smaller area hence a small width signal (bottom right figure).

A cylindrical lens placed before the Fresnel bi-prism focuses the beam into the SHG crystal in the *y* axis so that a variety of incidence angles are obtained. A thick SHG crystal is used due to its relatively small phase-matching bandwidth, so the phase-matched wavelength of the SHG signal varies with angle. The range of angles must be large enough and the crystal thick enough for the different wavelength components to exit the crystal at different angles. The generated second harmonic wavelengths are diffracted out spatially. The SHG wavelength components leaving the crystal at different vertical positions are focused into the camera with a final lens and their position mapped to wavelength. The map of wavelength against time, a spectrogram of the SHG pulse, was deconvoluted using pulse characterisation software (Mesaphotonics VideoFrog version 6.0) to give a spectrogram of the reference pulse.

The IR pulse was characterised completely using a commercial GRENOUILLE (Swamp Optics UPM 8-20) and pulse characterisation software (Mesaphotonics VideoFrog version 6.0), and thus acts as a reference pulse. The DFG spectrogram and the measured electric field of the reference pulse were used as input for an XFROG inversion algorithm (FROG3 program from Femtosoft Technologies) to retrieve the electric field of the UV shaped pulses.

The GRENOUILLE trace used within the pulse characterisation software is shown below in figure 18. The raw trace is shown in panel (c) and the retrieved spectral intensity (black line) and phase (red line) is shown in panel (a). Panel (b) shows the time intensity intensity (black line) and phase (red line). The phase in both the time and frequency domains shows a small quadratic chirp. This most likely caused from the long beam path length and from passing through beam splitters. The pulse duration is 71.21 fs as calculated by the pulse characterisation software.

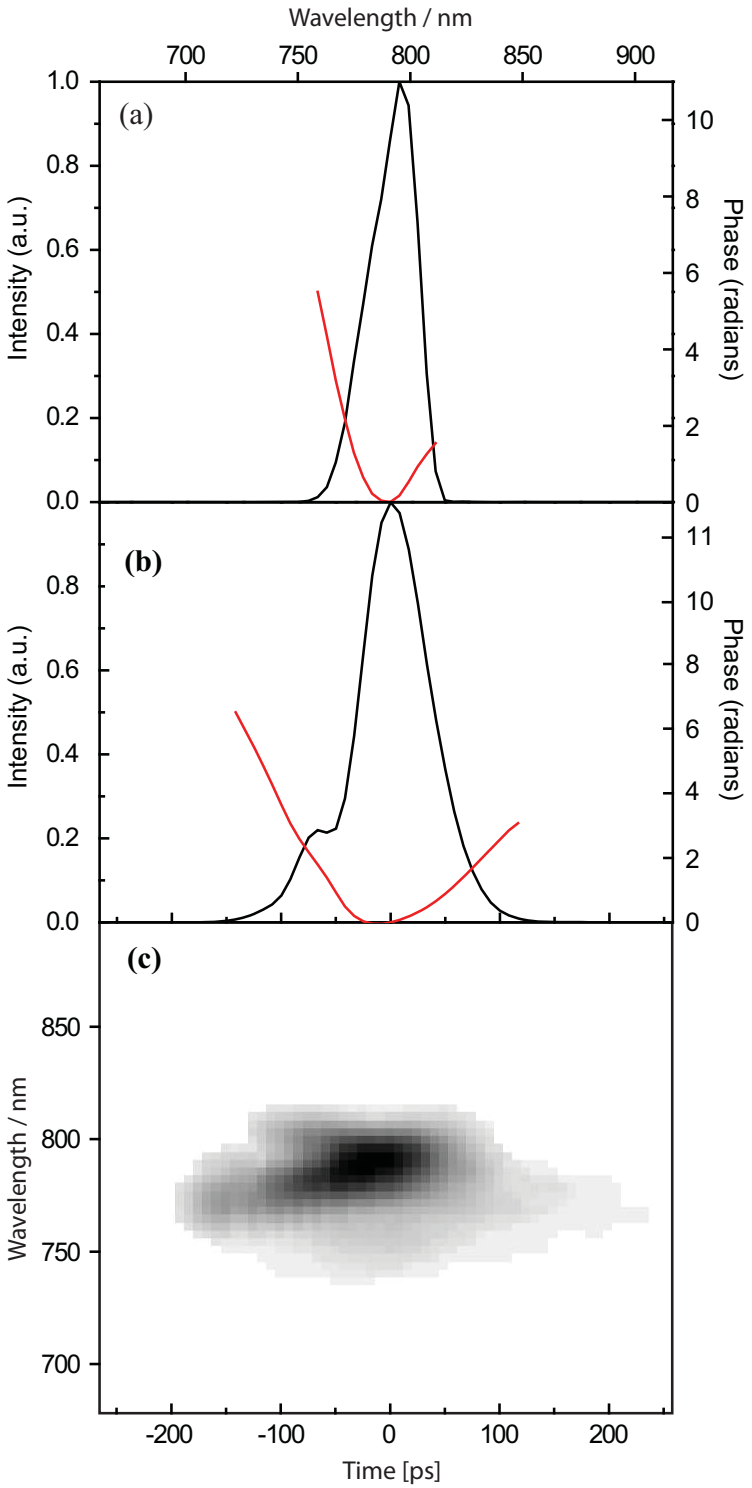

Figure 18: GRENOUILLE trace of the fundamental 800 nm pulse used in the XFROG measurement. (a) Spectral intensity (black line) and phase (red line) (b) Temporal intensity (black line) and phase (red line. Pulse width: 71.21 fs, Bandwidth: 11.98 THz, Bandwidth: 25.26 nm, Autocorrelation width: 119.11 fs, Time bandwidth product: 0.85. (c) Raw GRENOUILLE trace.

2.3.6 XFROG

The XFROG pulse characterisation technique can be thought of as a spectrally resolved cross correlation[4]. A reference pulse is first characterised in a GRENOUILLE so its amplitude and phase profile (spectrogram) was known. A spectrogram of the DFG signal from mixing the reference pulse and the unknown pulse in a nonlinear crystal was recorded. The reference spectrogram and DFG signal spectrogram were deconvoluted to obtain a spectrogram of the UV electric field using an XFROG inversion algorithm (FROG3 program from Femtosoft Technologies). The electric field for the XFROG signal is:

$$E_{Sig}^{DFG}(t,\tau) = E(t)E_{ref}^{*}(t-\tau) \tag{2.28}$$

Here $E_{Sig}^{DFG}(t,\tau)$ is the electric field of the DFG signal, $E_{ref}^{*}(t-\tau)$ is the electric field of the reference pulse and $E(t)$ is the electric field of the unknown pulse. The spectrogram of the unknown pulse is deconvoluted using the relationship:

$$I_{XFROG}^{DFG}(\omega,\tau) = \left| \int_{-\infty}^{\infty} E(t)E_{\mathrm{Re}\,f}^{*}(t-\tau)e^{-i\omega t}\,dt \right|^{2} \tag{2.29}$$

Where the DFG spectrogram $I_{XFROG}^{DFG}(\omega,\tau)$ is yielded from the squared magnitude of the spectrum of the cross correlation signal recorded as a function of delay τ between the two pulses. An experimental benefit of the XFROG is that the magnitude of the signal recorded is proportional to the reference beam as well as the unknown pulse. So pulse energies on the nano joule scale were easily recorded. The central wavelength recorded by the spectrometer of the DFG signal was ~373 nm, which can be calculated from the relationship:

$$\omega_0^{DFG} = \omega - \omega_{\mathrm{Re}\,f} \tag{2.30}$$

An example XFROG trace of an unshaped UV pulse centred at 254 nm is shown in figure 19. The reconstructed spectral intensity (black line) and phase (red line) are shown in (a) and the temporal intensity (black line) and phase (red line) are shown in (b). The raw XFROG trace is shown in (c).

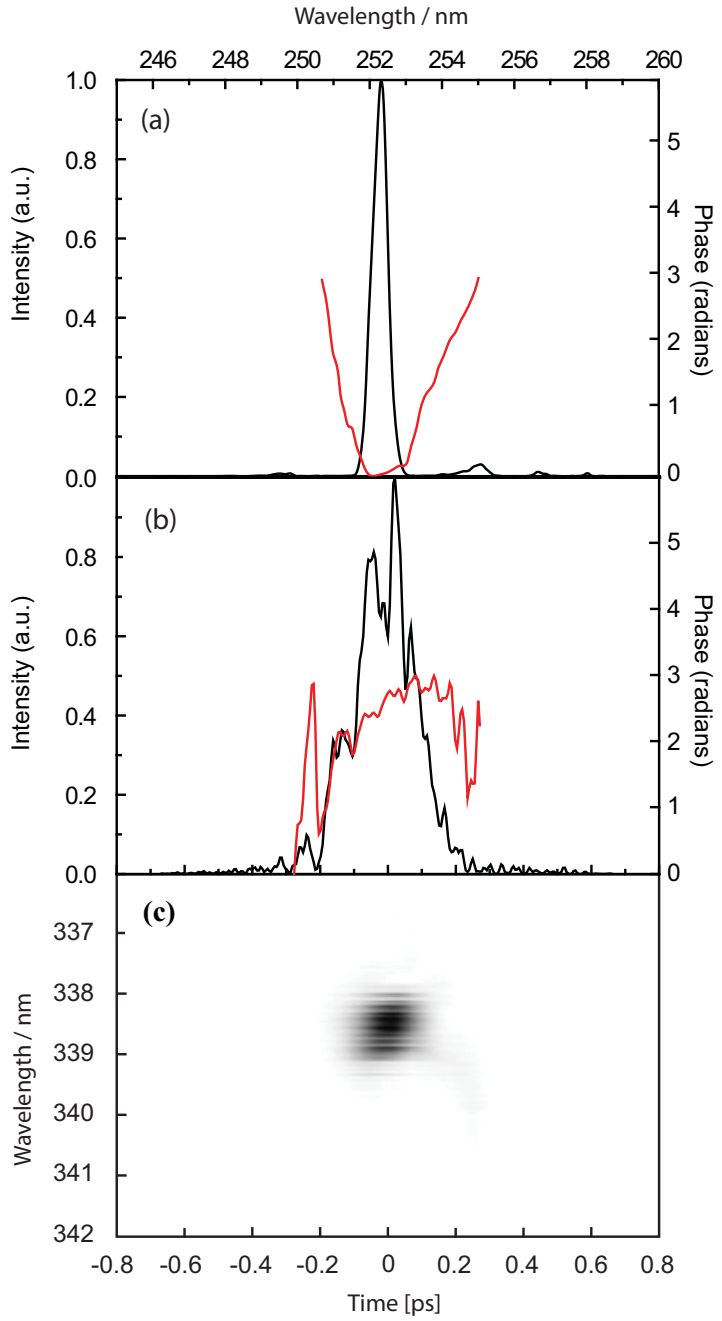

Figure 19: XFROG trace of the unshaped 254 nm pulse used from the pulse shaping apparatus (described in chapter 4). (a) Reconstructed spectral intensity (black line) and phase (red line) (b) Reconstructed temporal intensity (black line) and phase (red line).

The pulse shaping apparatus and XFROG set-up are shown in figure 20. To obtain a DFG signal the reference 800 nm pulse and the unknown UV pulse must be overlapped in time and space in the DFG crystal. Both pulses originate from the amplifier where are subsequently they are split. The pulse used to generate the shaped UV pulse first travels through an OPA and then the pulse shaper. This amounts to a significantly long path length that must be matched by the reference pulse in order to overlap the two pulses in time. To do this the reference pulse was reflected 8 times between a pair of wide mirrors coated for 0° angle of incidence. The final adjustment of time was made using a motorised delay stage. The beams were focused into a 10 μm DFG crystal mounted on fused silica using 75 mm focal length spherical mirrors. The 800 nm pulse was weakly focused into the crystal and the power attenuated so there was no white light generation. The UV pulse was focused into the crystal with a 75 mm focal length spherical mirror. The weakly focused beam gave a wider spot size than the focused UV beam which aided in beam alignment. Both beams were overlapped spatially onto the face of the DFG crystal. The two beams were at an angle of 30° to each other. This gave a DFG signal that was spatially separate from the two incident beams allowing for its simple separation. The DFG signal beam was directed onto a final spherical mirror by a small mirror, where it was focused into the optical fibre of a spectrometer. The signal from a photodiode was used to get the two pulses to within a nanosecond of each other and as close to a time delay of zero ($\tau = 0$) as possible. The imaging apparatus was then used to find a coherent spike caused by the overlap in time of both beams. This method was very accurate and it was found that $\tau = 0$ always lay around 500 fs from the coherent spike position. With this initial position the delay stage was scanned until a DFG signal was seen by eye as fluorescence on paper. The crystal angle, in all Cartesian coordinates, was optimised along with the input beam angle to obtain the brightest visible DFG signal at the focal spot. The beam was directed into the spectrometer, to achieve maximum signal. Care was taken to align the spectrometer along the same axis as the beam. The reference pulse was generally attenuated using neutral density filters once good alignment had been achieved to reduce saturation in the spectrometer. The reference beam generally had a Gaussian beam profile in time and frequency leading to optimum XFROG spectrograms and ideal

for use in the phase retrieval algorithm. The collection of spectra and stage movement were automated using a Labview program.

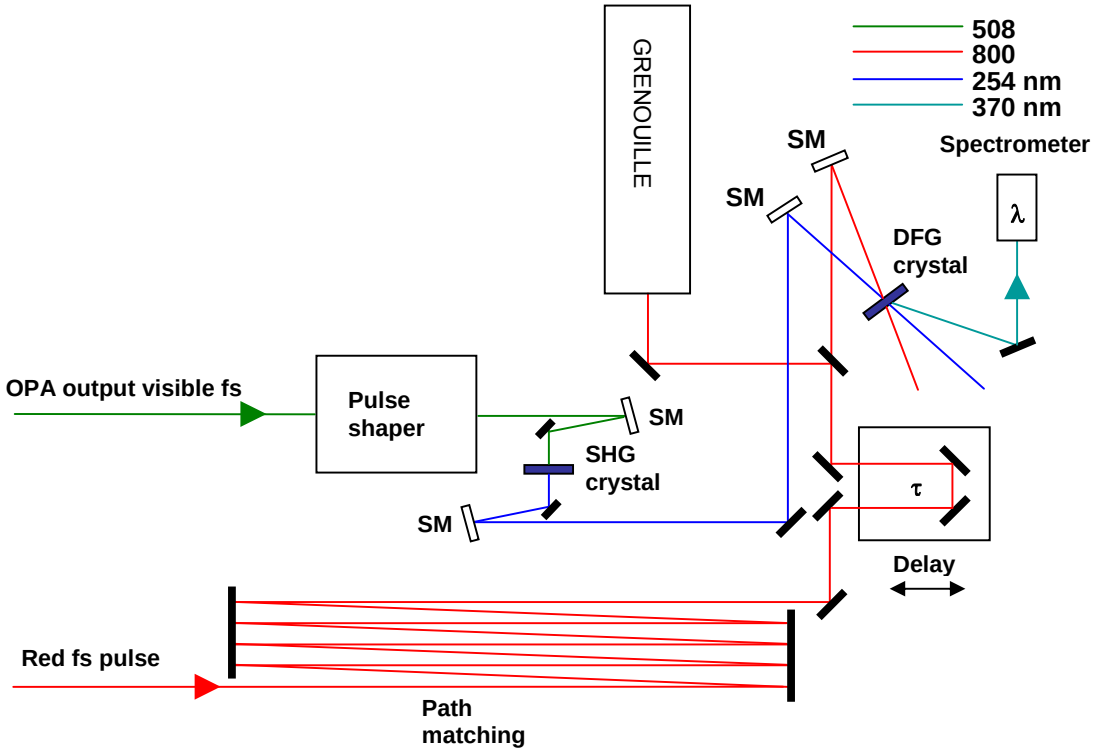

Figure 20: Experimental setup for the generation and characterisation of shaped UV pulses at 254 nm. The optical path length is described in detail in the text. All thick black rectangles represent mirrors, open rectangles spherical mirrors and dark blue rectangles non linear crystals. SLM; liquid crystal spatial light modulator, G; grating, M; mirror, CM; cylindrical mirror.

2.4 References

1 A. Eppink and D. H. Parker, *Review of Scientific Instruments*, 1997, **68**, 3477-3484.

2 G. A. Garcia, L. Nahon and I. Powis, *Review of Scientific Instruments*, 2004, **75**, 4989-4996.

3 V. Dribinski, A. Ossadtchi, V. A. Mandelshtam and H. Reisler, *Review of Scientific Instruments*, 2002, **73**, 2634-2642.

4 R. Trebino, K.A.P publishers, *Frequency-Resolved Optical Grating: The Measurement of Ultrashort Laser Pulses*, (2001)

5 A. Nunn, H. H. Fielding, *Femtochemistry and the control of chemical reactivity*, from *Tutorials in molecular reaction dynamics*, Edited by Mark Brouard and Claire Vallance, RSC, submitted for publication.

Chapter 3

Ultrafast intersystem crossing in benzene

The ultrafast intramolecular dynamics of electronically and vibrationally excited benzene are investigated using time-resolved photoelectron spectroscopy. In addition to an ultrafast initial decay we observe an oscillation between two states. The most plausible explanation of the data is that the photophysical pathway involves an ultrafast intersystem crossing from the initially populated singlet state to an optically dark triplet state. Our experimental findings have been supported by quantum dynamics simulations. Our results challenge the currently accepted view that the initial ultrafast decay from the excited state is dominated by internal conversion through a singlet-singlet conical intersection taking the population directly back to the ground state.

3.1 Introduction

The dynamics of intramolecular energy transfer has attracted widespread attention. Much effort has been concerned with determining the time scale for energy redistribution and/or the channels through which energy flows among various degrees of freedom in isolated molecules. Such unimolecular reactions, in which the reactants and products differ only in the distribution of energy in the rotational, vibrational and electronic degrees of freedom, represent the simplest and most fundamental of all chemical reactions.

In this chapter, the non radiative ultrafast decay route from benzenes first excited state, at around ~3000 cm^{-1} above the origin that is referred to as channel 3 is investigated. The decay mechanism is rationalised to be a previously unexpected process. Our interpretation challenges preconceptions on the nature of ultrafast intersystem crossing in organic polyatomic molecules.

In this introductory section, the molecular properties of benzene will be discussed from early spectroscopic studies employing low resolution spectroscopy techniques; including the symmetry effects of the first excited state and how the Herzberg-Teller mechanism gives rise to the bulk of the absorption spectrum. The focus will then fall more specifically on a time domain perspective and onto some of the many investigations into the channel 3 process.

3.1.1 Spectroscopy of benzene

Benzene is an aromatic planar molecule in the form of a regular hexagon. It possesses a conjugated π-electron system which determines its electronic properties. Hückel theory can be used to calculate the orbital energies of the molecule. This method ignores sigma bonds (sigma-π separability) and uses a method of linear combination of atomic orbitals to build up the π–molecular orbitals. For benzene, using Hückel theory the six orbitals on the carbon atoms and perpendicular to the plane of the molecule are shown below:

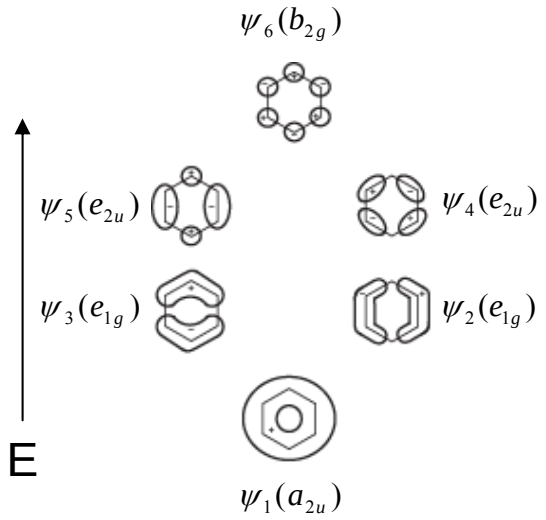

Figure 1: Hückel MOs in the benzene molecule. The states increase in energy with greater number of nodal planes. The symmetry species has been indicated in each case[33].

Figure 3.1.1 illustrates the MO wave functions and gives the symmetry species, according to the D_{6h} point group. The π-type MOs in planar benzene are antisymmetric to reflection in the plane of the molecule. The wavefunctions above the plane of the molecule are shown and those below are opposite in sign but identical in shape. The energy increases with the number of the nodal planes. The ground electron configuration of benzene is obtained by feeding the six electrons into the lower energy MOs, giving

$$\ldots (1a_{2u})^2 (1e_{1g})^4 \tag{3.1}$$

and the ground state is labelled $\widetilde{X}^1 A_{1g}$.

The first excited configuration is

$$\ldots (1a_{2u})^2 (1e_{1g})^3 (1e_{2u})^1 \tag{3.2}$$

The states arising from this configuration can be considered the same as those from $(1e_{1g})^1 (1e_{2u})^1$ since the single vacancy can be treated like a single electron. Group theory can be used to find the symmetry species of the allowed electronic states. This is carried

out by finding the components of the direct product of the two occupied degenerate levels:

$$\Gamma(\psi_e^0) = e_{1g} \times e_{2u} = B_{1u} + B_{2u} + E_{1u} \tag{3.3}$$

where ψ_e^0 represents the electronic wavefunction. The spins of the electrons in the e_{1g} and e_{1u} orbitals can be either parallel (triplet) or antiparallel (singlet) which results in six possible states $^{1,3}B_{1u}$, $^{1,3}B_{2u}$ and $^{1,3}E_{1u}$. The triplets can be neglected since the ground state is a singlet i.e. not optically accessible according to $\Delta S = 0$. The singlet states are, in order of increasing energy, $\widetilde{A}^1B_{2u}$, $\widetilde{A}^1B_{2u}$ and $\widetilde{C}^1E_{1u}$.

In benzene, the $\widetilde{A} - \widetilde{X}$ and $\widetilde{B} - \widetilde{X}$ systems are electronically forbidden since neither B_{2u} nor B_{1u} (or E_{2g}) is a translational symmetry species but the transitions do still occur through vibronic interaction. They are seen in the 227-267 nm (S_1) and 185-205 nm (S_2) regions of the spectrum, respectively. The transitions occur because the molecular framework of the benzene molecule is not rigid. The molecular vibrations distort the D_{6h} molecular symmetry to a lower type resulting in a relaxation of the symmetry selection rules. This, in effect is due to a breakdown of the Born-Oppenheimer separation of electronic and vibrational motions. They gain their intensity by mixing with the $\widetilde{C}^1E_{1u}$ state which is an electronically allowed transition and shall be discussed in more detail in section 3.1.4.

3.1.2 A vibronically allowed transition

The transition moment R_{ev} for an electric dipole transition between an upper and lower vibronic state, with vibronic wave functions ψ'_{ev} and ψ''_{ev} respectively, is given by

$$R_{ev} = \int \psi'^{*}_{ev} \mu \psi''_{ev} d\tau_{ev} \tag{3.4}$$

where μ is the electric dipole moment operator and the integration is over electronic and vibrational coordinates. For R_{ev} to be non-zero, and for the transition to be allowed, the product of the symmetry species for the quantities inside the integral must be totally symmetric. The integral in equation 3.4 can be written as:

$$R_{ev} = R_e \int \psi_v'' \psi_v' d\tau_v \tag{3.5}$$

Here, the product of the electronic transition moment is assumed to be independent of nuclear motion, and the vibrational overlap integral (Born Oppenheimer approximation). If the electronic transition moment integral is totally symmetric, then so are all vibronic transition moment integrals. All vibronic transitions associated with allowed electronic transitions are allowed by symmetry but, their intensities are governed by the Franck-Condon principle. The intensities of bands in progressions are proportional to the square of the vibronic transition moment of equation 3.5.

The general symmetry requirement for a vibronic transition to be allowed by electric dipole selection rules is that the integral equation 3.4 contains the totally symmetric species. Since the symmetry species of μ is that of a translation it follows that:

$$\Gamma(\psi_{ev}') \times \Gamma(\psi_{ev}'') \supset \Gamma(T_\alpha) \tag{3.6}$$

where $T_\alpha = T_x, T_y, T_z$. The symmetry species for a vibronic state is always given by:

$$\Gamma(\psi_{ev}) = \Gamma(\psi_e) \times \Gamma(\psi_v) \tag{3.7}$$

Irrespective of whether the Born-Oppenheimer approximation holds so that equation 3.6 becomes:

$$\Gamma(\psi_e') \times \Gamma(\psi_v') \times \Gamma(\psi_e'') \times \Gamma(\psi'') \supset \Gamma(T_\alpha)_v \tag{3.8}$$

Fulfilment of these additional symmetry rules allow for a band system that is electronically either forbidden or allowed to show vibrationally induced bands involving non-totally symmetric vibrations. A vibronic transition may be allowed but that does not mean it possesses intensity.

3.1.3 Herzberg-Teller intensity stealing

Herzberg-Teller intensity stealing[35] is the phenomenon of obtaining intensity by vibronic transitions. Herzberg and Teller explained that, when the vibrational overlap integral of equation 3.4 is non-totally symmetric, the electronic transition moment R_e is no longer independent of vibrational motion. The effect of vibrational motion is taken account of by expanding R_e as a Taylor series, in the normal coordinates Q_k,Q_l….of the vibrations involved, as follows:

$$
\begin{aligned}
R_e &= (R_e)_{eq} && \text{zero order} \\
&+ \sum_k \left(\frac{\partial R_e}{\partial Q_k} \right)_{eq} Q_k && \text{first order} \\
&+ \frac{1}{2!} \sum_{k,l} \left(\frac{\partial^2 R_e}{\partial Q_k \partial Q_l} \right)_{eq} Q_k Q_l && \text{second order} \\
&+ \frac{1}{3!} \sum_{k,l,m} \left(\frac{\partial^3 R_e}{\partial Q_k \partial Q_l \partial Q_m} \right)_{eq} Q_k Q_l Q_m && \text{third order} \\
&+ \ldots && (3.9)
\end{aligned}
$$

Where *eq* refers to the equilibrium geometry of the molecule and the order of each term with respect to normal coordinates is indicated. This Taylor expansion implies that, the calculated electronic transition moment, R_e for one particular geometry will be different to another. The first order term in the expansion is responsible for the majority of the intensity and so is more important than higher order terms. For a vibrational symmetry that is a result of a quanta of two different vibrational modes then the second order term would be involved in the equation. For two different vibrational modes then the third order term would come into play. In the $\tilde{A}^1B_{2u} - \tilde{X}^1A_{1g}$ system of benzene, second- and

third-order terms cause the very weak but observable, vibronic transitions. By removing everything but the first order term the series can be shown as:

$$R_{ev} = \int \psi_v' \left[(R_e)_{eq} + \sum_k \left(\frac{\partial R_e}{\partial Q_k} \right)_{eq} Q_k \right] \psi_v'' d\tau_v \tag{3.10}$$

The vibrations can now be separated into those which are totally symmetric (s) and those which are non totally symmetric (a). Then equation 3.10 becomes:

$$R_{ev} = (R_e)_{eq} \int \psi_v' \psi_v'' d\tau_v + \sum_s \left(\frac{\partial R_e}{\partial Q_s} \right)_{eq} \int \psi_v' Q_s \psi_v'' d\tau_v + \sum_a \left(\frac{\partial R_e}{\partial Q_a} \right)_{eq} \int \psi_v' Q_a \psi_v'' d\tau_v \tag{3.11}$$

For the electronically forbidden transitions in benzene, $(R_e)_{eq} = 0$ and $(\partial R_e / \partial Q_s)_{eq} = 0$ and the first two terms on the right hand side of equation 3.11 are zero; however, the third term is non-zero and the transition is electronically forbidden but vibronically allowed.

3.1.4 Normal mode vibrations of benzene

Benzene possesses 30 vibrational modes: 10 degenerate modes and 10 non degenerate modes. The vibrational modes and their symmetries have been reproduced[1] below in figure 2 for reference throughout this chapter.

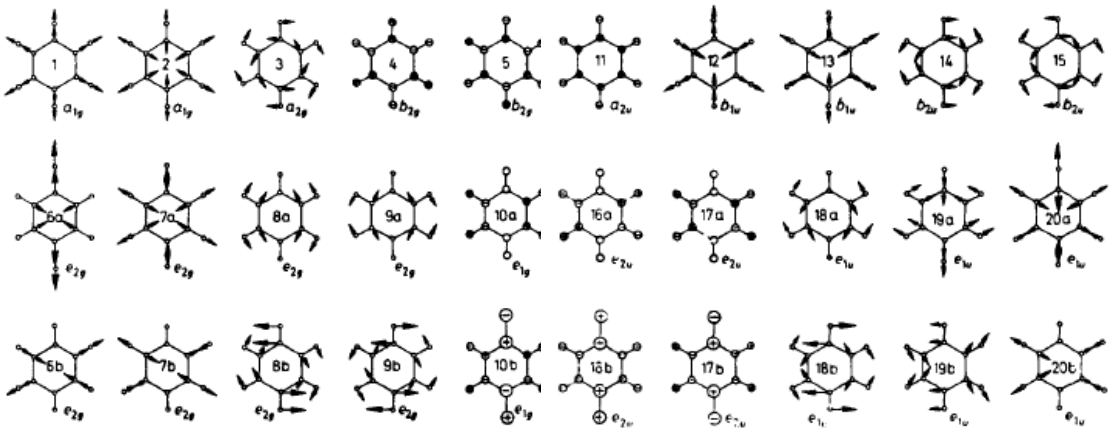

Figure 2: Benzenes vibrational modes. There are ten degenerate modes and ten non degenerate modes[1].

3.1.5 Low resolution absorption spectrum

The $\widetilde{A}^1B_{2u} - \widetilde{X}^1A_{1g}$ 260 nm band of the absorption spectrum of benzene can be accounted for by the intensity stealing mechanism just described in section 3.1.4. Figure 3 shows a reproduced portion of the absorption spectrum at low resolution from Callomons early work[3]. The frequency at which a pure electronic transition would be expected to occur has been indicated by 0_0^0, it is not present due to it being symmetry forbidden as discussed earlier.

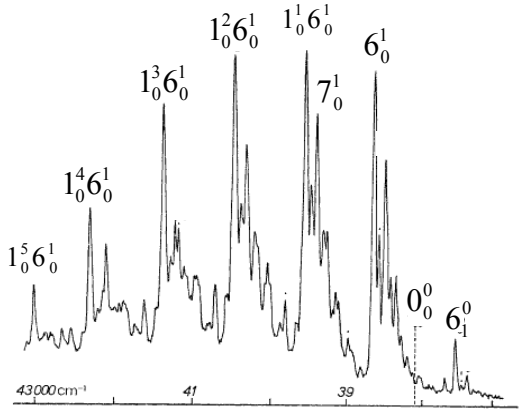

Figure 3: Low resolution $\widetilde{A}^1B_{2u} - \widetilde{X}^1A_{1g}$ absorption spectrum of benzene. The major peaks have been labelled. The spectrum is dominated by an intense 6_0^1 band due to Herzberg-Intensity stealing. The progression is due to mixing in with the totally symmetric ν_1 breathing mode. The false origin of where the electronically allowed vibrationless transition would be has been indicated[4].

To the high wavenumber of the 0_0^0 position is an intense band 6_0^1 (using the vibrational numbering scheme introduced by Wilson[5] which should be noted is different from the Mulliken scheme), where ν_6 is an e_{2g} vibration. Note: that we use the notation $\nu_{\nu''}^{\nu'}$ where n is the vibration labelled using Wilson notation and ν'' is the vibration quanta in the lower electronic state and ν' is the vibration in the upper state.

Since

$$B_{2u} \times e_{2g} = E_{1u} \tag{3.12}$$

and $E_{1u} = \Gamma(T_x, T_y)$, in the D_{6h} point group the 6_0^1 transition is symmetry allowed. This represents a vibronic transition that is allowed, even though the pure electronic transition is forbidden. The intensity of the transition derives from Herzberg-Teller intensity stealing from the $\widetilde{C}E_{1u} - \widetilde{X}^1A_{1g}$ electronic transition caused by coupling of the 6^1, $^1E_{1u}^{ev}$, vibronic state with the $\widetilde{C}^1E_{1u}^e$ electronic state. The hot band 6_1^0 also derives intensity from the $\widetilde{C} - \widetilde{X}$ transition but is weakened, in absorption, by the Boltzmann factor ($\tilde{\nu}''$ = 608 cm^{-1}). In the $\widetilde{A} - \widetilde{X}$ system in emission (fluorescence) the 6_1^0 band is intense and the 6_0^1 band weakened, if there is equilibrium population among vibrational levels by the Boltzmann factor ($\tilde{\nu}_6'$ = 521 cm^{-1}). Benzene has four e_{2g} vibrations all of which could, like ν_6, be involved in Herzberg-Teller intensity stealing. In fact the other three, ν_7, ν_8 and, ν_9 lead to false origins at least an order of magnitude weaker than those due to ν_6. This is because $(\partial R_e / \partial Q_k)_{eq}$ is much smaller for the other three vibrational modes. Note that the 7_0^1 transition can be observed in figure 3.

The progression structure in the remainder of the plot is the result of the totally symmetric ν_1 breathing mode. The progression is caused by an increase in the *r*(CC) bond length on excitation from the ground to the first excited state, the breathing mode which has a_{1g} symmetry and involves very little stretching of the *r*(CH) bonds.

3.1.6 Intramolecular dynamics: Channel 3

Although such a common component of the chemical structure of large polyatomic organic molecules, the intramolecular dynamics of benzene following excitation to the first excited state is still not fully understood. Its photochemistry has been studied now for 5 decades by many eminent scientists and has stood as a benchmark for spectroscopic studies of large polyatomics. From these studies it has been found that large aromatic molecules have a common ultrafast non radiative decay mechanism within the first few hundred femtoseconds when excited with above a threshold in the first excited state. The rates of decay are energy dependent. A variety of processes attributed to this ultrafast

decay mechanism over the years have included internal conversion[5], intramolecular vibrational redistribution (IVR)[2, 6] and isomerisation[14,15,35].

Calloman in 1972 eloquently summarised the problem, using fluorescence spectra and line width measurements of isolated gas phase benzene[3]. Firstly, upon excitation from the zeroth order ground state ($^1A_{2g}$) to just into the first excited state ($^1B_{1u}$) the excited state molecule decays back to the ground state through fluorescence (channel 1) with a quantum yield[7] of ~0.2, the remaining population undergoes non radiative redistribution that is slow and attributed to intersystem crossing (ISC) (channel 2)[8-12]. The states just below the channel 3 region exhibit long lifetimes, for example the states 6^1, $6^1 1^1$ and $6^1 1^2$ leading up to an excess energy of 2367 cm^{-1} have a 108 ns lifetime[13]. This mechanism dominates up to ~3000 cm^{-1} of excess energy above the zeroth order first excited state region. At this point the fluorescence diminishes and significant line broadening occurs indicating an ultrafast non radiative process. This process comes about over a short energy range of 400 cm^{-1} which marks the onset of a new decay channel. The new decay channel has been termed "channel 3" since the mechanisms responsible for channel 1 and 2 are too slow to account for this ultrafast event where the linewidth measurements from this work placed the rate constant at 1×10^{12} s^{-1}.

The figure below summarises the situation in the first excited state of benzene. The observations can be all represented in terms of k_{nr}, the non radiative first order rate constant. The x axis of the figure indicates the energy above the S_1 origin expressed in wavenumbers (cm^{-1}). At the bottom of the figure the fluorescence spectra, measured as the log of the non radiative first order rate constant, k_{nr}, is shown as a function of energy above the S_1 origin in wavenumbers. Up to just below 3000 cm-1 above the S1 origin the log k_{nr} = 7.5, and above this energy the log of the non radiative first order rate constant begins to abruptly rise. The increase in the log k_{nr} value occurs due to the reduction in fluorescence. The top of the figure shows the linewidths $\Delta\nu$ (cm^{-1}) of the fluorescence peaks as a function of energy above the S_1 origin. Just above ~3000 cm-1 the linewidths can be seen to abruptly increase. The area around 3000 cm -1 where the fluorescence

diminishes and the remaining fluorescence peaks broaden indicates a change in channel from that of fluorescence to an ultrafast non radiative process (channel 3).

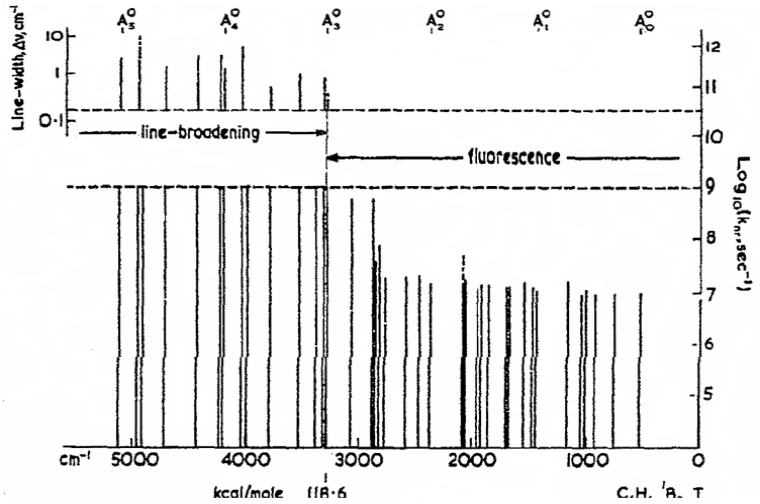

Figure 4: Summary of experimental data on rates of non-radiative decay in 260 nm system in benzene. Abscissa: energy cm^{-1} above zero-point of the $\tilde{A}\ ^1B_{2u}$ state, and k_{cal}/mole above the ground state of benzene. Ordinates: non-radiative rate constant k_{nr} on a logarithmic scale, and the equivalent spectroscopic linewidths. Taken from reference [3].

The difference in fluorescence above and below channel 3 can also be seen clearly in the Doppler free fluorescence spectra shown in figure 5. Riedle *et al.*, in 1983, compared the states $14_0^1 1_0^2$ and $14_0^1 1_0^1$, with the former being below channel 3 and the latter above[2]. They found that in the $14_0^1 1_0^2$ spectra only the K = 0 lines remain in the spectrum while all others become diffuse (i.e. K≠0). This brought about the conclusion that Coriolis coupling, the coupling of vibrational states due to rotation around a *z*-axis or *x*,*y* axes of the molecule, was causing the line broadening. This mechanism, a form of IVR, does not however explain the disappearance of fluorescence which would require a subsequent non radiative process after Coriolis coupling. It was thought that Coriolis coupling[2] redistributed vibrational modes into those known to be necessary for a internal conversion to the ground state namely out of plane modes, ν_{16} and ν_4 .[2]

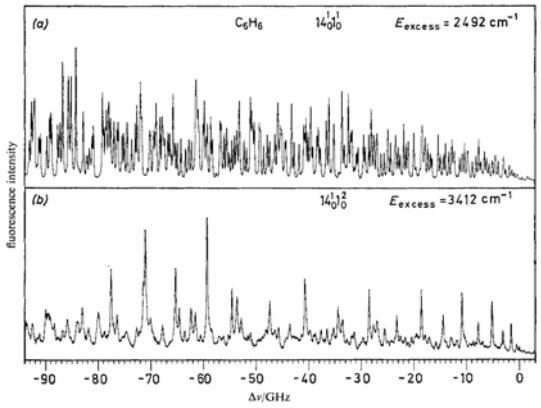

Figure 5: Doppler-free two-photon fluorescence excitation spectra of benzene. (a) part of the Q branch of the $14^1_0 1^1_0$: band at an excess energy of 2492 cm-'; (b) corresponding part of the $14^1_0 1^2_0$: band at 3412 cm^{-1}. [2]

Hellman and Marcus in 1993 modelled the observation of the rotationally selective line broadening with a combination of Coriolis and anharmonic coupling to vibrational background states within S_1. Around the same time it was proposed by Sobolewski *et al*. [14, 15], using CASSCF and MRCI techniques, that the energy barrier from the Franck Condon region to that of a prefulvenoid structure has the same absolute energy value as that of the "channel 3" threshold. From the prefulvenoid structure isomerisation could continue with the excited state population reaching the ground state through a conical intersection in the region and eventually resting in the ground state minimum of a structural isomer of benzene. This idea was further studied by Robb and co workers[13].

Investigations into the nature of the fast decay rate mechanism have up to now been postulated theoretically as an internal conversion (IC) through a S_0/S_1 conical intersection with a prefulvene like structure[5, 14]. Although not experimentally verified, it fits the long held understanding as introduced by Jortner[16] that IC is the only ultrafast non radiative intramolecular process available for molecules with low spin-orbit coupling such as benzene. ISC in cases of organic molecules in the gas phase remains a relatively slow process with timescales between picoseconds and nanoseconds. A variety of other explanations have been competently rebuked through the evidence obtained over the various studies conducted on benzene. These include notably isomerisation,

predissociation and intramolecular vibrational redistribution (IVR), all which could occur on a femtosecond (fs) timescale through movement over the potential energy surface.

It was first seen by Rice *et al.*[17] (1971), and later investigated again by Johnson[8, 9] (1983) that differences in decay dynamics in benzene occur depending on which modes are excited, with lifetimes ranging between 60 to 120 ns. This was later studied by Smith *et al.*[18] (1995) who concluded that there is a difference in dynamic behaviour between the $7^1 1^n$ and $6^1 1^n$ series both which are e_{2g} vibrations. Smith *et al.* [18] also confirmed this using picosecond photoionisation and photoelectron spectroscopy measurements of the electronic state lifetimes made by Sumitani[19-21] who used picosecond fluorescence techniques (10 ps pulse duration), and lifetimes inferred by quantum yield measurements. Although limited to picosecond resolution they were able to confirm the relationship that generally as vibrational energy is increased so is the electronic non radiative decay rate. Technological restraints occluded the true nature of many of the decay dynamics, whereby decays were often seen to be exponential with a few exceptions of biexponential decay[2] which was then attributed to excitation of a hot molecule and so causing IVR rather than an indication of the actual photochemistry. With the access to femtosecond time scales, in 2000, Neusser and coworkers[13] conducted the first ultrafast investigation of S_1 benzene using two photon time resolved photoelectron spectroscopy. They found that bi-exponential decays on the first four states in channel 3, $6^1 3^1$,7^1 ,$6^1 11^4$ and $7^1 1^1$ with the fastest of the decay constants found to be <300 fs.

In the most recent theoretical work, Zilberg[22] has found that the conical intersection responsible for decay to the ground state, has a spin orbit coupling to the triplet state higher than previously calculated. Investigations conducted previously[15] calculated the closest triplet state to the Franck Condon geometry and was found to be ${}^3B_{1u}$. The spin orbit couplings between this triplet state and S_1 were found to be 0.3-0.6 cm^{-1} implying little or no intersystem crossing. Zilberg instead searched for the closest triplet state from the S_1/S_0 conical intersection geometry which is C_s symmetry. He found the triplet state ,${}^3B_{2u}$ to be degenerate with the S_1 state and calculated a spin orbit coupling matrix element of 6.23 cm^{-1}. The rate of intersystem crossing is proportional to the square of the spin

orbit coupling matrix element this implies the rate of intersystem crossing could be up to 100 times faster than previously suspected. In this investigation of intersystem crossing at S_1/S_0 conical intersections he found a range of molecules exhibiting similar general behaviour[22].

3.2 Our investigation into the channel 3 mechanism using TRPES

In this section our experiments employing femtosecond time resolved photoelectron spectroscopy (TRPES) to unravel the photophysics at the onset of "channel 3" will be explained. Time-resolved photoelectron spectra were recorded using a photoelectron imaging apparatus that was described in the experimental chapter (section 2.1). The total integrated photoelectron signal provides a measure of the ionization probability as a function of time, and the photoelectron spectrum provides a map of time-dependent overlap integrals between the excited state and the accessible cation states, revealing detailed information about the evolution of the electronic and vibrational character of the wave packet on the excited state (section 2.1). A femtosecond pump pulse at 243 nm prepares benzene in the excited S_1 ($^1B_{2u}$) state with 3,070 cm^{-1} of excess vibrational energy. The subsequent evolution of the resulting wave packet is monitored by projecting its complete wave function onto all accessible cation states using a delayed femtosecond probe pulse (254 nm and 235 nm) to afford a two colour 1+1' photon ionisation scenario.

3.2.1 Energy level scheme

The energy level scheme relevant to the experiment is shown in figure 6. The zero-point energy levels of the singlet and triplet electronic states of neutral benzene and its cation are well known from experimental data[23] and the energy of the fulvene and prefulvene ions are calculated at the CASPT2 (perturbation theory corrected complete active space) level [24].

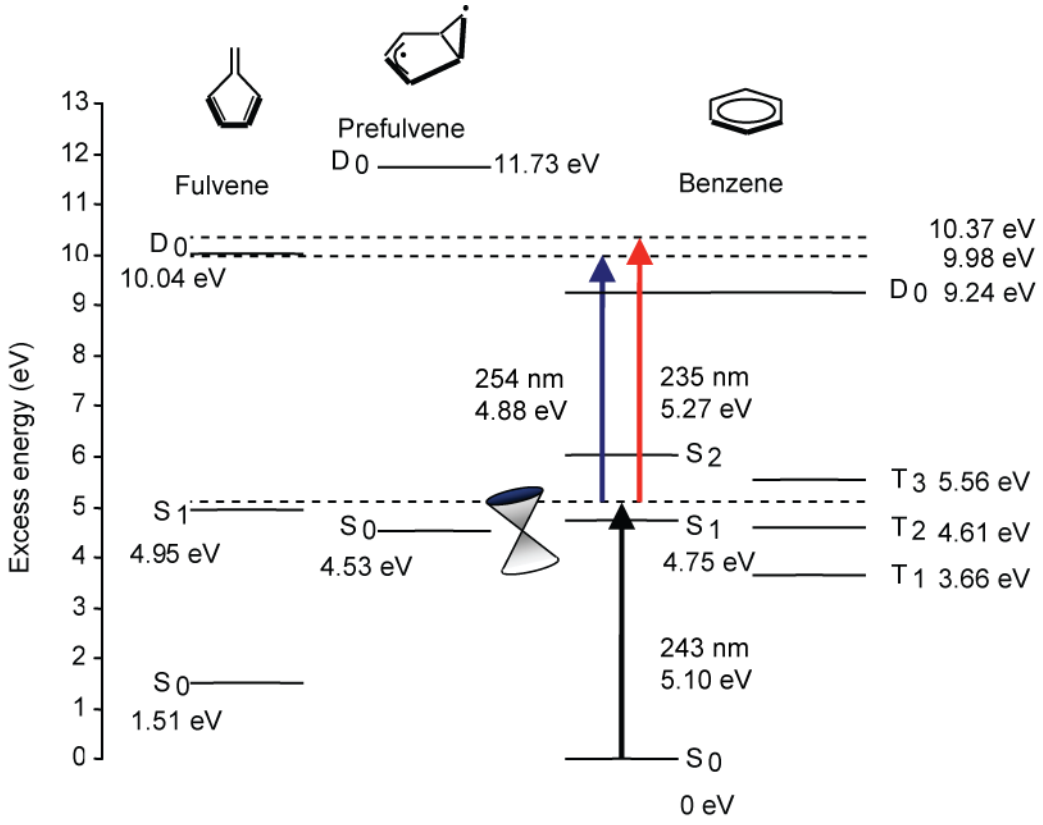

Figure 6: Energy level diagram depicting the electronic state energies of benzene and some energetically accessible features on the potential energy surface. Energies are relative to the zero point energy of benzene. A 243 nm pump pulse creates a wave packet on the first excited state of benzene in the Franck Condon region. A number of mechanisms to dissipate the absorbed energy are available to the wave packet these could be movement of the wave packet: through a conical intersection to the ground state which would involve adoption of a prefulvene like structure, to another isomeric form of benzene the closest being fulvene, through a singlet triplet surface crossing and then decay through phosphorescence.

The 243 nm pump pulse excites the ground state population to the first excited state onto a region where a good Franck Condon overlap exists with the ground state. Energetically, from this position the wave packet can access any area of the potential energy surface (PES) indicated by the dotted line. Although there are a variety of options available to the excited state wave packet some will be preferred depending on how facile the path to be taken is. The probability of where the wave packet goes and hence which mechanism is undertaken is determined by the topology of the PES and the trajectory of the wave packet initiated by the pump pulse. This is in turn determined partly by which vibrational modes are excited by the pump pulse and also by which hot bands may already be excited. Although the energies of the critical points are calculated theoretically and obtained experimentally (high resolution spectroscopy) they give little indication of how

they are related to each other. It is the topology of the PES between the critical points which is of most interest to us and which least is known about. This is because the path that the wave packet can take over the PES is determined by its topology and therefore determines the ultimate outcome of the photochemical or photophysical processes. The PES topology in this context refers to not only to the convolution of vibrational modes and so a change in structure but also the non-adiabatic regions responsible for surface crossing such as IC and ISC. From the Franck Condon region on S_1 the excited state wave packet can undertake a number of non radiative process; isomerisation to fulvene, IVR, IC to the ground state or ISC to the triplet state. Our aim is to understand which mechanism is responsible for the dissipation of the absorbed energy in the isolated molecule which undertakes an ultrafast non radiative decay process

3.2.2 Pulse intensity investigation

A 1+1 photon scheme (243 nm pump and 235 nm and 254 nm probe pulses) was adopted to conduct this experiment and these boundaries are essential to the correct conclusion being drawn. Importantly, the pump and probe intensities were kept well below 10^{11} W cm^{-2} to avoid multiphoton ionisation. The observed photoelectron count, $I \propto F^n$, where F is the laser fluence and n is the number of non-resonant photons involved in the ionisation process. In our experiments $n \approx 1$ as shown in figure 7. It should be noted that great care was taken to ensure intensity was kept to approximately the same value throughout all measurements.

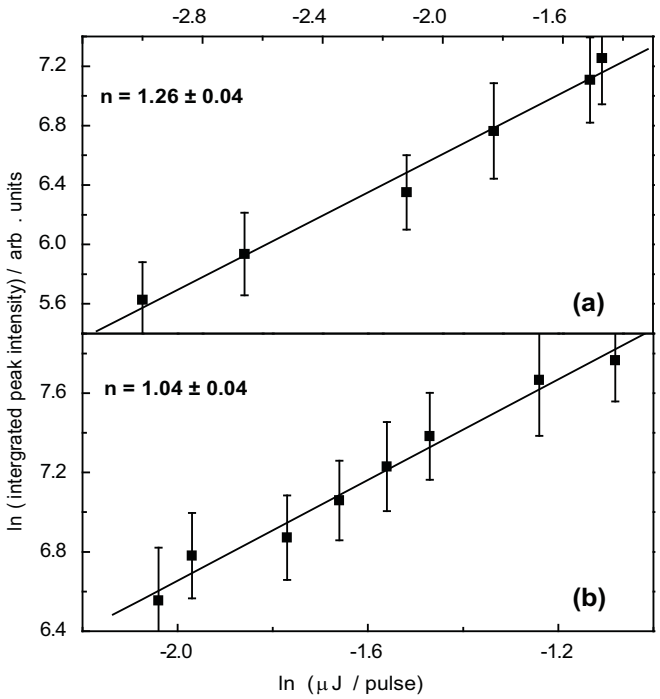

Figure 7: Intensity dependence of the photoelectron count rate. A pump of 243 nm and probes of 235 nm (a) and 254 nm (b) are investigated. Both curves show a gradient of approximately one and are measured at intensities well above those used in the imaging experiments as the power meters available in the lab are unreliable at such low pulse energies.

3.2.3 Time resolved total integrated photoelectron spectra

After absorption of a photon the excited state wave packet formed in the Franck Condon region will begin to move over the potential energy surface marking the start of its molecular dynamics. The wave packet will change energy as a function of time which can be observed by the probe pulse through ionisation and followed in a decay scan. A decay scan involves increasing the time delay between the pump and probe pulses continuously whilst measuring the photoelectron count rate recorded by the photoelectron imaging set-up. The photoelectron count rate is not energy resolved but is the total integrated photoelectron signal for the energy range as set-up by the ion optics as described in section 2.19 and the pulse energy. The total integrated photoelectron signal was measured over a period of 2 ps for two probes of 254 nm and 235 nm. The pump pulse was kept at 243 nm throughout all experiments in this chapter. Figure 8 shows the decay plots for the 235 nm (red) and 254 nm (blue) probe pulses.

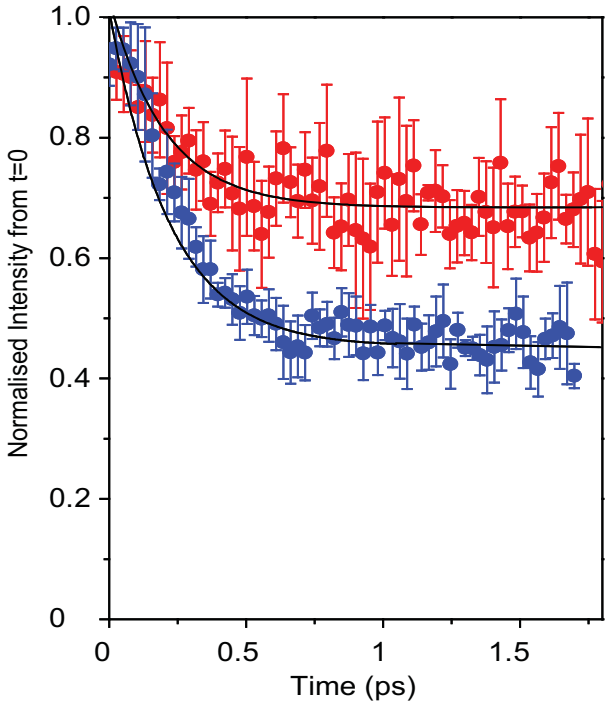

Figure 8: Variation of the normalised total integrated photoelectron signal from t=0 as a function of pump-probe delay for two different probe wavelengths. Experimental integrated photoelectron yield as a function of delay for probe wavelengths of 254 nm (lower curve/blue points) and 235 nm probe (upper curve/red points). The solid lines represent least squares fits to the observed data with a biexponential function. The recovered lifetimes are τ_1 = 220 ± 10 fs (blue) and 230 ± 10 fs (red) for the fast component and τ_2 = 11.5 ± 1.0 ps (254 nm probe) and 1.7 ± 0.3 ns (235 nm probe) for the slow component. The absolute value of the exponential tells us very little about the dynamics, only how quickly population leaves the observation window.

Every 10th point has been plotted in both graphs to show the points and error bars more clearly. At -0.5 ps, before the coherent $\tau = 0$ spike the count rate was collected for the pump only and probe only components for a period of 20 seconds each. The sums of the averaged signals were subtracted from the total count rate of the signal to give a count rate for the pump and probe only signal. The plots were normalised by dividing the number of counts by the peak value of the coherent $\tau = 0$ spike. Both decay curves were fitted to biexponential functions, as observed in previous femtosecond pump-probe ionisation measurements[13]. The error bars were calculated as twice the standard deviation from the fitted biexponential function.

The 254 nm and 235 nm probe pulses both exhibit a fast initial decay component of 220 ± 10 fs and 230 ± 10 fs respectively. It should be noted that this decay rate is within the cross correlation limit of the pump and probe pulses (175 ± 20 fs) from the bandwidth of 135 cm^{-1}, as shown in figure 14, chapter 2. The fast decay constant recorded is the shortest decay rate measured in this energy region of the spectrum. Decay rates on such a short timescale are commonly considered to be due to internal conversion. This had been considered the dominant ultrafast non radiative mechanism[5] causing "channel 3". The decay constants for the long decay component are 11 ± 1 ps for the 254 nm probe and 1.7 ± 0.3 ns for the 235 nm probe. The most interesting feature about these decay plots is their severe difference due to probe energy rather than pump energy. Both plots have the same pump pulse and so the difference is caused by what the probe can "see". With the increase in probe energy a 20 % increase in photoelectron count rate is obtained. It is expected to rise slightly due to the higher energy pulse giving better Franck-Condon overlaps with the ion. The 235 nm probe pulse (red) is only 0.4 eV greater in energy than that of the 254 nm probe pulse (blue) but is showing that only a possible 30 % of the population is leaving the probe viewing window at the ultrafast decay rate associated with internal conversion. The remaining 70% of the population must be due to something else. This implies only viewing the low energy 254 nm pulse decay scans could cause a misled conclusion about the length and scale of the initial decay; this could have affected the conclusions of recent work on benzene by Neusser[13].

The higher energy probe (red) is showing that a large portion of the excited state population is still able to be ionised by a probe of 5.27 eV. The low energy probe (blue) is limited in which area of the potential energy surface it can ionise. The area of the PES which the low energy probe is probing is evidently only around the initial geometry where the Franck Condon overlap is still good enough to reach the ionisation continuum. As the wave packet moves from the Franck Condon region to other areas of the potential energy surface, the 254 nm probe does not have enough energy to ionise the more vibrationally energetic wave packet. The high energy probe conversely does possess enough energy to ionise more of the wave packet evidently over a greater area of the PES. Therefore, the photoelectrons responsible for the 30 % difference in the

photoelectron intensity hold in them the information about the dynamics of the wave packet that remains on the excited state. To re-emphasise, incorporating the $\Delta v = 0$ propensity of benzene, the probe photon has only enough energy to cause ionisation from the excited state surface, since this experiment is a 1+1 photon process (section 3.2.3). Other possible schemes such as excitation to a Rydberg state to account for our signal would include a two photon process at some point which is not what we are seeing here. This consideration is discussed in more detail later in section 3.2.8.

The low energy probe is still ionising population on the excited state but not all of it. If there was no population on the excited state then the signal would be zero as all the population would not be able to be ionised on the ground excited state due to a poor Franck Condon overlap. Energetically, a two photon process at these wavelengths would be required to ionise the ground state population. This leads to the conclusion that around 70 % of the population is still on the excited state and the main mechanism is therefore not due to internal conversion to the ground state.

In summary, the higher energy probe (235 nm) is able to ionise 20% more of the excited state wave packet. Its relative photoelectron intensity of 0.7 compared with $\Delta t=0$ indicates at least 70% of the wave packet is still on the excited state ruling out internal conversion as the predominant decay process. With an increase in probe energy it may well be possible to view more of the excited state. The steep decay seen in the low energy probe (254 nm) indicates movement of the wave packet to another area of the PES. The initial ultrafast decay (20% of population) as viewed by the 235 nm probe cannot be seen by either probe and can be attributed to undergoing internal conversion as postulated previously[5].

3.2.4 Varying probe energy

A series of decay scans at a range of probe wavelengths were conducted to investigate the difference in the ionised excited state population seen in the decay plots, as shown in

figure 9 (a). All decay scans were kept at the pulse power that is responsible for 1+1 photon processes. The decays can be seen to be split into two groups, those above 250 nm (a)(i)-(v) which exhibit the decay profile as seen in the 235 nm probe and those below 250 nm (a)(vi)-(viii) which exhibit the same decay profile as that of the 254 nm probe. This cut-off region can be seen more clearly in figure 9 (b) where the amplitude of the slow component of the biexponentials fitted to the data (red line) have been plotted as a function of probe wavelength.

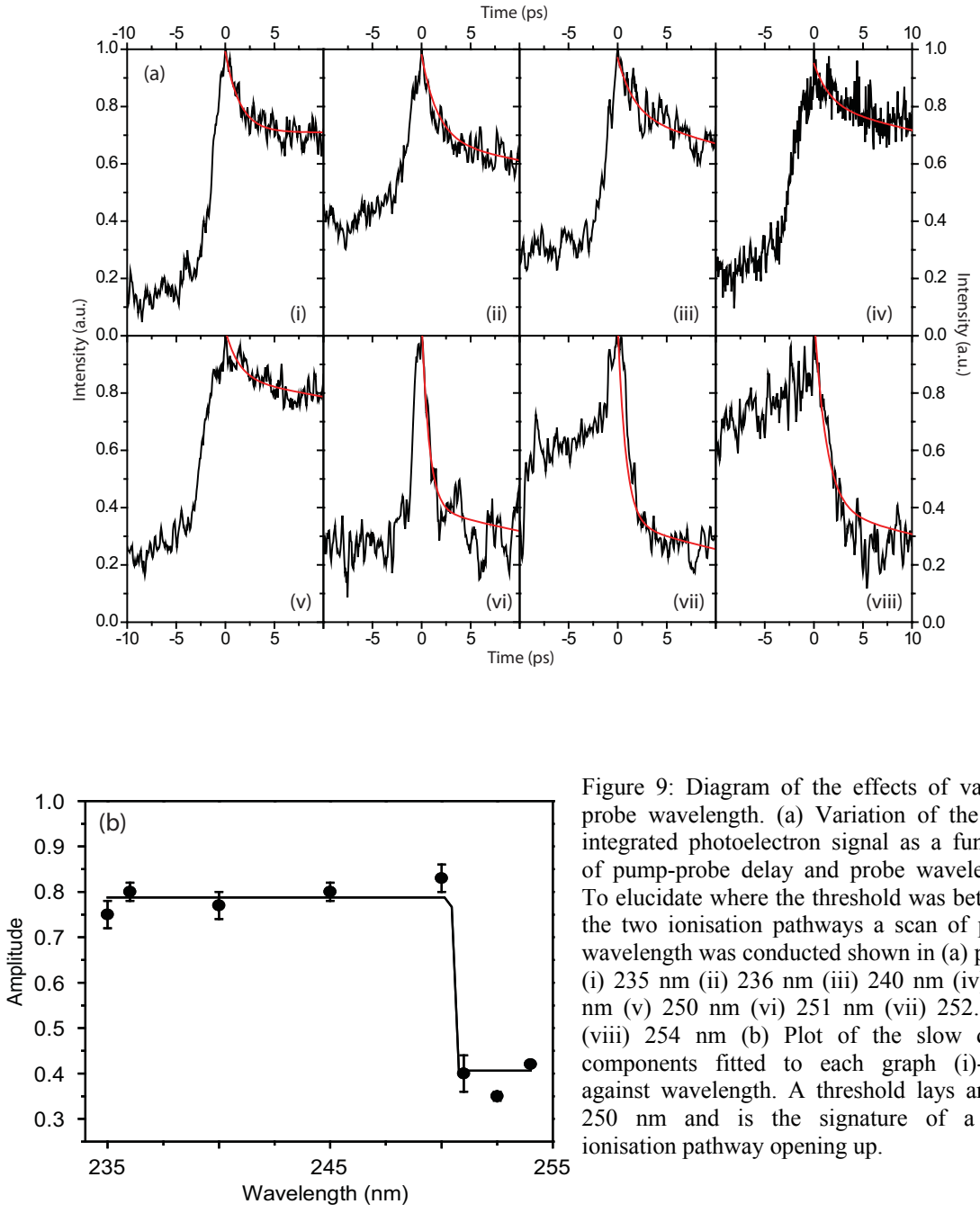

Figure 9: Diagram of the effects of varying probe wavelength. (a) Variation of the total integrated photoelectron signal as a function of pump-probe delay and probe wavelength. To elucidate where the threshold was between the two ionisation pathways a scan of probe wavelength was conducted shown in (a) panel: (i) 235 nm (ii) 236 nm (iii) 240 nm (iv) 245 nm (v) 250 nm (vi) 251 nm (vii) 252.5 nm (viii) 254 nm (b) Plot of the slow decay components fitted to each graph (i)-(viii) against wavelength. A threshold lays around 250 nm and is the signature of a new ionisation pathway opening up.

The distinct change in decay rate occurs at around 250 nm and is shown by the step function fitted to the data in figure 9(b). Such a distinct threshold is a signature of a new ionisation pathway opening up which suggests that there is a change in the electronic character along the adiabatic potential surface. This can be interpreted in two ways: Either the change is associated with an enhanced overlap of the wave packet on the excited adiabatic potential surface with an isomer of the benzene cation, or it is associated with an enhanced overlap with higher lying vibrational states of the benzene cation.

To re-iterate, from Franck-Condon arguments, to ionise any highly vibrationally excited levels of S_0 populated by internal conversion (IC) would require the energy of the probe to be of the order of 9 eV according to the $\Delta v=0$ propensity of benzene. In our experiments the probe energy is ~5 eV which is not high enough to ionise the products of IC in a single photon process, and the intensity is not high enough for two-photon ionisation of these levels. Thus, at this excitation energy, the fast decay observed is not associated predominantly with a direct transition through the S_1/S_0 conical intersection (CI)[5]. If IC did occur the decay plots would go to zero since the probe would not possess enough energy to reach the $\Delta v=0$ in the ion. As stated above, the decay of the total ion count in the first 600 fs observed using this higher probe energy can be attributed to population returning to the ground-state by ultrafast internal conversion. Having removed this contribution, changes in the photoelectron spectrum must be due to changes in the composition of the excited state wave packet.

In summary, what has been learnt from the decay scans and the step function is that the wave packet created on the excited state has three dynamical features. Firstly there is the initial ultrafast decay, which at most is 30% of the signal and that is happening at a rate commonly associated with internal conversion. Secondly, there is a 20 % portion of the excited state population that is residing on the potential energy surface which can be observed through ionisation by the 235 nm. Thirdly, there is the remainder of the excited state population that can be observed through ionisation by the 254 nm probe.

3.2.5 Oscillation in low energy probe signal

To investigate what the excited state population is doing the decay scan was further scrutinised. Since the initial fast decay has a plausible explanation of internal conversion (IC) its component was subtracted from the decay plot for both probes. As well as this the long decay was removed so any changes could be seen more clearly. This yielded no further insight for the 235 nm probe but did for the 254 nm probe. Figure 10 shows a plot where the biexponential decay has been removed from the decay scan. The long decay component was removed to see more clearly any features. The biexponential subtracted was that fitted to the decay plot as shown in figure 8.

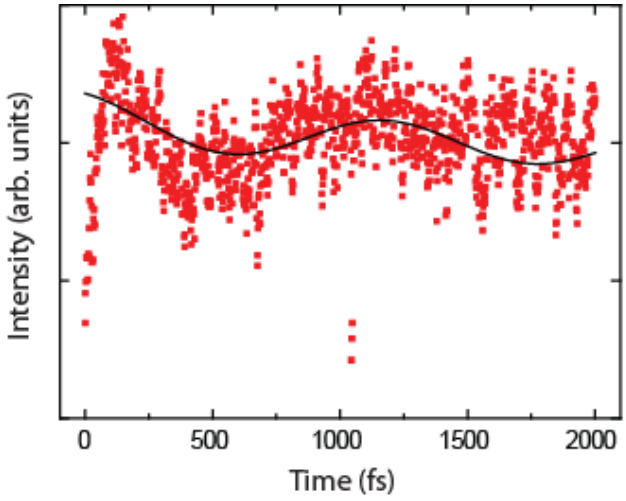

Figure 10: Total integrated photoelectron count rate as a function of pump probe delay for a 254 nm probe with the biexponential decay subtracted. An oscillation in count rate can be clearly seen oscillating with a period of 1.2 ps. This time scale is too long to be a signature of a pure vibration so must be accounted for be a movement of the wave packet over the potential energy surface. The biexponential as plotted as the solid line in figure 3.2.3 was subtracted from the data to yield this plot. The oscillation has been fitted with a sinusoid to obtain the period.

Figure 10 exhibits an oscillation over the scan range. The data has been fitted with a sinusoidal function which has a period of oscillation of 1.2 ± 0.1 ps. The data obtained in this decay scan shows the total integrated photoelectron count rate using the 254 nm probe. The period of 1.2 ps is too long to be associated with any type of vibrational mode (but not IVR) so must be accounted for by movement of the excited state wave packet over the potential energy surface. The data resembles a perfect sinusoid over the 2 ps range. The probe in this case is viewing an excited state wave packet that at $\tau = 0$ has a

good Franck Condon overlap with the continuum and 600 fs later has a weaker overlap. The wave packet appears to be bound and between two states. The probe has a reduced Franck Condon overlap with the outer turning point. The outer turning point must therefore require a different wavelength probe pulse to ionise it. The probe energy must need to be higher than 250 nm. In summary, a sinusoidal oscillation of 1.2 ps is observed in the total integrated photoelectron signal for the 254 nm probe which indicates movement of the excited state wave packet on a bound trajectory.

3.2.6 Energy differentiated time resolved photoelectron spectra

So far the true power of the photoelectron imaging apparatus has not been revealed. The most important aspect of the photoelectron imaging set-up is that it yields a differential signal with respect to energy. TRPES require hour long photoelectron spectra to be collected in order to gain adequate energy resolution and so limit the time over which data can be collected; these have been described in section 2.1.10. TRPES were collected for both the 235 nm and 254 nm probes. Due to the long collection times of each spectrum they were collected every 100 fs over a range of 2 ps to give sufficient time resolution. Each photoelectron spectrum recorded was normalised by the inversion algorithm. They subsequently had to be multiplied by the value of the bi exponential fitted of the decay scans (figure 8) for their respective times i.e. t=0 was multiplied by 1. Each spectrum had two 3 point rolling averages run through them to smooth out the noise. The data recorded for 254 nm is shown below:

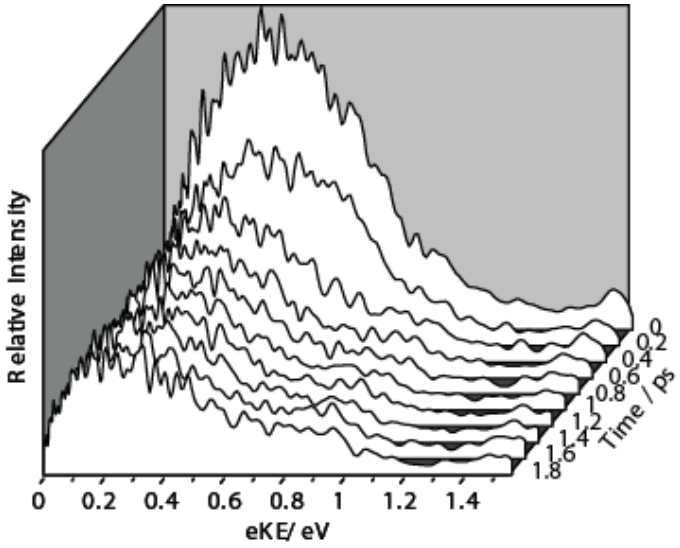

Figure 11: Energy and time resolved ionisation spectra for the 243 nm pump pulse and the 254 nm probe pulse. A spectrum was collected every 100 fs The biexponential decay can be clearly seen dominating this plot. There are no discernible features elucidating the decay mechanism visible in this plot.

Figure 11 shows the TRPES for every 200 fs to distinguish between spectra more easily. Apart from the biexponential decay there is nothing notable, that is to say there are no features appearing or disappearing as a function of time. The biexponential can be seen to be affecting the whole spectrum but no distinct features like that which has been seen in previous TRPES experiments for other systems[25] is seen here. This suggests a single cation electronic state is involved. The long period oscillation as seen superimposed on the 254 nm data could be evidence of isomerisation; however, an isomerisation would cause a change in internal energy distribution of the molecule leading to a change in the profile of the photoelectron energy distribution. The only isomer of the benzene cation that is accessible energetically by one-photon absorption from S_1 is the fulvene cation since the fulvene S_1 energy is 4.95 eV which is accessible by the pump pulse. CASPT2 calculations show that the ionisation limits of benzvalene, prefulvene, dewar benzene and prismane lie at 6.96 eV, 6.98 eV, 7.97 eV and 8.88 eV above benzene S_1 which are energetically inaccessible to the excited state wave packet. While ionisation to the fulvene cation cannot be ruled out, dynamics calculations[24] indicate that geometries where this will happen are not reached on the time-scale of the experiment.

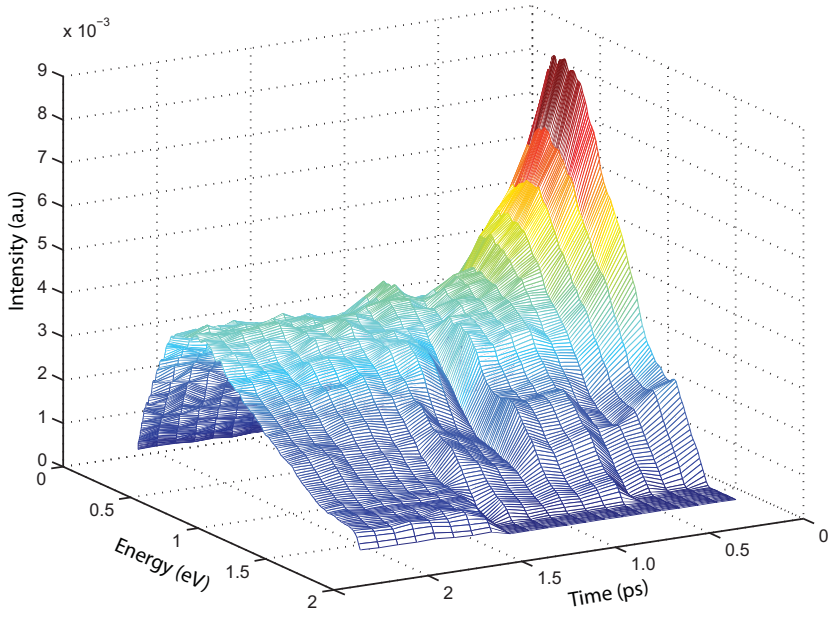

Figure 12: Plot of energy and time resolved ionisation spectra for all data collected using the 254 nm probe pulse. A spectrum was collected every 100 fs. As well as the rolling averages, each point on the energy scale was averaged over 20 points to provide a smoother energy profile in this plot. There are no discernible features elucidating the decay mechanism are visible in this plot.

Figure 12 shows all the spectra collected, those for each 100 fs over 2 ps for the 254 nm probe. As well as the rolling averages, each point on the energy scale was averaged over 20 points to provide a smoother energy profile in this plot.

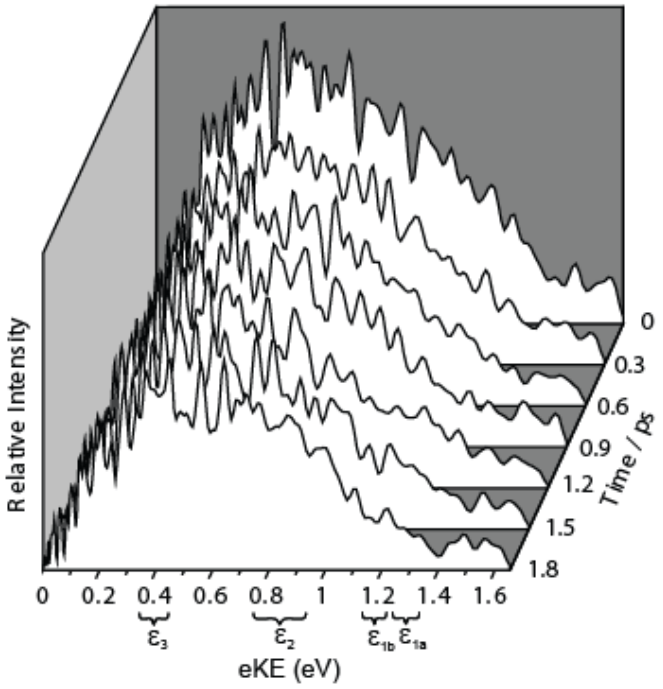

Figure 13: Energy and time resolved ionisation spectra for the 243 nm pump pulse and the 235 nm probe pulse. A spectra was collected every 100 fs but one has been plotted every 300 fs for clarity. The biexponential decay can be clearly seen dominating this plot. There are no discernible features indicating the decay mechanism visible in this plot.

The TRPES from the 235 nm probe is shown above in figure 13. The spectra have been processed in the same way as for the 254 nm data. Since this plot is noisier than the 254 nm probe spectra, the spectra have been plotted every 300 fs so their relationship can be more clearly seen. In the same way as for the 254 nm data no discernible features can be seen emerging or disappearing. This reinforces the notion that there is no significant movement of the wave packet to an area of the potential energy surface which has a Franck Condon overlap with a different cation state assuming the probe could access another cation state. In summary, the featureless forms of both TRPES suggest no isomerisation is evident and that the wave packet is ionising to the same cation state.

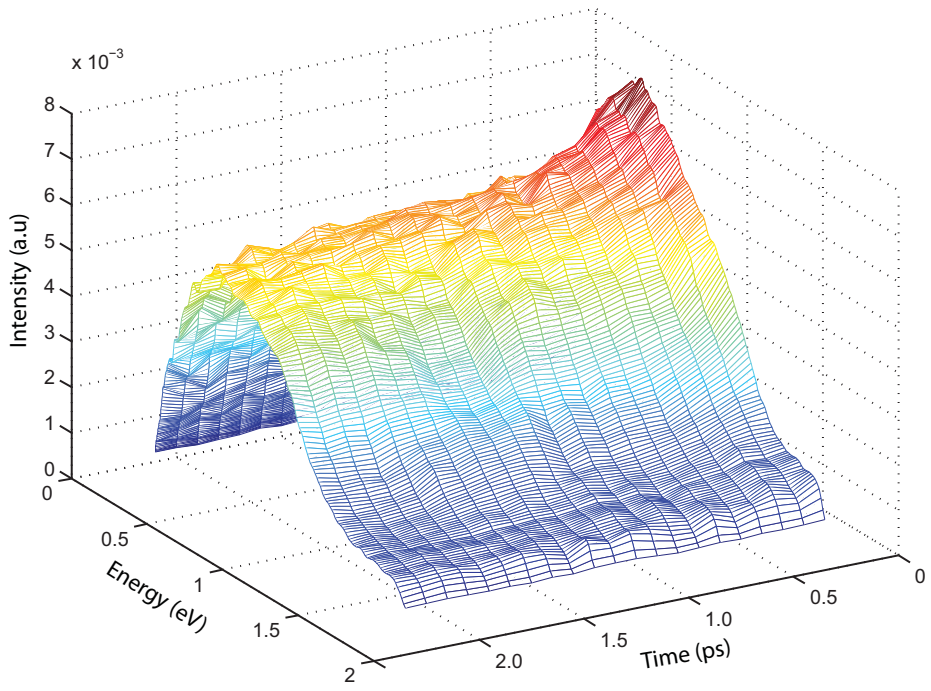

Figure 14: Plot of energy and time resolved ionisation spectra for all data collected using the 235 nm probe pulse. A spectrum was collected every 100 fs. As well as the rolling averages, each point on the energy scale was averaged over 20 points to provide a smoother energy profile in this plot. The biexponential decay can be clearly seen dominating this plot. There are no discernible features indicating the decay mechanism visible in this plot.

Figure 14 shows all the spectra collected, those for each 100 fs over 2 ps for the 235 nm probe. As well as the rolling averages, each point on the energy scale was averaged over 20 points to provide a smoother energy profile in this plot. The biexponential again can be seen clearly here. The analysis conducted that is described in the subsequent sections of this chapter uses every spectra but without the 20 point average.

3.2.7 Oscillation elements within the TRPES spectrum

The decay scan for the 254 nm data has already given an indication of excited state dynamics where a wave packet is oscillating on a bound state with a period of 1.2 ps. As discussed earlier, the increased number of photoelectrons obtained, relative to t=0, in the

235 nm TRPES data must contain within it information about the excited state dynamics. To search for photoelectrons exhibiting an oscillation of 1.2 ps a "box car" analysis was conducted on the 235 nm TRPES data. Firstly, the spectra were composed into a matrix then the biexponential decay fitted to the 235 nm data was removed. The matrix of electron kinetic energy as a function of time was scanned for any oscillations. For this analysis sinusoidal functions were fitted to plots of discrete energy ranges over time. Three energy regions were found to exhibit the most pronounced oscillatory structure. The energy ranges have been indicated in the figure 3.2.7, as ε_{1a} = 1.25 – 1.35 eV, ε_{1b} = 1.13 – 1.23 eV and ε_2 = 0.75 – 0.95 eV. The observed trends are clearly different from one another and can not be fitted by the exponential decay observed in the overall photoelectron count (Figure 8). Figure 15(a) shows plots of the $\varepsilon_{1a} + \varepsilon_{1b}$ and ε_2 as found by the oscillation analysis. The biexponential has been removed from (a) to give the plot in (b) where the oscillations can be seen with sinusoidal profiles and equal and opposite amplitudes.

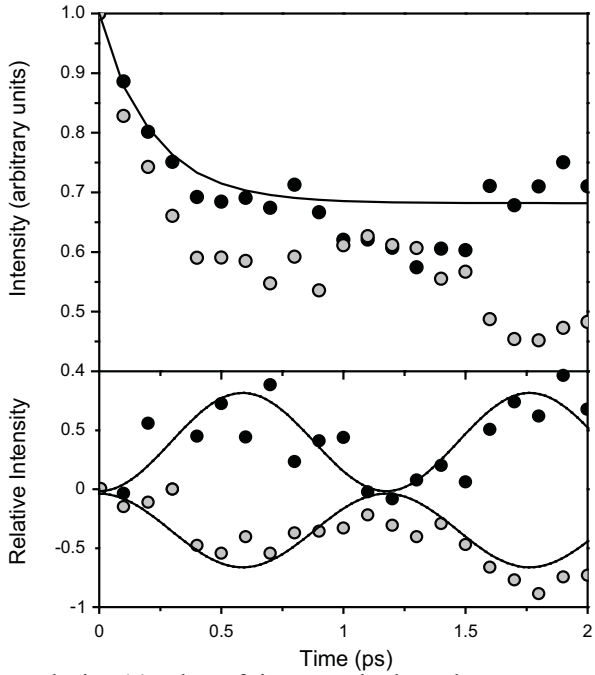

Figure 15: Oscillation analysis. (a) Plot of integrated photoelectron count over energy ranges with predominant oscillatory structure as a function of pump probe delay. The energy range ε_2 = 0.75-0.95 eV is shown as filled circles and the energy range ε_{1a} = 1.25-1.35 eV plus ε_{1b} = 1.13-1.23 eV are shown by empty circles. The biexponential decay fitted to the data is shown as the solid line. (b) Plot of integrated photoelectron count over energy ranges with predominant oscillatory structure as a function of pump probe delay with the biexponential decay subtracted. Both oscillations have the same but opposite amplitude. The oscillatory structure is indicative of a bound state. The in phase oscillatory components ε_{1a} and ε_{1b} are separated by 0.11 eV which is a signature of the ν_1 symmetric stretch in benzene.

Oscillations in the difference photoelectron counts are observed for photoelectron kinetic energies ε_{1a}, ε_{1b} and ε_2. The oscillations have a period $\tau_{osc} = 1.2 \pm 0.1$ ps, which is much longer than any fundamental vibration period of S_1 ($^1B_{2u}$) benzene. The three oscillations are clearly related to each other. Several interesting features come from figure 15: (1) the in phase oscillations are separated by 0.11 eV. (2) There are two oscillations that are in phase with each other but out of phase with the third oscillation. (3) The two in phase oscillations are seen in the high energy photoelectrons and the out of phase oscillation is seen in the low energy photoelectrons. (4) The in phase oscillations have the same oscillation profile as previously seen in the 254 nm data. (5) Finally, the sum of the amplitudes of the oscillations at ε_{1a} and ε_{1b} is equal to the amplitude of the out of phase oscillation at ε_2.

The separation of the two in phase oscillations by 0.11 eV corresponds very well with the ν_1 breathing mode of benzene. This is taken as a signature that the wave packet contains a component associated with the ν_1 breathing mode of benzene which is known to show a long vibrational progression upon ionisation. The in phase oscillations (ε_{1a} and ε_{1b}) show a high photoelectron count at $\tau = 0$ indicating they are observing the wave packet while it is in its ground state structure in the Franck Condon region on the excited state. At this geometry the higher energy photoelectrons of the out of phase component ε_2 are at a minimum. After 600 fs, the photoelectrons of the lower energy in phase energy range ($\varepsilon_{1a} + \varepsilon_{1b}$) have lowered in energy indicating the wave packet is in a higher energy potential which is harder to ionise and so termed a dark state. This is the outer turning point of the wave packets motion on the excited state surface. After a further 600 fs the bound wave packet moves back to a geometry similar to that of the ground state minimum and a full oscillation is complete. Since the magnitudes of the in phase components and the out of phase component are the same, the observed dynamics must account for the entire wave packet motion. The in phase oscillation which is attributed to the benzene ground state geometry is that which is observed in the decay scan of the 254 nm probe, figure 10. Energetically the 254 nm probe pulse is only able to ionise the wave packet in this region. These observations imply that we are ionising a bound wave packet

at two extremes of an oscillatory motion on the adiabatic potential energy surface. The bound oscillation can be summarised in a model two state system as shown below in figure 16:

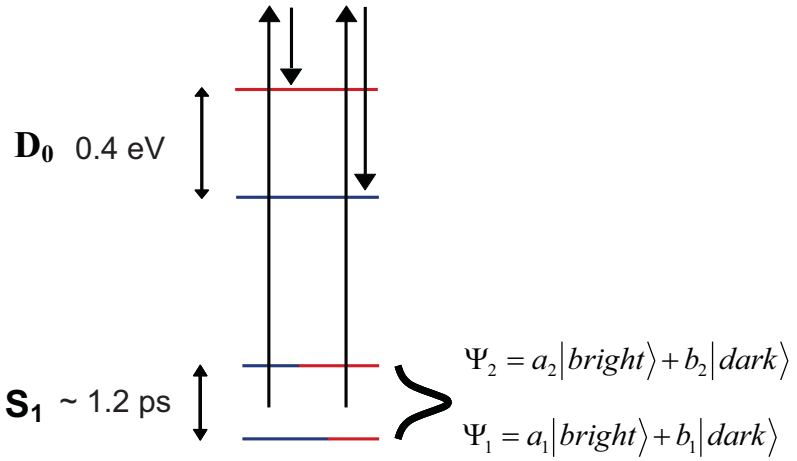

Figure 16: A two state system. A simple diagram to show a two state wave packet illustrates the basic picture so far of the oscillatory behaviour of the excited state process. The downwards pointing red arrow indicates the photoelectrons ejected by the low energy 254 nm probe pulse which can only view the bright state. The blue arrow indicates the photoelectrons ejected by the high energy probe which can view both bright and dark states of the wave packet. The oscillation period is 1.2 ps which manifests itself as a state separation of 0.4 eV.

The inner turning point in this case is a bright state which we are able to identify as the benzene ground state geometry and the outer turning point is the dark state which we will try to rationalise. We observe a 1.2 ps oscillation between components of the photoelectron spectrum separated by 5000 cm^{-1}.

One possible explanation considered for the observed signal is intramolecular vibrational energy redistribution (IVR). The effects of IVR on the photoelectron spectrum of toluene have been studied by Reid and coworkers[26]. In their experiment they observed 6 ps oscillations between components of a photoelectron spectrum separated by 500 cm^{-1} (arising from changes in Franck-Condon overlap between different rovibrational states of S_1 toluene and the ionisation continuum), which they attributed to a Fermi resonance between bright and dark vibrational states. Our observations are quite different. We observe a 1.2 ps oscillation between components of the photoelectron spectrum separated by 5000 cm^{-1}. The strong $\Delta\upsilon = 0$ propensity in the ionisation of benzene[12] suggests that this should not be interpreted in terms of a change in the Franck-Condon factors for different vibrational modes associated with the same electronic state, but by a change in

Franck-Condon factors for different vibrational modes associated with different electronic states.

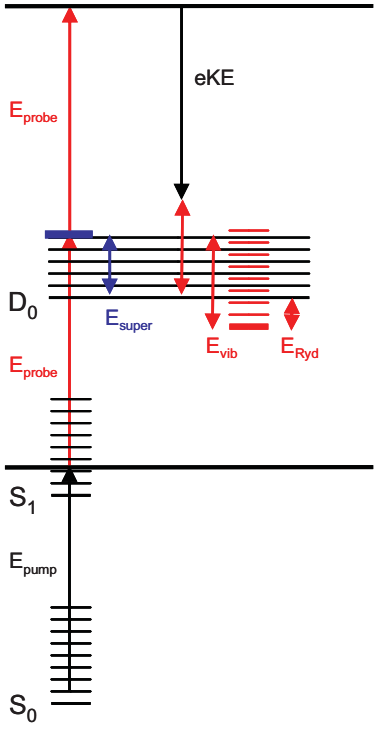

Figure 17: Energy level scheme illustrating formation of a saturated superexcited state (SES) in benzene. Recently a growing body of evidence in experiments of this kind, in aromatic molecules, suggests that it is easy to create doubly excited states that decay rapidly to Rydberg states which are vibrationally highly excited. When ionized the vibrational energy is conserved in the cation leading to a photoelectron spectrum that is independent of the probe wavelength. However, the SES would not be in the energy range of our detection system for this scenario.

The high energy probe used in our experiments is of sufficient energy to ionise S_1 by absorption of a single probe photon, E_{probe}. From our laser fluence study, it is clear that our ionization step either involves a single photon, or a saturated resonant two-photon ionization. The two-photon resonance could be a saturated superexcited state (SES) which then undergoes rapid internal conversion to vibrationally excited states of a Rydberg state converging to the lowest ionization threshold (D_0) – based on work reported by Weber and coworkers[27]. The figure above illustrates such a situation for benzene. It is clear that the electron kinetic energy (eKE) following two-photon ionization is $eKE = E_{probe} - R/v^2$, where $E_{Ryd} = R/v^2$ is the binding energy of the Rydberg state and ν is the effective principal quantum number. A 235 nm probe (5.28 eV) and eKE ~1 eV (corresponding to our observations) would require the Rydberg state to have an effective principal quantum number < 2. In benzene, this is not possible and would lead to a Rydberg orbit less than the diameter of the benzene ring. If we were accessing a Rydberg state with effective principal quantum number ≥ 3 (plausible and in line with Weber's observations) then the eKE would be ~4 eV. This is far larger than our

observation window (2 eV maximum). Consequently, the SES scenario is not a plausible explanation for the data.

3.2.8 Doorway state

Within the TRPES data another interesting feature is observed for photoelectron energies between 0.35-0.45 eV as labelled ε_3 in figure 15. Figure 18 (a) shows the box car integrated energy profile as a function of time with the biexponential fitted to the data. In this figure the count rate can be seen clearly rising above the biexponential fit. In figure 18 (b) the biexponential has been removed and there can be seen two levels to the intensity.

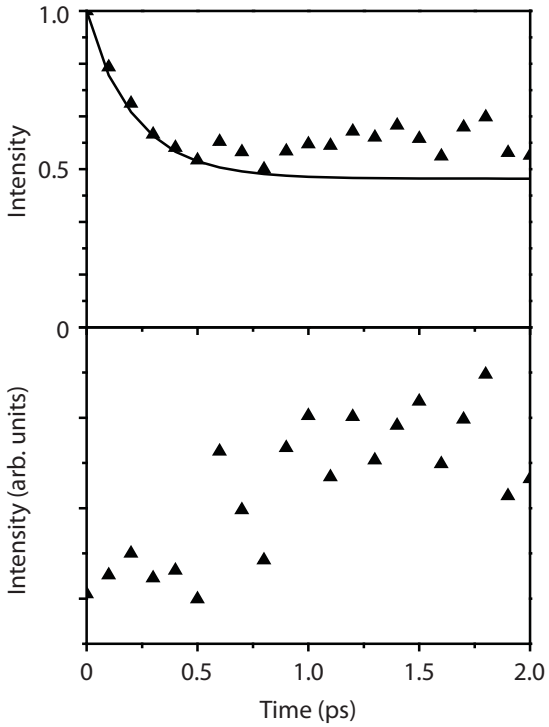

Figure 18: Plot of the energy range ε_3. (a) After 600 fs the excited state population can be seen to ride above the fitted exponential. (b) The biexponential decay has been removed to show the rise in excited state population more clearly.

The photoelectron count increases to a maximum at 600 fs (the time it takes for the bound wave packet to reach its outer turning point), suggesting that a portion of the excited state population is being transferred from the Franck-Condon region (monitored at ε_{1a} and ε_{1b})

to a dark state (monitored at ε_2) via a doorway state (monitored at ε_3). The fact that the population of ε_2 does not decrease as ε_3 rises, indicates that there is a strong coupling between ε_2 and ε_3 that transfers population to ε_3 immediately and that it is never detected in ε_2 .

3.2.9 Contour plot

All the features observed in the TRPES spectra can be better visualised in a contour plot of 235 nm data as shown in figure 19. The contour plot was made by subtracting the $\tau = 0$ normalised photoelectron spectrum from the rest of the normalised spectra. The spectra that compose the TRPES all have a similar profile as seen in figure 13.

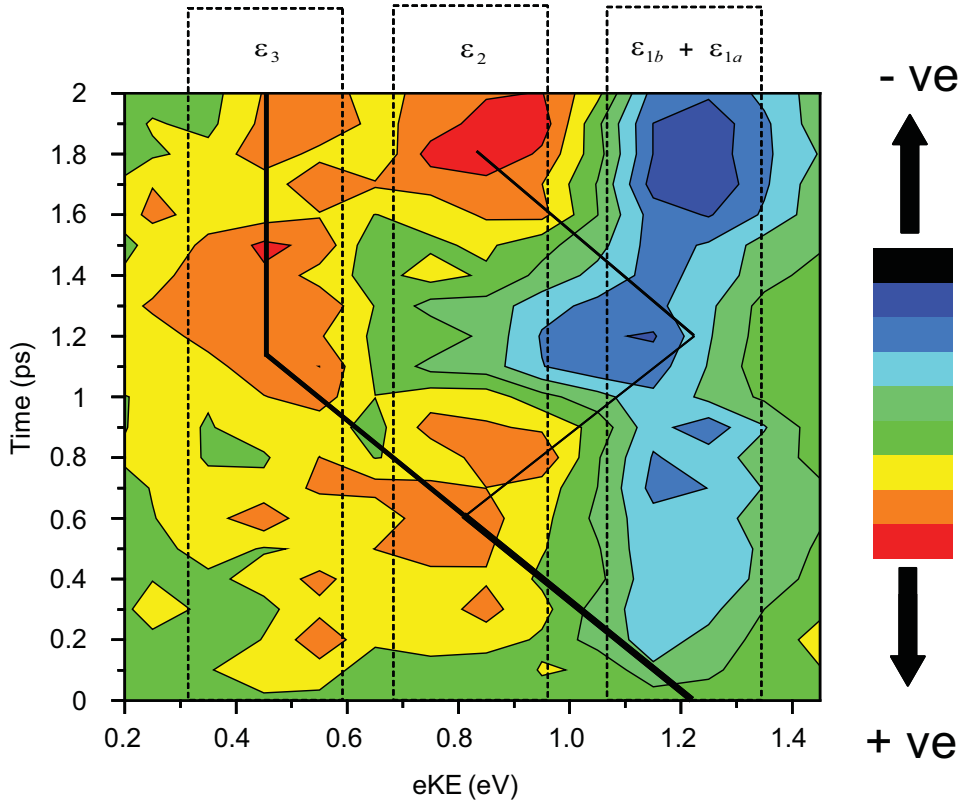

Figure 19: Contour plot of the 235 nm probe TRPES with the signal from that of the $\tau = 0$ spectrum subtracted to illustrate the difference in photoelectron signal. The three energy bands have been marked: the increase in signal after 600 fs, ε_2 the out of phase oscillation and ε_{1a} and ε_{1b} the in phase oscillation. A ε_3 black line has been plotted illustrating the movement of the wave packet over the potential energy surface. Cold colours indicate a lower than average signal and hot colours indicate a higher than average signal.

The contour plot has been plotted with hot colours indicting the higher number of photoelectron counts than the $\tau = 0$ energy profile and cold colours indicating lower number of photoelectron counts. Drawn on the contour plot are the three main bands of the 235 nm TRPES: The 600 fs rise ε_3 , the out of phase component ε_2 and the in phase component ε_{1a} and ε_{1b} (composed of two components). Superposed onto the contour plot are black lines to help guide the eye over the main features of the wave packets trajectory. Firstly, the wave packet decays on an ultrafast timescale attributed to internal conversion. This accounts for the first 600 fs. The wave packet is then split by an energy barrier into two components separated into those above the region corresponding to photoelectrons of 0.6 eV and those below. The component of the wave packet ε_3 with enough energy to overcome the barrier moves to a new area of the PES which no longer interacts with the remaining excited state population. The lower energy component of the wave packet is trapped on the excited state surface and oscillates back and forth between the bright state monitored by (ε_{1a} and ε_{1b}) and dark state monitored by (ε_2).

3.2.10 Intersystem crossing

From the analysis so far the routes that have been eliminated as possible mechanisms undertaken by the wave packet have been internal conversion to the ground state, isomerisation to fulvene and IVR. The remaining contending mechanism is ultrafast intersystem crossing. This, however, has been always regarded as occurring on too long timescale as stated by Jortner *et al*[16]. The observations can be explained in terms of ISC involving the S_1, T_1 and T_2 states of benzene – the energies of the measured photoelectrons correspond with those expected for ionisation of the S_1, T_1 and T_2 states based on simple Franck-Condon arguments and taking into account the excess vibrational energy in all of the states involved. The proposed dynamics is: that the excited state wave packet which starts in S_1 monitored by ε_{1a} and ε_{1b}, traverses after 600 fs to T_2 monitored by $\varepsilon_2$which acts as a doorway state, at the same time part of the excited state population couples to T_1 allowing for fast dispersion of the wave packet into its dense bath of states. The strong vibronic coupling between T_2 and T_1 facilitates rapid population transfer to

the dense bath of states which are energetically accessible in T_1, resulting in the step in the photoelectron counts observed at low photoelectron energies ε_3(Figure 18). The small population of states in T_2 which do not couple well to T_1, are then free to oscillate back to the S_1 state.

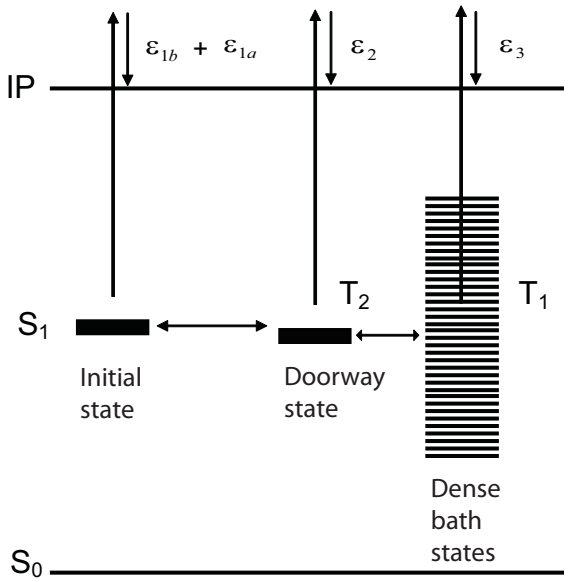

Figure 20: Illustration of the intersystem crossing mechanism. A wave packet is created by a 243 nm pump pulse which moves from S_1 (ε_{1a} and ε_{1b}) to a doorway state, T_2 (ε_2). The majority of the wave packet moves on from T_2 to T_1 (ε_3) through a strong coupling and is dissipated into the dense bath of states. The remainder of the wave packet does not overcome the energy barrier and oscillates back to S_1.

This "doorway" picture is common to many examples of intramolecular vibrational energy redistribution, albeit on a much longer timescale, where a sparse state facilitates the coupling between an initially populated bright state and its associated bath[28]. However, such rapid intersystem crossing challenges currently accepted models for ultrafast non-adiabatic processes in which ISC is assumed to be too slow to be important, unless certain conditions are fulfilled to increase the spin-orbit coupling (SOC) such as the presence of a heavy atom or nitro group[29-33].

In context, this picture of ISC fits into work conducted by Zilberg[22] as detailed in the last paragraph of the introduction. They found an increase in SOC in the prefulvene region where a conical intersection exists to the ground state. In terms of movement over the PES, the entire wave packet moves towards the prefulvene region of the PES. This

movement has been anticipated by Robb *et al*[5]. and others (Sobelewski)[14]. They found that easily excited symmetric modes, acceptor modes like the v_1 breathing mode feed into out of plane modes like v_4. The out of plane modes in turn are well known to move the excited state wave packet to the prefulvene area of the PES. From here theoreticians[5] (Robb) state the wave packet would decay through a conical intersection that occurs locally, down to the ground state. This agrees in part with our observations. Their models however did not represent the SOC between S_1 and T_1 effectively as argued by Zilberg. Although our picture differs from Zilberg in that we predict a doorway state T_2 to be involved it fits the theoretical prediction that the wave packet moves to the prefulvene region. The calculations Zilberg conducted may be misleading since the surface crossing region is hard to predict due to its reduced symmetry. This, for example, is caused by the non-Born Oppenheimer nature of this region of the PES. In the prefulvene region we see approximately 30% of the wave packet decay through the conical intersection to the ground state. The decay could take the population back to benzene or to other isomers such as fulvene. These isomers have been found in photolysis experiments but in no more than 1% yields[34]. The remaining population then moves as stated to T_2 through a CI to the triplet state where part flows to T_1 and is dissipated in the dense bath of states and part that does not and flows back to S_1 causing the observed oscillation. The assignments of these states have been aided by theoretical calculations which will be discussed in section 3.3.1.

3.2.11 260 nm probe

The contour plot in figure 19 illustrates the movement of the excited state population and helps in visualising the wave packets trajectory. The mechanism of an ultrafast intersystem crossing as being responsible for the long period oscillation in the signal can be further tested by varying the probe energy once again. The oscillation observed in the 254 nm probe (figure 10) can be seen in the contour plot (figure 19) to be between 0.7 - 1.0 eV of photoelectron kinetic energy. The photoelectrons ejected by the 254 nm probe have energies centred at 4.88 eV which means the observed oscillation is reduced by the overlap into channels other than that of the in phase oscillation. So to observe a more

pronounced oscillation with a greater amplitude the probe energy was reduced to 260 nm so the in phase oscillation was the predominant signal observed. Figure 21 shows the results from a decay scan conducted in the same fashion as in figure 3. The 260 nm data can be clearly seen to have an increase in oscillation amplitude with the electrons centred at 4.76 eV. This consolidates the energy ranges found in the TRPES data of the 235 nm probe.

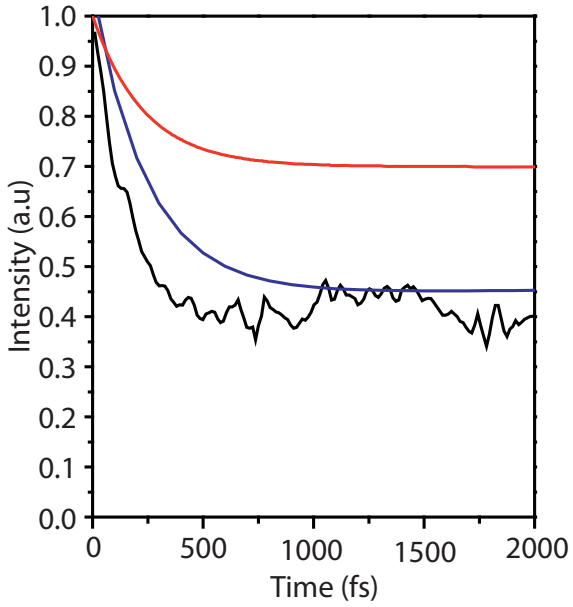

Figure 21: Variation of the total integrated photoelectron signal as a function of pump-probe delay. Experimental integrated photoelectron yield as a function of delay for a 260 nm probe (lower curve/black line). The biexponential fits, from figure 3.2.3, to the 235 nm (upper curve/red line) and 254 nm (middle curve/blue line) are shown for comparison. A large amplitude oscillation can be seen with the characteristic 1.2 ps period.

3.3 Supporting theory: MCTDH

The interpretation of the data has been supported by theoretical calculations conducted by our collaborators[36]. The coupled manifold of benzene singlet states S_0 (A_{1g}), S_1, (B_{2u}), S_2 (B_{1u}) and S_3 (E_{1u}) have been characterised previously by setting up a vibronic coupling model Hamiltonian to second order at the CASSCF level[24]. At this level of theory, however, the S_2 and S_3 states are poorly described and so this work has been repeated to greater accuracy to provide potential surfaces calculated at the CASPT2 level. The resulting model is able to reproduce quantitatively the lowest three bands of the

absorption spectrum of benzene. Important for the discussion of the initial dynamics is the cut along the "prefulvene" mode that takes benzene to the low lying S_1/S_0 conical intersection[5]. This is shown in figure 22. The (approximately 3000 cm^{-1} high) barrier on S_1 along this coordinate is clear. To the left of this barrier the S_1 state has $^1B_{2u}$ character and on the right of the barrier it has $^1E_{1u}$ character (and correlates diabatically to the S_3 state).

Quantum dynamics calculations were performed for 13 vibrational modes in the coupled four-state singlet manifold using the Heidelberg MCTDH package[32], including effects in the potential relevant for the first few hundred femtoseconds. In Wilson numbering the modes correspond to the breathing mode ν_1 , the e_{2g} modes ν_6, ν_9 which provide coupling between S_1 and S_3, the b_{2u} modes (including the kekulé mode) ν_{14}, ν_{15}, the boat and twists modes ν_3, ν_4 and the e_{2u} and e_{1u} in-plane stretches ν_{16} and ν_{19}. The initial wavepacket was a vertical excitation from the S_0 vibrational ground-state taking into account the strong Herzberg-Teller excitation in ν_6. The results show that after excitation to the S_1 state, almost 40% of the population crosses through the intersection to S_0 by 500 fs; it should be noted that this is approximately double the experimental value and extra pathways keeping density in the excited states must be present. ISC into the triplet states not included in these calculations could account for the discrepancy. Finally, we note that if the S_1 population is divided into its component $^1B_{2u}$ and $^1E_{1u}$ diabatic states, the latter attains a population of approximately 10%. Due to the highly distorted geometries in the $^1E_{1u}$ vibronic states, these will ionize at a higher energy than the $^1B_{2u}$ state.

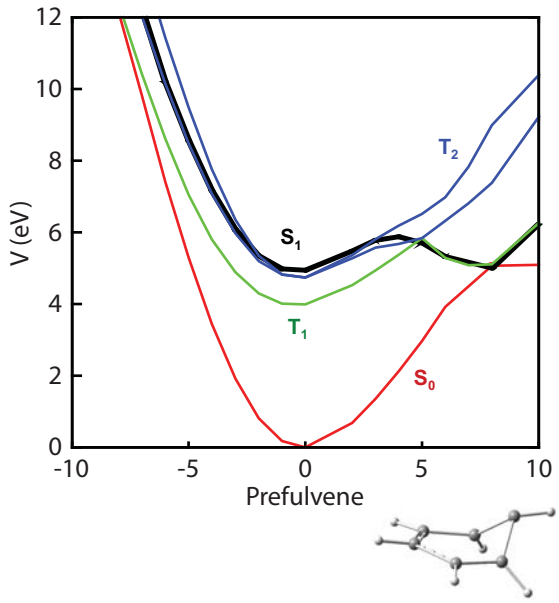

Figure 22: Cut through the potential energy surfaces of benzene along the "prefulvene" mode. A vector from the Franck-Condon point to the S_1 / S_0 conical intersection – calculated using the MOLPRO program at the CASPT2 level with a (6,6) CAS space and a Roos ANO basis set truncated to 6-31G* quality: S_1 (black), S_0 (red), T_1 (green) and T_2 (blue).

To examine the importance of ISC, the triplet states need to be included. This work is in progress, but the potential curves in figure 22 include the triplet states along the prefulvene mode. The T_2 ($^3E_{1u}$) and T_1 ($^3B_{1u}$) states lie just below S_1 at FC and the states cross. In fact they seem to meet at the barrier. At the FC point SOC is small between S_1 and T_1 (less than 1 cm^{-1}), and zero by symmetry between the $^1B_{2u}$ component of S_1 and T_2. However, recent calculations have found a value of 6.2 cm^{-1} for the SOC in the vicinity of the prefulvene conical intersection, and preliminary calculations indicate that the coupling is even higher at the barrier due to SOC between T_2 and the $^1E_{1u}$ component of S_1. By symmetry, the crossing point is also a singlet-triplet conical intersection, which is a more efficient pathway for population transfer than would be expected from this weak coupling. Thus the wave packet motion along the prefulvene mode will provide a route into T_2 and the near-degeneracy of these states explains the observed beating. The T_2 and T_1 states are then strongly coupled by pseudo-Jahn-Teller coupling involving modes with e_{2g} symmetry, providing a fast pathway between them, and resulting in the step-wise transfer observed to these low-energy vibronic states.

3.4 Wave packet composition and density of states

A wave packet composition analysis has been conducted as shown in figure 24. The fluorescence absorption spectrum has been shown in its entirety in figure 24 (a) taken from reference 6. The pump pulse has been superimposed onto the spectrum and represented by a pink Gaussian.

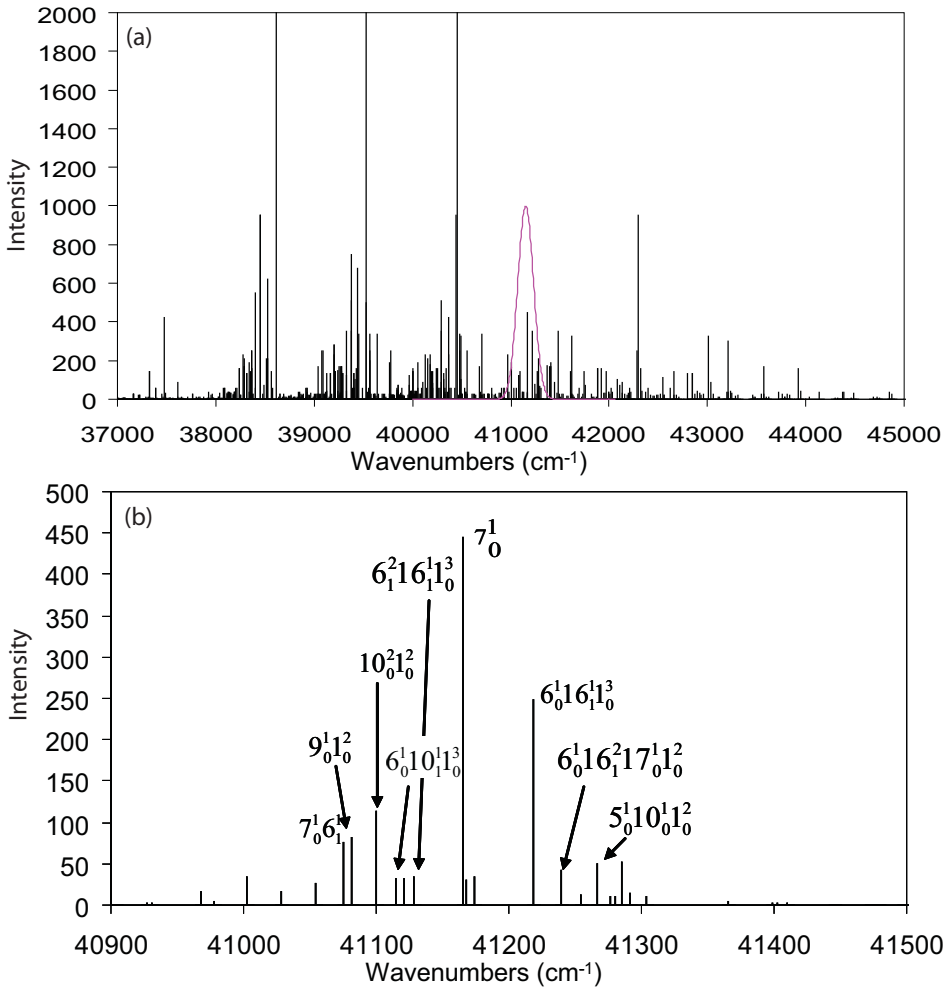

Figure 24: Wave packet mode analysis: (a) Spectrum of benzene (black) with pump pulse superimposed (pink). (b) Close-up of the vibrational states within the wave packet. The spectroscopic data have been taken from reference 6.

Figure 24 (b) shows a close up of the pump pulse and the major states within the bandwidth of the pulse. The composition of the excited state wave packet is thought to possess some hot bands from the ground state which is not represented in this analysis.

	excess energy eV	no. lines per cm-1
S1	0.35	4.25
T2	0.49	27
T1	1.44	94010

Table 2: Density of vibrational states in S_1, T_2 and T_1. The density of states has been calculated for the excess energy in S_1, T_2 and T_1 using the direct count method with vibrational frequencies from the S_1 state found in reference 37.

Table 2 shows the density of vibrational states calculated using the direct count method[37] for S^1, T^2 and T^1. The excess energy from the excitation from the ground state with the 243 nm (5.10 eV) pump pulse has been included in the table. The density of states can be seen to increase from S_1 to T_2 as the excess vibrational energy increases. The density of states dramatically increase in T_1 which matches the notion that T_1 acts as a bath state dissipating the wave packet vibrational motion into many different vibrational states.

3.5 Conclusion

In conclusion, we have observed ultrafast intersystem crossing in a hydrocarbon, which contradicts the currently accepted view that singlet-triplet coupling in hydrocarbons is weak and that ISC is assumed to take place on a much longer timescale than IC. The states involved are low lying singlet and triplet states that are close in energy, as is the case in many polyatomic molecules. Based on our calculations, the coupling strengths and density of states required for ultrafast ISC are far from extraordinary. Therefore, we expect ultrafast ISC to be widespread.

Finally, we note that although time-resolved photoelectron spectroscopy using ultrafast laser pulses has become a popular tool for monitoring ultrafast processes, care must be taken in the choice of probe photon energy since information can be lost if the probe laser cannot ionise the system across the entire reaction coordinate. Ideally, the photon energy of the probe should be able to project the complete excited state wave function onto the manifold of cation states with unit efficiency. We anticipate that the additional insight gained from observations with higher energy probe pulses that access the complete reaction coordinate, combined with accurate quantum dynamics simulations, will provide

more detailed insight into the photophysics that underpins our understanding of many important photochemical and photobiological processes.

3.5 References

1 T. A. Stephenson, P. L. Radloff and S. A. Rice, *Journal of Chemical Physics*, 1984, **81**, 1060-1072.
2 E. Riedle, H. J. Neusser and E. W. Schlag, *Faraday Discussions*, 1983, 387-394.
3 J. H. Callomon, J. E. Parkin and Lopezdel.R, *Chemical Physics Letters*, 1972, **13**, 125-&.
4 J. H. Callomon, T. M. Dunn and I. M. Mills, *Philosophical Transactions of the Royal Society of London Series a-Mathematical and Physical Sciences*, 1966, **259**, 499-&.
5 I. J. Palmer, I. N. Ragazos, F. Bernardi, M. Olivucci and M. A. Robb, *Journal of the American Chemical Society*, 1993, **115**, 673-682.
6 D. B. Moss and C. S. Parmenter, *Journal of Physical Chemistry*, 1986, **90**, 1011-1014.
7 W. A. Noyes, W. A. Mulac and D. A. Harter, *Journal of Chemical Physics*, 1966, **44**, 2100-&.
8 C. E. Otis, J. L. Knee and P. M. Johnson, *Journal of Chemical Physics*, 1983, **78**, 2091-2092.
9 C. E. Otis, J. L. Knee and P. M. Johnson, *Journal of Physical Chemistry*, 1983, **87**, 2232-2239.
10 M. A. Duncan, T. G. Dietz, M. G. Liverman and R. E. Smalley, *Journal of Physical Chemistry*, 1981, **85**, 7-9.
11 M. A. Duncan, T. G. Dietz and R. E. Smalley, *Journal of Chemical Physics*, 1981, **75**, 2118-2125.
12 S. R. Long, J. T. Meek and J. P. Reilly, *Journal of Chemical Physics*, 1983, **79**, 3206-3219.
13 M. Clara, T. Hellerer and H. J. Neusser, *Applied Physics B-Lasers and Optics*, 2000, **71**, 431-437.
14 W. Domcke, A. L. Sobolewski and C. Woywod, *Chemical Physics Letters*, 1993, **203**, 220-226.
15 A. L. Sobolewski, C. Woywod and W. Domcke, *Journal of Chemical Physics*, 1993, **98**, 5627-5641.
16 M. Bixon and J. Jortner, *Journal of Chemical Physics*, 1968, **48**, 715-&.
17 K. G. Spears and S. A. Rice, *Journal of Chemical Physics*, 1971, **55**, 5561-&.
18 J. M. Smith, X. Zhang and J. L. Knee, *Journal of Physical Chemistry*, 1995, **99**, 1768-1775.
19 M. Sumitani, D. Oconnor, Y. Takagi, N. Nakashima, K. Kamogawa, Y. Udagawa and K. Yoshihara, *Chemical Physics Letters*, 1983, **97**, 508-512.
20 M. Sumitani, D. V. Oconnor, Y. Takagi and K. Yoshihara, *Chemical Physics Letters*, 1984, **108**, 11-13.

21 M. Sumitani, D. V. Oconnor, Y. Takagi, N. Nakashima, K. Kamogawa, Y. Udagawa and K. Yoshihara, *Chemical Physics*, 1985, **93**, 359-371.
22 S. Cogan, Y. Haas and S. Zilberg, *Journal of Photochemistry and Photobiology a-Chemistry*, 2007, **190**, 200-206.
23 A. B. Burrill, J. T. Zhou and P. M. Johnson, *Journal of Physical Chemistry A*, 2003, **107**, 4601-4606.
24 L. Lorentzon, Malmqvist, P.-A, Fulscher, M. P. and Roos, B.-O., *Theoretica Chimica Acta* 1995, **91**, 91-108.
25 A. Stolow, J. G. Underwood, T. Schultz and J. P. Shaffer, *Abstracts of Papers of the American Chemical Society*, 2002, **223**, C46-C46.
26 C. J. Hammond, K. L. Reid and K. L. Ronayne, *Journal of Chemical Physics*, 2006, **124**.
27 N. Kuthirummal and P. M. Weber, *Journal of Molecular Structure*, 2006, **787**, 163-166.
28 Y. Yamada, N. Mikami and T. Ebata, *Journal Of Chemical Physics*, 2004, **121**, 11530-11534.
29 J. S. Zugazagoitia, C. X. Almora-Diaz and J. Peon, *Journal of Physical Chemistry A*, 2008, **112**, 358-365.
30 B. Moine, J. Rehault, S. Aloise, J. C. Micheau, C. Moustrou, A. Samat, O. Poizat and G. Buntinx, *Journal of Physical Chemistry A*, 2008, **112**, 4719-4726.
31 P. M. Hare, C. E. Crespo-Hernandez and B. Kohler, *Proceedings of the National Academy of Sciences of the United States of America*, 2007, **104**, 435-440.
32 O. F. Mohammed and E. Vauthey, *Journal of Physical Chemistry A*, 2008, **112**, 3823-3830.
33 J. J. Serrano-Perez, M. Merchan and L. Serrano-Andres, *Chemical Physics Letters*, 2007, **434**, 107-110.
34 L. T. Scott and M. Jones, *Chemical Reviews*, 1972, **72**, 181.
35 D. Bryce-Smith and H. C. Longuet-Higgins, Chemical communications, 1966, **17**, 593.
36 T. J. Penfold and G. A. Worth, 2009, *in press*.
37 T. Baer, W. L. Hase, *Unimolecular reaction dynamics*, 1996, **6**, 183

Chapter 4

Frequency doubling and Fourier domain shaping the output of a femtosecond optical parametric amplifier: Easy access to tuneable femtosecond pulse shapes in the deep ultraviolet

Tuneable, shaped, ultraviolet (UV) femtosecond laser pulses are produced by shaping and frequency doubling the output of a commercial optical parametric amplifier (OPA). A reflective mode, folded, pulse shaping assembly employing a spatial light modulator (SLM) has been designed and built to shape femtosecond pulses in the visible region of the spectrum. The shaped visible light pulses are frequency doubled to generate phase- and amplitude-shaped, ultrashort light pulses in the deep ultraviolet. This approach benefits from a simple experimental setup and the potential for tuning the central frequency of the shaped ultraviolet waveform. A number of pulse shapes have been synthesised and characterised using cross-correlation frequency resolved optical gating (XFROG). This pulse shaping method is robust and can be employed for coherent control experiments in the ultraviolet region of the spectrum where many organic molecules have strong absorption bands.

4.1 Introduction

Pulse shaping techniques in the frequency domain for femtosecond pulses have enabled huge advances in the field of molecular coherent control. Shaped pulses have proved to be an effective tool for exercising control over the branching ratios in dissociation reactions[1, 2]. Such control mechanisms have tended to rely on multiphoton excitations to access excited molecular states, together with simultaneous perturbations and re-arrangements of molecular bonds that occur *via* the Stark effect due to the intense electric field of the excitation laser. Weak field coherent control is an important complementary tool because under such conditions, insights into the nuclear dynamics on the unperturbed, field-free potential energy surfaces, during the process of a photochemical reaction, may be obtained. Many organic molecules require shorter wavelength photons in the ultraviolet region of the spectrum to access the excited electronic states in a single photon process. The possibility of steering excited state molecular dynamics of such species using tailored ultraviolet (UV) pulses is very exciting; however, at present there is a divergence between the capabilities of commercially available pulse shaping technology and the requirements of such weak field coherent control. The most common pulse shaping technologies are constrained to a wavelength range from the near infrared (IR) to the visible. With this in mind, we set out to design and build a simple setup to create shaped UV femtosecond pulses for the control of organic photochemistry.

The ability to shape directly in the UV is possible with micro-mechanical mirrors[3]; however, this technique is still under development and is currently limited to smooth and low-amplitude phase shapes. The two predominant methods of producing shaped pulses both use programmable mask technologies: acousto-optic mask (AOM) devices and liquid crystal modulators, both shape in the Fourier domain within a 4*f* zero-dispersion compressor set-up. Very recently, direct pulse shaping in the UV at 262 nm has been achieved using a fused-silica acousto-optic modulator (FS-AOM)[4]. Acousto-optic programmable dispersive filters (AOPDFs) are a more recent development of AOM technology, and operate directly on the beam, cutting out the difficulties of alignment but also losing the higher resolution possible within a 4*f* setup[5, 6].

Commercial spatial light modulators (SLMs) have very high resolution and may be employed to create highly complex pulse shapes. They do not usually operate effectively at UV wavelengths, however, Hazu and coworkers have recently developed a novel UV-transparent liquid crystal SLM[7]. In an attempt to manipulate the phase and amplitude of UV light using commercially available SLMs, non-linear techniques such as sum frequency generation (SFG)[8] and second harmonic generation (SHG)[9] have been used to shift a shaped waveform to a higher carrier frequency in the UV – so called indirect UV pulse shaping.

Indirect pulse shaping has been demonstrated experimentally by several groups[8-12] and studied theoretically by Wang *et al.*[13]. Most of these studies have focussed on UV shaped pulse generation by sum frequency mixing or type II second harmonic generation (SHG). In type II SHG and SFG, the polarisations of the two light beams are mutually perpendicular, and one of the beams may be shaped and the other unshaped (figure 1 (b)).

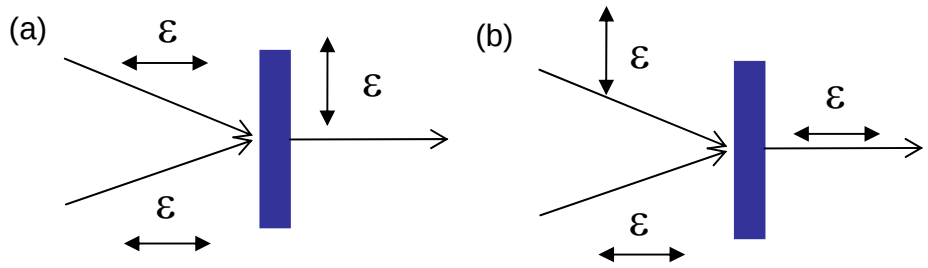

Figure 1: A diagram showing the type I SHG and type II SHG and SFG. The blue rectangle represents the second harmonic crystal, the two arrows pointing towards it represent the two photons incident on the crystal, with their respective polarisations illustrated. (a) Type I SHG where the incident polarisations are the same but perpendicular to the output. (b) Type II SHG or SFG where the incident polarisations are perpendicular to each other. The output polarisation is dependent on the crystal angle.

Gerber and co-workers produced shaped UV pulses at the third harmonic of the output of a Ti-sapphire laser by using sum-frequency generation of shaped 800 nm pulses with a temporally stretched 400 nm pulse[8]. The 400 nm pulse had to be stretched (chirped) to ensure complete temporal overlap with all parts of the shaped light. Schriever *et al.* reported a similar indirect UV pulse shaping capability using the output of a non-collinear optical parametric amplifier (NOPA) in a pulse shaper followed by SFG with a 775 nm beam to produce shaped light in the near UV at 344 nm, with some very short sub-pulse

structures (19 fs)[11]. Their method has the advantage of tuneability – the NOPA may be tuned so that pulses at a wide range of UV wavelengths may be generated. These SFG indirect shaping techniques have proved capable of producing highly structured pulses in the UV. The disadvantage of the method, and for indirect UV pulse shaping by type II SHG, is that it is complicated by the necessity of mixing in a temporally stretched pulse to cover the time window of the shaped pulse: the result is a shaped UV pulse with an inherent chirp for which some compensation must be made. Although many successful coherent control experiments have been achieved using non-linear mixing of the harmonics of the 800 nm Ti:Sapphire fundamental, there exists a need for a fully tuneable deep UV pulse shaping capability for quantum molecular dynamics and control.

Type I SHG, in which two photons of the same frequency and polarisation are converted into a single photon of double the frequency, offers the simplest experimental arrangement for indirect pulse shaping (figure 1(a)). A pulse may be shaped in the infrared or visible region of the spectrum and then frequency doubled, simply by placing a correctly cut doubling crystal in the beam path, to reach the wavelength of interest. To the best of our knowledge, only one implementation of this indirect shaping method has been reported in the literature: Hacker *et al.* were able to measure the spectra of shaped pulses at 400 nm that had been generated by SHG of a sinusoidal phase modulated 800 nm pulse[9]. The authors highlighted some key aspects of this conversion technique, namely that the preservation of the phase of the field in the SHG upconversion process is dependent on the type of function on the phase of the input electric field. They also speculated that the phase profile of a sinusoidal phase shape is not preserved in the up-conversion process but were unable to measure the phase of the upconverted light. Owing to the simplicity and versatility of the experimental setup, we chose to generate shaped ultrafast pulses in the deep UV using a standard SLM setup to shape the visible output of an OPA followed by type I SHG. In this chapter the effectiveness of a pulse shaping and type I SHG setup, as pioneered by Hacker *et al.*, by fully characterising the shaped UV pulse is demonstrated. We present both XFROG traces (spectrograms) of the upconverted pulses, and the analytic descriptions of the electric fields of the shaped UV laser pulses, which were obtained from electric field reconstructions.

4.1.1 Pulse shaping using a 4f zero dispersion compressor configuration

A 4*f* zero dispersion compressor configuration refers to an arrangement of optics that disperses the frequency components of a broad bandwidth femtosecond pulse out linearly in space without causing any change in the phase or amplitude profile of the original pulse[14]. Having the pulse drawn out in space enables access to the individual frequencies. The experimentalist is able to alter the frequency domain profile of the pulse in terms of phase and amplitude. This type of arrangement has a variety of applications in photonics such as within regenerative amplifiers, stretchers, compressors and fixed mask pulse shaping[15].

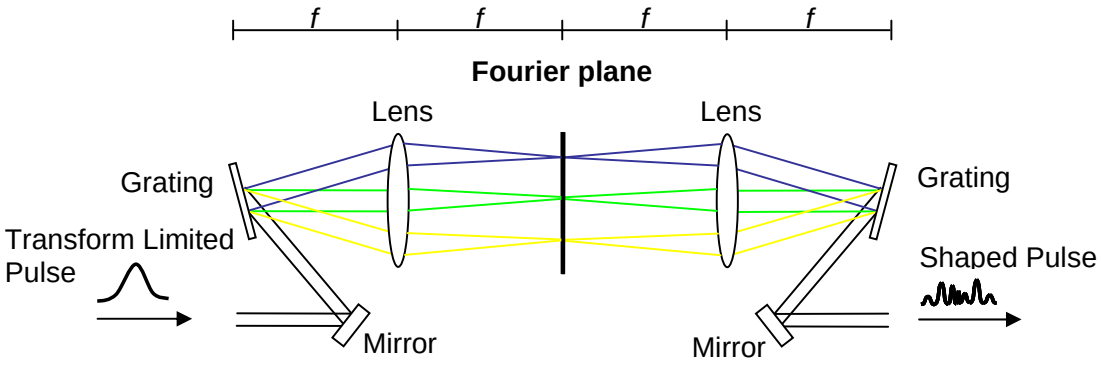

Figure 2: A schematic diagram of the 4*f* zero dispersion configuration for shaping coherent light. The incident transform limited pulse is dispersed by a grating into its constituent frequency components where the angle of dispersion is dependent on wavelength, this has been represented in the figure by fast colours (blue) being diffracted less than slow colours (yellow). A lens focuses the individual frequency components to their smallest beam waist in the Fourier plane so that the pulse is spread out linearly as a function of frequency. A modulation device is placed in the Fourier plane, modulating either or both amplitude and phase of the frequency components. The second lens focuses the beam on the grating which diffracts it back to its original shape with any modulation imparted due to the modulation device and not the 4*f* line.

Figure 2 shows one of the earliest geometries used[16]. The principles behind its use are that a broad bandwidth transform limited femtosecond pulse is directed onto a diffraction grating by a mirror, where the individual frequency components are diffracted out at different angles spreading the pulse out linearly as a function of wavelength. A lens at the point where the pulse has been spread out by the desired amount, *f*, collimates the pulse. The lens also focuses the individual frequency components to their smallest beam waist at the Fourier plane.

The line between the lenses where the individual frequency components are focused and overlap the least is called the Fourier plane. This is the most appropriate position for a modulation device to afford the highest resolution[14]. Once the pulse has been modulated it passes through the same procedure in reverse. The collimated beam is focused onto the diffraction grating by a second lens at a distance *f* from the Fourier plane back to its original beam diameter. The diffraction grating is again at a distance *f* from the lens which constitutes the final *f* of the 4*f* set-up. Zero dispersion of the pulse is achieved by keeping all distances equal to *f*. Compressors and stretchers work by making small adjustments to one of the focal lengths, *f*, to introduce a linear chirp which results in a change in the temporal profile.

4.1.2 Fourier domain pulse shaping and linear masking

If we assume the modulation device has no inherent dispersion, we can assume the input electric field $E_{in}(\omega)$ of the pulse is the same as that of the output pulse electric field $E_{out}(\omega)$, and the change introduced by the modulation device can be represented by a mask function, $M(\omega)$*:*

$$E_{out}(\omega) = M(\omega)E_{in}(\omega) \tag{4.1}$$

The aim of the pulse shaper is to achieve complex pulse shapes in both the time and the spectral domain. Many control experiments have at the centre of their control schemes a series of sub pulses in a pulse train scenario[17]. Unfortunately it is impossible to create electronics that can operate on this time scale. To overcome this problem the interference effects of coherent light in the frequency domain are used to modulate the pulse in the time domain. The frequency domain modulation is converted to time domain modulation *via* a Fourier transformation:

$$E_{out}(t) = M(t)E_{in}(t) \tag{4.2}$$

Where the electric field in the time domain of the input and output pulses are $E_{out}(t)$ and $E_{in}(t)$ respectively.

4.2 Pulse shaper design

4.2.1 Pulse shaper geometries

There are several geometries that can be used incorporating a dual array SLM[18] which will now be discussed. The SLM can be used in either a transmissive mode, with the pulse passing through the SLM once, or in a reflective mode where a mirror is placed directly behind the liquid crystal array to send the pulse back along the same path. The transmissive mode has the advantage of higher throughput energy but has the disadvantage of twice the number of optics that needs aligning. All geometries shown in figure 3 adhere to the 4*f* zero dispersion compressor set-up[19].

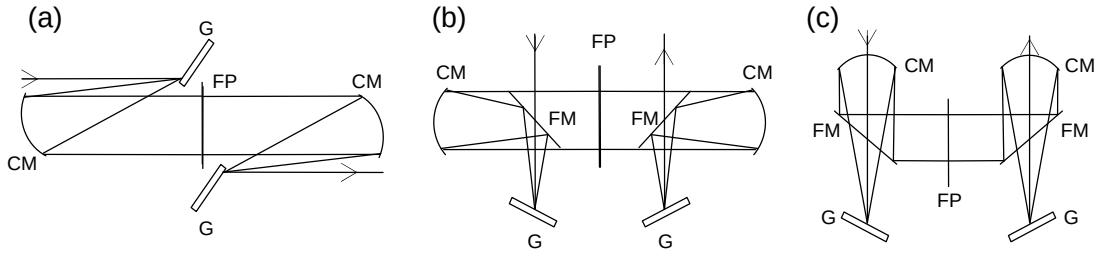

Figure 3: Pulse shaper designs. (a) Cylindrical mirrors are used instead of lenses. Termed the z configuration, this set-up has off axis errors from the mirrors. (b) Folding mirrors are used in this design to eliminate off axis errors. (c) Similar in principle to (b) but in a more compact formation. CM; cylindrical mirror, G; grating, FP; Fourier plane, FM; Folding mirror.

Figure 3 illustrates the classic geometry using a pair of lenses to collimate the beam. Chromatic aberrations are introduced by the lenses causing temporal and spatial reconstruction errors. While this set-up benefits from all the components being on an optical axis aiding alignment it has the disadvantage of only being suitable for shaping pulses of durations over 100 fs. Geometries in figure 3 (a) – (c) make use of cylindrical mirrors to overcome the error introduced by using lenses. In figure 3 (a), the cylindrical mirror reflects with an angle in the horizontal plane which causes optical aberrations. Although kept as small as possible this angle is unavoidable. To eliminate this severe

angle, the beam can be reflected from the cylindrical mirror in the vertical plane as in figure 3 (b) and (c). Both designs (b) and (c) make use of a folding mirror to reduce the overall size of the geometry and to steer the beam so that the optical components assemblies have enough room to be easily accessed.

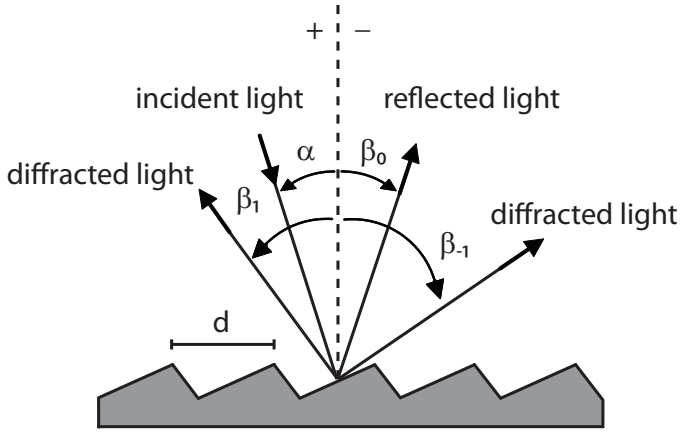

Figure 4: Diffraction by a plane grating. A beam of monochromatic light of wavelength l is incident on a grating and diffracted along several discrete paths. The triangular grooves come out of the page; the rays lie in the plane of the page. The sign convention for the angles α and β is shown by the + and - signs on either side of the grating normal.

The angle between the incident and the diffracted beam from the grating normal imposes important design considerations. It dictates the power efficiency, and the amount of angular dispersion. The quasi-Littrow angle of incidence affords the best efficiency. This refers to the central wavelength diffracting along the same angle to the normal as that of the incident beam so that $\alpha = \beta$ as shown in figure 4. A slight difference in height in the plane parallel to the grating lines is imparted to enable the beams to be separated out spatially. Although often small this causes conical diffraction which hinders alignment and causes the pixels not to see equal amounts of the frequency components. It is of no consequence to the re-collimation of the beam since it is exactly matched upon leaving the SLM. Both designs (b) and (c) utilise this design feature.

The design in figure 5 was adopted for the work presented in this thesis. It has the advantage that the components lie upon an optical axis enabling ease of alignment[20]. The incident beam is not quite in quasi-Littrow configuration but only 6° away from it causing a approximately 5 % decrease in efficiency as calculated from power

measurements. The diffracted beam is in the same plane as the incident beam eliminating any spherical diffraction. A folding mirror was used to reflect the diffracting beam over the grating which helped reduce the space taken up on the laser table. All the optics used lie on an optical line which aids the alignment significantly. The alignment procedure will be described in section 4.3. A cylindrical mirror collimates the diffracted beam so that the FWHM is incident on the central quarter of the SLM array which corresponds to a length of 16 mm. Diffracting the FWHM of the pulse over only a quarter of the SLM allows for information in the wings of the pulse to be shaped. The foot print of the pulse shaper including optical component assemblies is 820 x 320 mm.

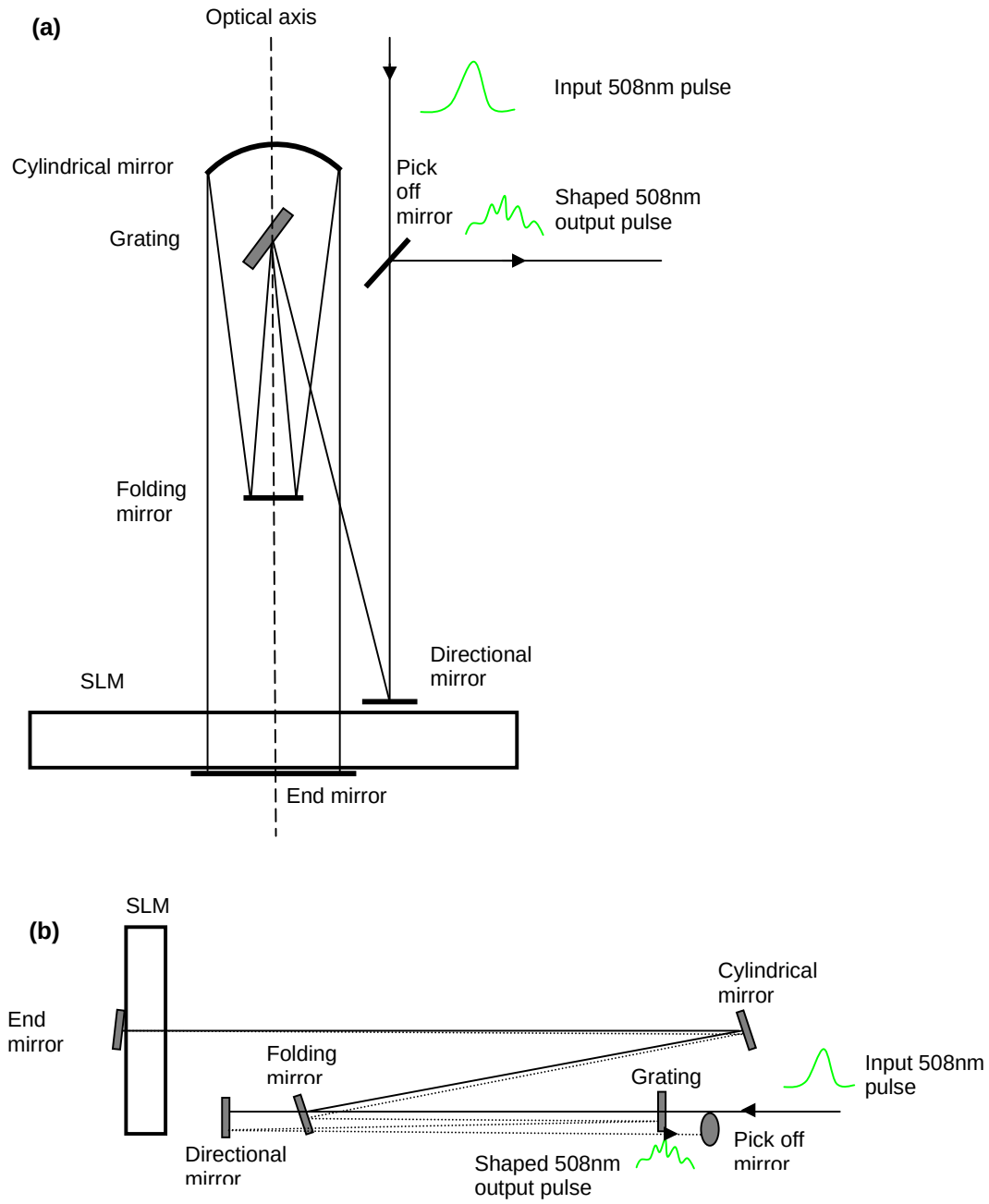

Figure 5: View of the pulse shaper from the top (a) and the side (b). The incident beam is reflected off the directional mirror to give an angle of incidence into the grating of 44º. The diffracted beam is folded into the cylindrical mirror without major off axis errors. The cylindrical mirror reflects and collimates the beam over the grating and mirror into the SLM and onto the retro reflecting mirror which reflects the beam back along the same path with a slight angle in such a way that the beam propagates under the input beam. The pick off mirror picks the beam off and directs it to the frequency doubling set-up. The optical axis marks the path of the 508 nm component of the pulse and is used in the alignment, section 4.3. (b) Side view of the pulse shaper lay out. The input beam is plotted with the full line and the output with the dotted line.

4.2.2 Grating

The length, *f*, is determined by how far the beam needs to propagate to diffract the FWHM of the spectrum over a quarter of the SLM (i.e. 16 mm). The amount by which the beam is diffracted is determined by the number of grooves/mm on the grating. The length, *f*, corresponding to the focal length must not be too long since there is limited room on the laser table. Also it can not be too small since the angles between the component assemblies will be too large and therefore cause aberrations.

$$m\lambda = d(\sin\alpha + \sin\beta) \tag{4.3}$$

The grating equation[40] (equation 4.3) delivers the angle of diffraction β for a particular wavelength, λ, depending on the angle of incidence, α, and groove spacing of the diffraction grating, d. The groove spacing corresponds to the distance between thin lengths of the same reflective material on the grating surface. When the geometrical path length of the light between the grooves is equivalent to the wavelength of light, constructive interference occurs yielding a wavefront of surfaces of constant phase. The angle of incidence is the angle to the normal of the grating. m relates to the order of diffraction, the zeroth order (m = 0) being a direct reflection; generally m = 1 is the most efficient and is used in our set-up.

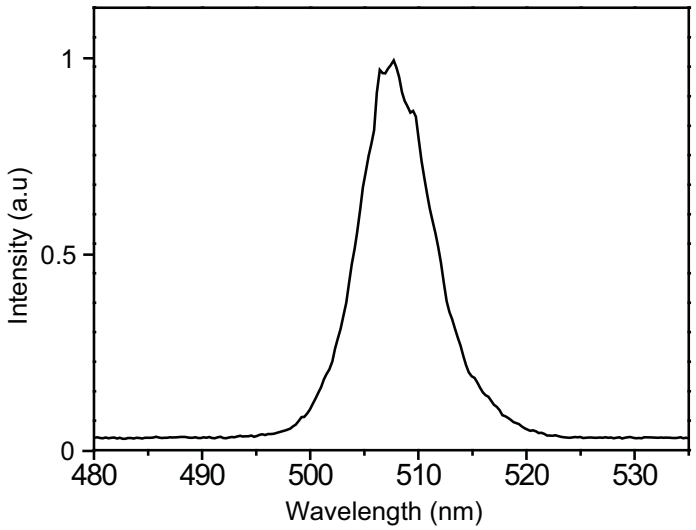

Figure 6: Spectrum of the input pulse centred at 508 nm. A FWHM of ~9.5 nm is measured indicating the bandwidth of a 40 fs pulse.

The grating equation was used to calculate the number of grooves needed on the grating and the length required to diffract the FWHM of the beam over 16 mm (central 25% of the SLM). The bandwidth of the transform limited pulse was calculated assuming a 40 fs pulse – this is an upper limit on the bandwidth. With centering at 508 nm the FWHM of the pulse runs from 503.3 nm to 512.8 nm yielding a bandwidth of 9.5 nm. This was confirmed by a spectrometer reading as illustrated in figure 6. Calculations were performed assuming that the two wavelengths of the FWHM were input into two grating equations to yield a distance *f*. The groove density, *G,* was taken as from commercially available values, where $G = 1 / d$. α was fed into the equations to give two angles of β. The trigonometric relationship between tan of half the angular difference between the two values of β and the opposite length of half of 16 mm was used to give the required value of *f*. The cylindrical mirror was made with the angle of curvature equal to the focal distance *f* as illustrated in figure 7.

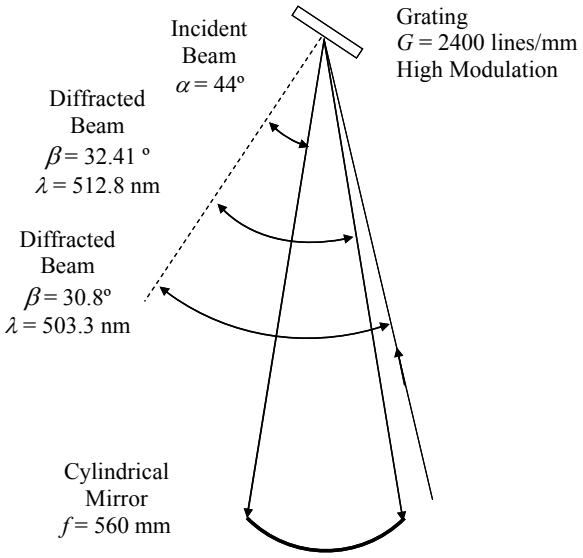

Figure 7: Schematic of the grating showing the angles of incidence and diffraction for the wavelengths corresponding to the edges of the FWHM. The incident beam is at an angle of $\alpha = 44^o$, for a wavelength of 503.3 nm which gives $\beta = 30.8^o$ and for a wavelength of 512.8 nm gives an angle of diffraction, $\beta = 32.41^o$. The focal length of the cylindrical mirror was determined to be the length needed for the distance between the two wavelengths to be 16mm, approximately one quarter of the SLM. The focal length of the cylindrical mirror was determined to be 560 mm.

With an angle of incidence of 44º and a value of *G* set to be 2400 it was found that *f* needed to be 560 mm in order to spread the wavelengths of the FWHM of the pulse by 16 mm. The linearly dispersed pulse has 0.06 nm of wavelength difference between each pixel (pixel width of 102 μm) with 488.631 nm incident on pixel 0 and 527.369 nm incident on pixel 639 (total 640 pixels). With approximately a 6π phase shift applied by

each pixel this set-up affords a maximum shaping time window of approximately 5 ps as calculated by $1/\Delta\nu$.

4.2.3 Optical components and alignment assemblies

The 4*f* zero dispersion compressor set-up consists of 5 optical components each of which requires different forms of precision alignment. The directional mirror used to direct beams into and out of the 4*f* line was a 1" anti-reflection coated optic (CVI AR2) whose centre of reflection lay at 500 nm, and was housed in a standard mirror mount with x and y axis alignment using micrometer screws. Since the grating required a high groove density 2400 lines/mm a holographic grating was used. Holographic gratings are made using the interference fringe pattern between two laser beams to etch into a polished photo resist coated substrate. This technique has the advantage over ruled gratings that there are very few ghosts or imperfections in the grating lines. However since the groove profile is sinousoidal there is no blazing angle, reducing over all efficiency. The grating does perform as well as a ruled grating at the quasi-Littrow angle. The grating was glued onto a custom made aluminium back plate with feet enabling it to be fixed to the top of a 2D tilt mount. The tilt mount was designed similarly to a standard mirror mount but bigger, 100 x 100 mm, and in this case laid flat enabling front and back tilt and side to side tilt. The tilt mount was fixed to a 40 mm high aluminium block used to raise the grating to the appropriate height and mounted upon a 360˚ rotation stage. The whole assembly was bolted to the laser table so the optical line was traversing through its centre and the centre of rotation of the rotation stage as illustrated in figure 8 (a).

The folding mirror had visible high energy 0° angle of incidence coating (CVI AR2) and was 50 mm wide, 20 mm high and 10 mm deep. The optic was gripped in a custom made aluminium bracket with 7 PTFE screws to hold the optic tightly in place. The bracket was fixed on top of a 1D tilt stage enabling forward and backward tilt, so the pivot of tilt was below the mirror face. The tilt stage was connected to a rotation mount so the axis of rotation was around the centre of the mirror. The rotation stage was in turn mounted onto a mechanical translation stage enabling a movement of 50 mm. The translation stage was

mounted on a custom made base plate which in turn was fixed to the laser table so that it ran with its centre on the optical line as illustrated in figure 8 (b).

The cylindrical mirror was held in a similar bracket to the folding mirror with its back face mounted onto a 2D tilt stage. The tilt stage was fixed vertically onto a 1" diameter optics post held by a post holder mounted on a translation stage enabling 1D movement of 50 mm. The translation stage was fixed to a base plate and placed with the optical line running through its centre as illustrated in figure 8 (c).

The SLM had two base plates attached to the bottom, with care taken not to block the ventilation holes; it was bolted to the table using optics clamps. The end mirror was held in a bracket and was 100 mm wide and 20 mm high with a thickness of 10 mm and 0° incidence visible high energy coating (CVI AR2). Similarly to the cylindrical mirror it was attached to a 2D tilt stage in the vertical position held on a 1" optics post which in turn was held by an optics post holder attached to a translation stage. The translation stage allowed a movement of 50 mm and was attached to the laser table with the optical line traversing through its centre as illustrated in figure 8 (d).

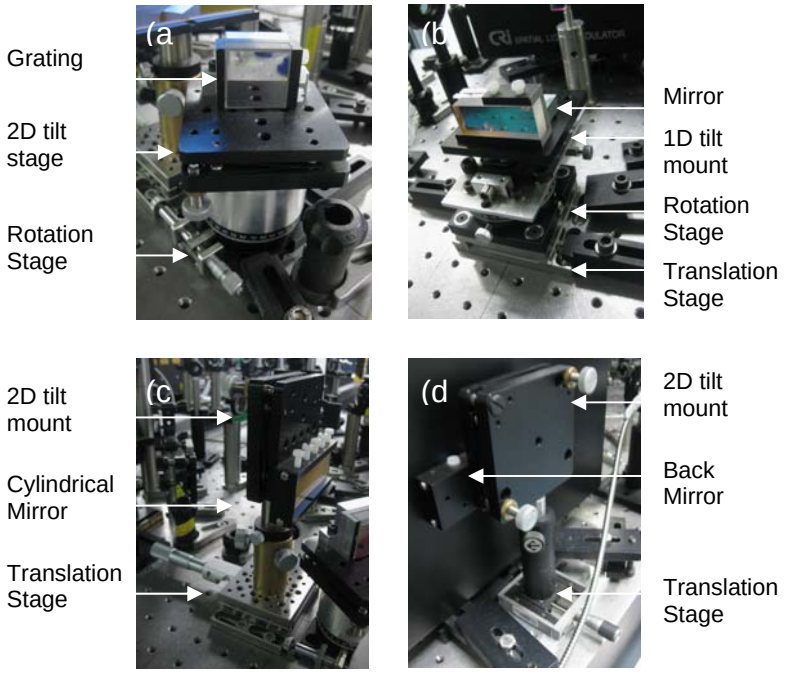

Figure 8: Optical component assemblies in order of use. (a) Grating assembly has a rotation stage and 2D tilt stage. (b) Folding mirror assembly has a 1D tilt stage, rotation and translation stage. (c) Cylindrical mirror assembly uses a 2D tilt stage upon a 1D translation stage. (d) Back mirror assemble uses 2D tilt stage and a translation

4.3 Alignment procedure

Precise alignment of the pulse shaping set-up is crucial to its effectiveness. The pulse shaping apparatus was built on a flat vibration damped optics table surrounded by perspex that allowed it to be sealed off from any disruptive air currents in the laboratory. Below the alignment procedure used is described:

4.3.1 Initial component placement and frequency domain adjustment

(1) The OPA output of 508 nm 'P' polarised light was reflected by 45º onto a mirror directing the beam on to the grating centre at an angle of approx 30º. The beam was kept parallel to the table by using a movable, just before the mirror and just before the grating.
(2) The zeroth order reflection of the grating was checked to see if the grating face was perpendicular to the laser table. The same movable iris was used and any angle changes were made using the 2D tilt stage that the grating was fixed on.
(3) The beam was aimed at the centre of the grating where the axis of rotation was located. An iris was then fixed in front of the grating.
(4) To check the grating lines were perpendicular to the table, the line of diffraction was allowed to propagate ~1 m and was checked to be parallel to the laser table. The tilt stage controls on the grating mount were used for any adjustments.
(5) The grating assembly was rotated so that the 508 nm frequency component travelled along the central line of the set-up. A line was drawn onto the laser table and the optical component assemblies were fixed in place so that their centres were in line with it, referred to as the optical line. A custom made beam block with a slit 1 mm wide in its face running from top to bottom was placed on top of the optical line so that the wavelength of the diffracted beam propagated through it. The spectrometer was used to observe the wavelength running along the optical line and the grating rotated until 508 nm was found.
(6) The folding mirror was now placed into the correct position. The slit was used on the optical line to obtain the central wavelength of 508 nm in the same fashion as

described above. The height of the reflected beam was measured at the point where the cylindrical mirror was to be placed.

(7) The cylindrical mirror was placed onto its adjustment assembly and again the slit used to obtain the central wavelength on the optical line. The height of the beam was measured to ensure that it ran parallel with the table.

(8) The end mirror was placed into its position and adjusted so that the reflected beam can be seen reflecting of the grating. The spot was placed so that it is around 8 mm below the incoming beam allowing for it to be easily picked of down stream.

(9) A pick off mirror was placed in the beam line. Its height was adjusted for the incoming beam to pass over it while capturing the outgoing beam. The tilt of the back mirror and the height of this mirror were altered to achieve the least difference in height from the incoming and outgoing beams while capturing the entire outgoing beam.

(10) The spectrum of the outgoing beam was checked against that of the incoming beam.

4.3.2 Time domain adjustment

(1) The output of the OPA before the pulse shaper was directed into an autocorrelator. The beam was reflected off a glass slide to attenuate the beam to 7 % of its initial power which stopped any damage to the nonlinear crystal. The FWHM was recorded and adjustments to the OPA were undertaken to reduce it.

(2) The glass slide was removed to allow the beam to propagate through the SLM. A mirror was placed into the output path to direct the beam into the autocorrelator where the FWHM could be monitored.

(3) The pulse length was optimised by adjusting the two lengths of f in the set-up. The folding mirror translation stage was adjusted first, then the cylindrical mirror translation stage. The FWHM could be seen changing with these adjustments, a value most similar to the beam prior to the SLM was aimed for. The distances between the components were recorded and the end mirrors position adjusted so that it was equivalent to the focal length of the cylindrical mirror.

(4) By adjusting, *f*, the direction of the beam path could have changed. This manifested itself as a FWHM of the output pulse being longer than the input pulse. In which case the alignment procedure would need to be re-done starting from point (5) in the frequency domain alignment, assuming the input beam had been successfully aligned on the grating. If the FWHM of the input and output pulses are matched then correct alignment can be assumed.

The autocorrelation measurement before the pulse shaper is shown in figure 9 (a), with a FWHM of 144 fs corresponding to a pulse duration of ~100 fs. Figure 9 (b) illustrates an autocorrelation of a temporally stretched pulse before the time domain adjustment procedure in red. The output pulse after a full alignment is shown by the plot in black with an autocorrelation similar to that of the input pulse.

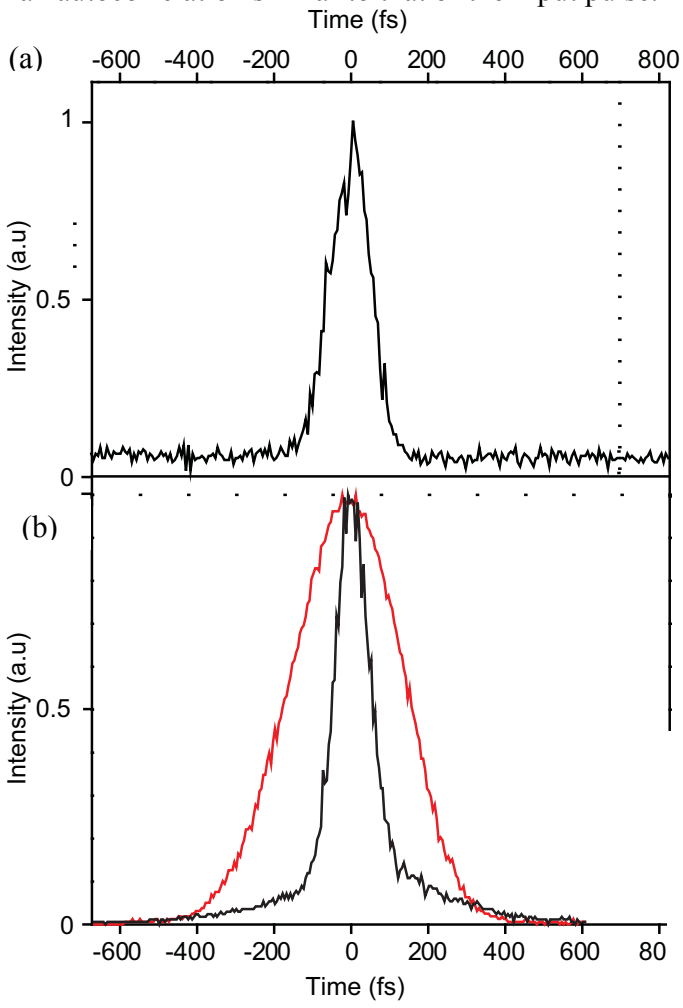

Figure 9: Typical autocorrelation traces. (a) Autocorrelation of the 508 nm input pulse before the pulse shaping apparatus. (b) Autocorrelation of a temporally stretched pulse before applying the time domain adjustment (red) and after (black).

4.4 Spatial light modulator calibration

4.4.1 Liquid crystal array

The liquid crystal spatial light modulator (CRI-640-VN-D) is made up of 2 arrays of 640 individually addressable pixels that are fixed directly opposite each other and separated by 102 μm, figure 4.5. Each pixel has a width of 100 μm and is spaced by 2 μm, each pixel is 5 mm tall and the whole array spans 64 mm. The dual array liquid crystal has a ~94% transmission at 508 nm and the surfaces have an anti reflection coating for the visible wavelength range with an 8% loss. Therefore, at 508 nm the total maximum efficiency if the SLM on double-passing is ~50 % as calculated from power measurements. The glass plates sandwiching the liquid crystal between them are made from indium tin oxide (ITO) which is electrically conductive as well as optically transparent. Each plate acts as an electrode through which a potential difference can be achieved across the liquid crystal of each pixel.

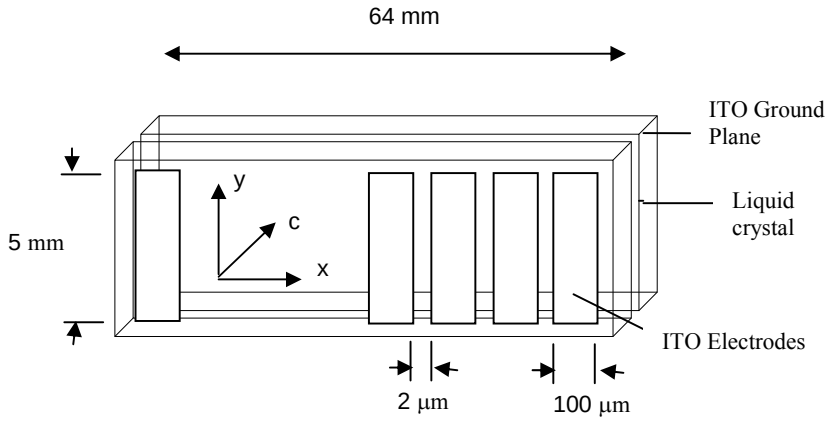

Figure 10: Schematic of the dual liquid crystal array. Showing interpixel spacing, pixel width, pixel height and pixel orientation relative to the axes. Array height and width are shown. ITO electrodes, which are transmissive sandwich a nematic liquid crystal. Each electrode addresses a liquid crystal crystal. The liquid crystal is aligned along the y axis with no voltage applied and re-aligns along the c axis with applied voltage, the re-alignment causes the alteration of the polarisation into the axes of the liquid crystals.

The liquid crystal (LC) used in spatial light modulators falls in the category of a twisted nematic crystal[21]. The molecules each have a charge at either end and when a voltage is applied across the pixel the molecules become twisted by electrostatic forces into a helical structure. The LC molecules lie parallel to each other and the *y* axis, all facing the

same direction as illustrated in figure 10. When a voltage is applied across the pixel the molecules rotate so they are aligned along the *c* axis, this causes an increase in refractive index along this axis but not any other. The change in refractive index imparts a phase shift $\Delta\varphi$ onto the light passing through it. With a broad bandwidth pulse dispersed over many pixels a phase can be imparted onto the pulse. Depending on the orientation of the *y* axis the twisted liquid crystal has the property of rotating the polarisation of light passing through it. With more voltage, more twist is developed, and so a greater index of refraction as well as a rotation of the polarisation.

4.4.2 Shaping with spatial light modulator

In the case of a single array LC-SLM, phase only pulse shaping is achieved as shown in figure 11 (a). The tilt axis is aligned parallel to the polarisation of the input light field. Amplitude modulation pulse shaping with one array is achieved by having the *c* axis at 45° to the input electric field polarisation; however, a phase modulation coupled to the amplitude modulation is always imparted onto the pulse. For pulse shaping simultaneously of the amplitude and phase the two liquid crystal arrays can be used in concert. They are aligned at +45º and -45º to the polarisation of the input light field, as shown in figure 11 (b).

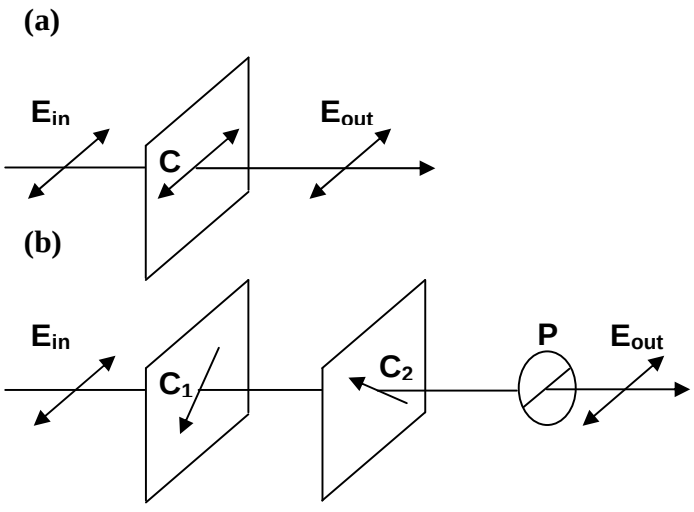

Figure 11: Diagram of polarisations in pulse shaping. (a) Polarisations of a phase only pulse shaper. The polarisation of the laser field is represented by the double headed arrow. The input pulse E_{in} passes through the modulation device represented by the square. The imparted polarisation by the device is shown by C which yields the output pulse E_{out}. (b) Polarisations of a phase and amplitude pulse shaper. The input pulse E_{in} has horizontal polarisation, the modulation devices C_1 and C_2 induce cross polarisations in the transmitted electric field so that phase modulation can be applied. The phase shift is calculated as the sum of the polarisation vectors. The difference in the polarisation vectors which amounts to a non horizontal polarisation component is cut out by the polariser P.

Mathematically, the modulation of the vectors of the input light field by the LC arrays can be described using Jones matrices[28]. In the following description of phase and amplitude shaping the shift of the absolute phase due to the interpixel spacing of the SLM is not taken into account. The input light field vector, E_{in}, modulation device, $M(\Delta\varphi)$, polariser, P_x, and rotation matrices, $R(\theta)$ are given by:

$$E_{in} = \begin{pmatrix} 1 \\ 0 \end{pmatrix}$$

$$P_x = \begin{pmatrix} 1 & 0 \\ 0 & 0 \end{pmatrix}$$

$$M(\Delta\varphi) = \begin{pmatrix} \exp(\Delta\varphi) & 0 \\ 0 & 1 \end{pmatrix}$$

$$R(\theta) = \begin{pmatrix} \cos\theta & \sin\theta \\ -\sin\theta & \cos\theta \end{pmatrix} \tag{4.4}$$

The matrix $M(\Delta\varphi)$ is written in its own coordinate system relative to its c axis. A rotation matrix $R(\theta)$ is used to transform between the *x*-*y* and the LC coordinate systems. In the case of the phase only pulse shaper:

$$E_{out} = M(\Delta\varphi)E_{in}\begin{pmatrix} \exp(i\Delta\varphi) \\ 0 \end{pmatrix} \tag{4.5}$$

In this case the polarisation of the output field is not affected by the change in refractive index imparted by the modulation device since they have the same vector. In the case of the dual array system:

$$E_{out} = P_x R(\pi/4)M(\Delta\varphi_2)R(-\pi/2)M(\Delta\varphi_1)R(\pi/4)E_{in} \tag{4.6}$$

Substituting in the matrices as shown in equation 4.4, gives:

$$E_{out} = \exp(i[\Delta\varphi_1 + \Delta\varphi_2]/2\begin{pmatrix}\cos([\Delta\varphi_1 - \Delta\varphi_2]) \\ 0\end{pmatrix} \tag{4.7}$$

What can be seen here is that the amplitude imparted onto the electric light field is due to the difference between $\Delta\varphi_1$ and $\Delta\varphi_2$. This can be thought of as one vector, C_1, as becoming dominant and so turning the overall vector out of the horizontal direction. The portion of light with its polarisation altered in the C_1 axis direction is filtered out by the polariser. The phase modulation of the electric light field is due to the sum of $\Delta\varphi_1$ and $\Delta\varphi_2$. Here the polarisation vector imparted by C_1 and C_2 are equal and opposite, so there is no overall change, however, there is in the case of its refractive index which gives the phase shift.

4.4.3 SLM electronics architecture

The SLM arrays 640 pixels each have a gray-level range of 4096 drive levels[41]. The drive levels are communicated to the pixels in the SLM by a voltage, V_i, where i is the pixel element.

$$V_i = V_{ref}\frac{D_i}{4096} \tag{4.8}$$

Where, V_{ref} is the reference voltage of 10.000 V and D_i is the digital level corresponding to that element. To prevent electromigration effects, the transport of materials under the influence of a field, in the liquid crystal the voltage supplied is ac rather than dc, since the rotation of the liquid crystal depends on the amplitude not the sign of the voltage. Each drive signal consists of a variable amplitude bipolar square wave typically operating at a few hundred hertz.

4.4.4 Calibration of phase and transmission modulation

The procedure for calibration of a dual array system of liquid crystals aligned with opposing polarisation rotations is non trivial. The SLM was set-up as illustrated in figure 11 (b), but with an extra polariser in front of the SLM to ensure the purest horizontal polarisation possible of the input light field. A helium-neon (HeNe) laser with a central wavelength of 633 nm was set to propagate through the pulse shaping apparatus and a power meter positioned to measure the power of the output beam. The retardance of both arrays is given by:

$$R_{net} = R_1 - R_2 \tag{4.9}$$

The overall retardance, R_{net}, experienced by the light is the difference between the first and second arrays, R_1 and R_2 respectively. The normalised transmission, T, of the SLM using a polariser as described in figure 4.4.2 (b) is:

$$T = \frac{I}{I_{\max}} = \cos^2\left(\frac{\pi[R_{net}]}{\lambda}\right) = \cos^2\left(\frac{\pi[R_1 - R_2]}{\lambda}\right) \tag{4.10}$$

The transmission is measured with the power meter as intensity, I, over the maximum intensity, I_{max}. The overall retardance of the system is related to the transmission by including the wavelength, λ. The phase modulation is determined by the average value of the retardances:

$$\phi = \frac{2\pi\left(\frac{[R_1 + R_2]}{2}\right)}{\lambda} \tag{4.11}$$

This can be simplified to:

$$\phi = \frac{\pi(R_1 + R_2)}{\lambda} \tag{4.12}$$

The second array is driven to maximal voltage and the first array is incremented through the entire range of its 4096 voltage steps, the resulting power is measured at each level. This process was automated using a Labview program. The resulting power data was normalised to obtain the transmission as a function of the voltage, $T(V_1)$. Using the above equation for T, $R_1(V)$ is calculated except for an unknown constant corresponding to $R_2(V=V_{max})$. The same procedure is followed for the second array, with its voltage incremented as the first array is kept at maximum voltage to obtain $T(V_2)$. From this data $R_2(V)$ is calculated except for the unknown constant corresponding to $R_1(V=V_{max})$. The phase, ϕ, of the modulated beam depends on $R_1 + R_2$, equation 4.12, while the transmission depends on $R_1 - R_2$, as shown in equation 4.10. A fixed optical offset of ϕ is realised due to $R_1 - R_2$ term but this is of no consequence to the control of the relative phase of the frequency components. This entails that one of the unknown terms can be set to equal 0, $R_2(V=V_{max}) = 0$. The unknown constants directly effect the transmission term $R_1 - R_2$. To eliminate this problem, the constants are amalgamated into one constant.

$$dR = R_1(V = V_{\max}) - R_2(V = V_{\max}) \tag{4.13}$$

The two arrays exhibit an inherent overall retardance which is made of the contributions from each array that corresponds to the two unknown constants. dR is the apparent retardance of the combined system when both SLM arrays are driven to maximum voltage. This value is simply added to the R_1 (V) table already obtained and a complete calibration is made. Figure 12 illustrates the functions R_1 (V) and R_2 (V) as obtained from the calibration procedure. They are plotted as transmission against drive count:

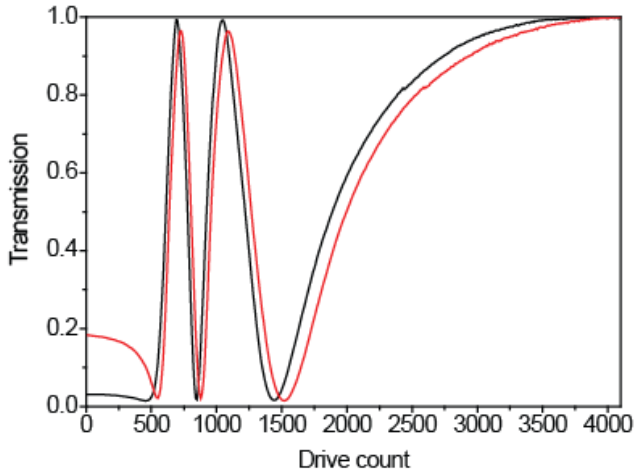

Figure 12: Plot of wrapped phase shift against drive count for mask A (black) and B (dotted red). (c) Plot of unwrapped phase shift against drive count for mask A (black) and B (dotted red).

The transmission data was converted to two functions of retardance against drive count using equation 4.10. The retardance was calculated as a phase shift (nm) which the light experiences by a set of drive counts. In this case the phase shift is related to 633 nm light. The retardance against drive count is subsequently unwrapped to give the functions shown in figure 13. The calibration was performed in a single pass configuration. In order to use the same calibration in the double pass geometry a factor of two must be applied.

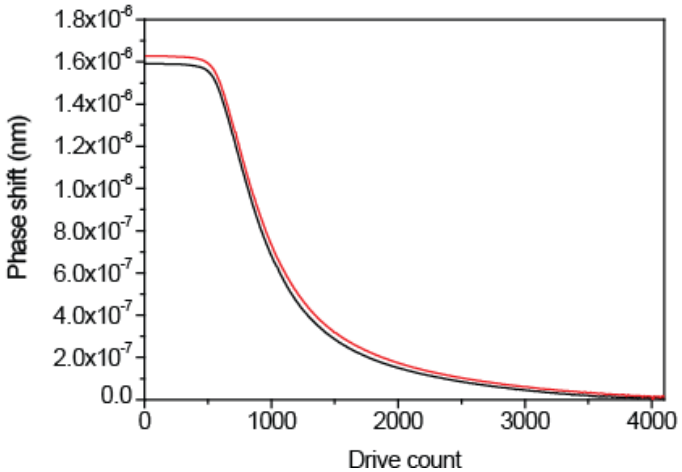

Figure 13: Plot of unwrapped phase shift against drive count for mask A (black) and B (red).

4.4.5 Scaling by wavelength

Once the calibration had been completed, equations 4.10 and 4.11 were used within a Labview program to obtain the retardance values $R_1(V)$ and $R_2(V)$ for a desired modulation function. The retardance values were scaled for the correct wavelength. The retardance against drive count function obtained in the calibration was for 633 nm, to use this data at another wavelength it must be scaled appropriately.

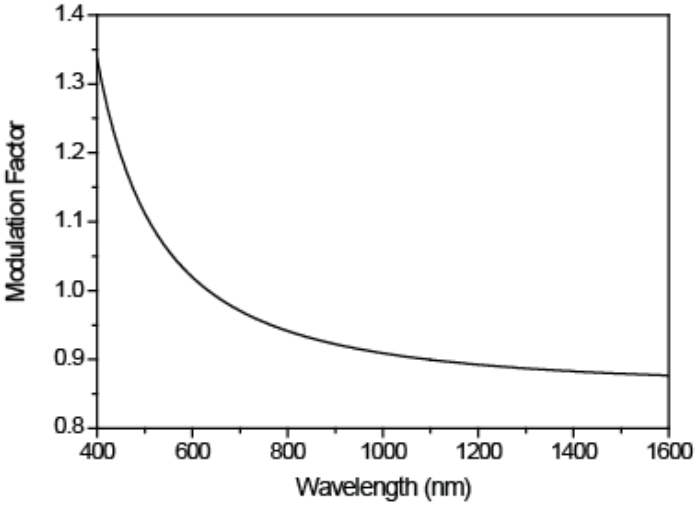

Figure 14: Plot of the modulation factor against wavelength (nm). Calibration is performed at 633 nm, the output of a HeNe, the calibration can be converted to other wavelengths using the appropriate modulation factor. The modulation factor for 633 nm is therefore 1.

Figure 14 shows the wavelength calibration function that was supplied by the manufacturers. It is possible to create your own wavelength calibration but has not been done here since the difference is known to be negligible[29].From this graph the set of wavelength calibration factors for the wavelength corresponding to each of the pixels were obtained. To scale the wavelength accordingly the calculated retardance is simply divided by the set of wavelength factors. The arrays of scaled retardances were used to find the relevant drive counts from the 633 nm calibration graph of retardance against drive count.

4.4.6 Spectral dispersion

The calibration of phase and transmission against drive count of each pixel is dependent on the wavelength, λ, propagating through it. So in order to accurately program the phase and transmission of a pixel, the exact wavelength incident on it must be known. Once the

4*f* alignment was complete the SLM itself was used to calculate spectral dispersion. First, a mask was applied to the SLM with a maximum transmission on half the array and no transmission over the other half. The spectrum of the output beam was observed and the SLM placed into the appropriate position so that the cut off in the spectrum lay at approximately 508 nm. This gave an approximate wavelength of 508 nm for the 320th pixel. A second mask was applied with a phase shift of π on every other 10 pixels to the SLM to give a "comb" shape in phase. This creates a comb in intensity of the spectrum due to the destructive interference of the out of phase components at each junction of π and 0 phase shift. The spectral analyser was used to record the wavelength at each peak of the spectrum. Around 13 wavelength points were enough to create an accurate linear equation which was used to interpolate around the recorded data and calculate the wavelength at each pixel. The wavelength at each pixel was theoretically calculated using equation (4.3) to program the initial masks in the spectral dispersion calibration.

4.4.7 The effects of a pixellated modulator

Generally when shaping in the frequency domain a smooth function in the phase and amplitude is desired. Unfortunately SLM's create a pixelated analog to the smooth functions due to the array of finite width rectangular pixels used to mimic the desired mathematical function in the Fourier plane. This is best shown in the figure 15.

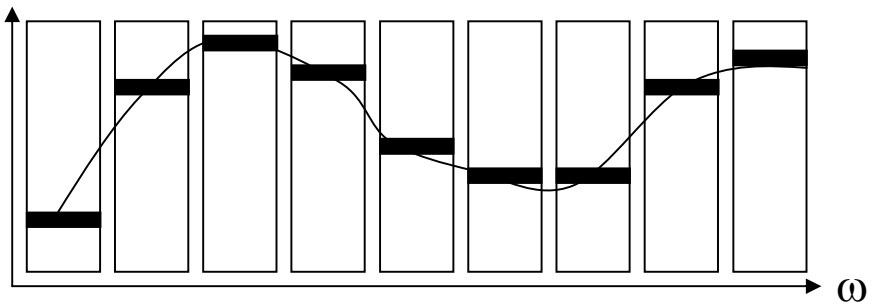

Figure 15: Arbitrary waveform plotted as a function of frequency with pixels superimposed. The finite size of the pixels within a SLM means the actual analog waveform can not be completely replicated causing pulse replicas.

In the following discussion, the properties of an output waveform from a pixelated amplitude and phase modulation device are analysed. A square function, *squ(x)* is used to describe each pixel and is defined as:

$$squ(x) = 1 \quad |x| \leq ½$$
$$= 0 \quad |x| > ½ \tag{4.14}$$

Interpixel spacing has not been taken into account here. The modulation applied by the SLM as a function of position can be described by[28]:

$$M(x) = \sum_{n=-N/2}^{N/2-1} squ\left(\frac{x - x_n}{\Delta x}\right) A_n \exp(i\phi_n) \tag{4.15}$$

Where $M(x)$ is the sum of the modulation functions for each pixel, which are, A_n amplitude modulation and ϕ_n phase modulation each over the distance Δx and centred at the position x_n. N is the number of sharply defined pixels. Since the beam has a finite width at the focus of the lens, equation (4.15) needs to be modified to account for this. Assuming a Gaussian spatial beam profile with a *1/e* width D, then at the focal plane the beam profile is $\delta x = 4\pi F/\lambda D$. By convolving the focal plane spatial profile with the modulation function and assuming a Gaussian spatial profile with width δx, the modulation function becomes[28]:

$$M(x) = \exp\left(\frac{-x^2}{\delta x^2}\right) \otimes \sum_{n=-N/2}^{N/2-1} squ\left(\frac{x - x_n}{\Delta x}\right) A_n \exp(i\phi_n) \tag{4.16}$$

The spatial modulation function above can be converted to a spectral modulation function after assuming the spectral components are diffracted linearly with respect to frequency by the 4*f* set-up[28]. This assumption aids in the analysis in this case but is not ubiquitous.

$$M(x) = \exp\left(\frac{-(v - v_o)^2}{\delta v^2}\right) \otimes \sum_{n=-N/2}^{N/2-1} squ\left(\frac{v - v_n}{\Delta v}\right) A_n \exp(i\phi_n) \tag{4.17}$$

Here δx in the spectral plane is converted to, δv, a spectral width. If we further assume a transform limited pulse, giving a flat spectral phase, the pulse can be represented by a sum of spectral amplitudes B_n:

$$E_{in}(v) \approx \sum_{n=-N/2}^{N/2-1} squ\left(\frac{v-v_n}{\Delta v}\right) B_n \tag{4.18}$$

Substituting equation (4.18) into equation (4.17) gives the output pulse in terms of square segments of defined frequencies[28]:

$$E_{out}(v) = \exp\left(\frac{-(v-v_o)^2}{\delta v^2}\right) \otimes \sum_{n=-N/2}^{N/2-1} squ\left(\frac{v-v_n}{\Delta v}\right) A_n B_n \exp(i\phi_n) \tag{4.19}$$

By inverse Fourier transforming the above equation the temporal response for a pixelated pulse shaping apparatus (without interpixel spacing) is obtained[28]:

$$E_{out}(t) \propto \exp(-\pi^2 \delta v^2 t^2) \sin c(\pi \Delta v t) \times \sum_{n=-N/2}^{N/2-1} A_n B_n \exp\left[i(2\pi v_n t + \phi_n)\right] \tag{4.20}$$

The Gaussian term on the right comes from the finite spot size of the input beam on the grating and is inversely proportional to it. The *sinc* term arises from the Fourier transform of the square function from the pixels rectangular shape where the width of the *sinc* function is inversely proportional to the pixel separation Δv. The summation is a Fourier series of the amplitudes and phases of the frequency components v_n and describes the basic properties of the pulse.

4.4.8 Pulse replicas

The effect of having a Fourier series in the time domain with evenly spaced frequency samples is that the pulse shape repeats itself with a period of the reciprocal of the frequency increment, 1/Δν. The Gaussian-sinc term suppresses replicas far from time

zero and at or near the nodes of the sinc function. Sampling replicas degrade the overall signal quality and there is little that can be done by the SLM alone to diminish them. In this study we use nonlinear effects (second harmonic generation) after the shaped pulse to up convert it to the UV domain. Nonlinear effects act as a squared on the amplitude resulting in small amplitudes being reduced and becoming negligible compared to the overall signal.

4.4.9 Complexity, time window and spot size

The output electric field is a convolution of both the mask function, *M(t)* and the electric field of the light pulse, equation (4.2). The time window with which the SLM can operate is specified by the frequency range over each pixel, ω, whereas the time window in which the SLM can operate is determined by the 4*f* set-up. The time window in this case is proportional to the number of grating lines illuminated by the input beam multiplied by the period of an optical cycle[28]:

$$T = \frac{2\sqrt{\ln 2}\omega_{in}\lambda}{cd\cos\theta_{in}} \tag{4.21}$$

Where ω_{in} is the input beam radius before the grating, c is the speed of light, d is the grating period, λ is the central wavelength and θ_{in} is the input angle of the beam onto the grating. In the set-up described a beam radius of 3 mm is used in conjunction with an input angle of 44º, which allows a time window of 25 ps for a 40 fs pulse. This relationship also gives a limit of complexity which is defined by[28]:

$$\eta = \frac{\Delta\lambda}{\lambda}\frac{\pi}{(\ln 2)^{1/2}}\frac{\omega_{in}}{d\cos(\theta_{in})} \tag{4.22}$$

Where, $\Delta\lambda$ is the bandwidth (in units of wavelength). This affords a complexity of 644. With shorter pulse lengths and, or, larger input beam diameters, higher complexities are possible. The spectral resolution is also determined by the input beam diameter. The spot

size of individual spectral components should be the same size or smaller than the size of a pixel in the LC array. For the central wavelength, assuming near Littrow diffraction, the spot size is[28]:

$$\text{Spot size} = 4 \ln (2) \frac{f\lambda_0}{\pi w} \tag{4.23}$$

Where w is the width of the input beam and f is the focal length. The spectral plane spot width will be, at best 84 μm, which is less than 100 μm pixel width.

4.4.10 Second harmonic generation

Once the ultra-short pulse centred in the visible has been shaped its electric field is up converted to the ultra violet (UV) region using a non-linear process. In the case of SHG type I and assuming a thin crystal, and hence also phase matching over the complete bandwidth and a non-depleted fundamental electric field, E_{f}, the second harmonic field, E_{SHG}, is expressed as,

$$E_{\mathrm{SHG}}(t) \propto E_{\mathrm{f}}{}^{2}(t) \tag{4.24}$$

In the frequency domain the electric field is convoluted with itself to give the upconverted field:

$$E_{\mathrm{SHG}}(\omega_{\mathrm{SHG}}) \propto \int E_{\mathrm{f}}(\omega_{\mathrm{f}}) E_{\mathrm{f}}(\omega_{\mathrm{SHG}} - \omega_{\mathrm{f}}) \mathrm{d}\omega_{\mathrm{f}} \tag{4.25}$$

Where ω_{SHG} refers to the frequency of the second harmonic generation and ω_{f} refers to the frequency of the fundamental.

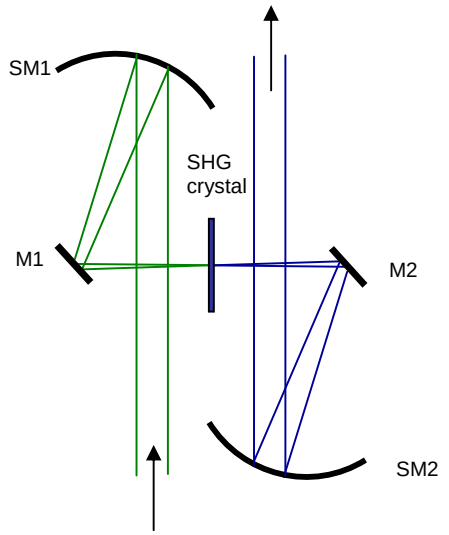

Figure 16: Schematic of SHG optical layout. A visible pulse (shaped) propagates to the spherical focusing optic SM1 which focuses the beam onto the SHG crystal by being folding the beam using mirror M1. The path of the UV generation is mirrored using optics suitable for UV reflection to afford a collimated UV laser beam. No filtering of the visible is required since the UV optics have a very low reflectivity in the visible.

Figure 16 depicts the optical layout used in SHG from a visible laser beam. The non linear crystal is made from beta-BaB_2O_4 (BBO) and is 100 μm in thickness. A spherical mirror (SM1) with a focal length of 15 cm was used to focus the beam into the SHG crystal. A second optically matched spherical mirror (SM2) was used to collimate the output beam. The use of small mirrors, M1 and M2, allow for a small difference as possible between the incident and reflected beam angle from the spherical mirrors which helped reduces optical aberrations. The SHG type I crystal, is rotated in all Cartesian coordinates to optimise phase matching in the pulse which is monitored by maximising the power of the SHG signal. Since the non linear process occurs in this set-up collinearly the fundamental and SHG beams have to be separated. Optics SM2 and M2 were coated for the UV wavelength range which is transparent in the visible region. After reflections from a further 4 such optics used for beam steering the residual visible light in the beam was negligible. Conversion efficiency is dependent on the pulse shape with maximum energy for an unshaped pulse of 2 μJ in the UV, which exceeds the demands of weak-field gas phase multiphoton excitation experiments in most organic molecules. Some bandwidth is lost in the SHG process, due to the non-negligible crystal thickness: the measured bandwidth of an unshaped pulse is reduced by a factor of 0.6 compared to the bandwidth calculated for SHG of the same pulse in a very thin crystal. The unshaped UV pulse centred at 254 nm is shown in figure 17.

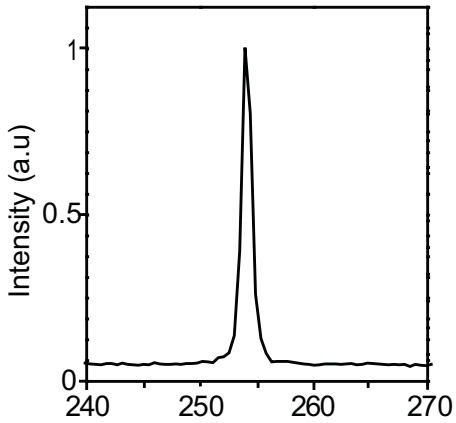

Figure 17: Spectrum of the unshaped pulse after second harmonic generation. This shows a bandwidth of ~1 nm, this is 0.6 of the expected bandwidth using the thin crystal limit.

4.5 Results

4.5.1 Computer controlled feedback optimisation

Coherent control schemes predominantly rely on a shaped pump waveform in order to dictate the ensuing excited state dynamics. The shape of the waveform can be created in two ways, either intuitively with prior knowledge of frequency resolved and time resolved spectroscopic information and *ab initio* calculations or through a feedback loop optimisation process using a genetic algorithm. The former technique requires detailed information about the potential energy surface under study. With this information there is also uncertainty about how much excess energy the molecule possesses in the ground state, and so upon ionisation where in the Franck Condon region the excited state wave packet is initiated. For polyatomic molecules with many degrees of freedom these small uncertainties can accumulate to a significant effect. To eliminate these uncertainties, Rabitz et al[22], proposed to use a genetic algorithm to generate the correct waveform for the desired final state of interest. This approach worked well for many systems[23-27]; however the approach has limitations. These are that although the final state was reached in the majority of cases and the photoproduct achieved, the waveform generated could give little or no information about the route taken over the potential energy surface. This was due to the complexity of the pulse shape generated by the genetic algorithm. The genetic algorithms were increasingly finding multiple solutions to the same problem.

Often the phase and amplitude profiles when Fourier transformed gave little information about which vibrational modes were responsible for the generated dynamics. At the onset of this experiment our aim was to incorporate both approaches to coherent control. Our aim was to use prior knowledge of the system gained from *ab initio* and dynamics calculations, pump probe experiments and high resolution spectroscopy to create a control scheme and then to use a genetic algorithm to optimise the process within a boundary. Although the restricted control scheme was not implemented in this work, the frame work for it to do so in the future exists and shall be described below.

4.5.2 Evolutionary Strategy

An elitist evolutionary strategy (ES) with adaptive mutation, $(\mu + \lambda)$ - ES was used as the optimisation algorithm, the code was written by Burbidge and follows procedures as set out in reference 23. This type of evolutionary strategy mimics Darwinian evolution hence the name and is global in its search, similarly to genetic algorithms. Firstly, a random initial population, λ, of 16 individuals, each with 1280 values, 640 for each liquid crystal array, is generated as a seed to the algorithm, which could also be a good guess pulse shape in later usage. The population is evaluated; in this case the values from the SHG measurement are used to generate the fitness for each individual as described above. From the initial population, λ, the best 4 parents, μ, are selected from which the mutants will be generated. Each mutant is generated by mutation from two parents, ρ, selected uniformly at random from the best μ pulses. The mutation adds an independent Gaussian perturbation to each dimension. This is done until a new population of 16 individuals is generated. Every 320 mutations, the ES counts how many were successful if more than 1 were successful, then the mutation strength is divided by 0.707 (i.e. increased). If less than 1 were successful, then the mutation strength is multiplied by 1 (i.e. decreased). In this experiment, ρ is set to 2, so it is not possible to determine whether or not mutations are successful hence, η is set to 1.0 and the mutation strength is multiplied by 0.707 every 320 mutations. Since there are 16 mutations every generation, the mutation strength will be decreased every 20 generations. The 4 parents and 16 mutants compile the next generation. This results in an over-valuation of the parent in noisy environments, but also

guarantees convergence. The evolutionary strategy then starts the cycle again and is run for 600 generations or until stopped externally.

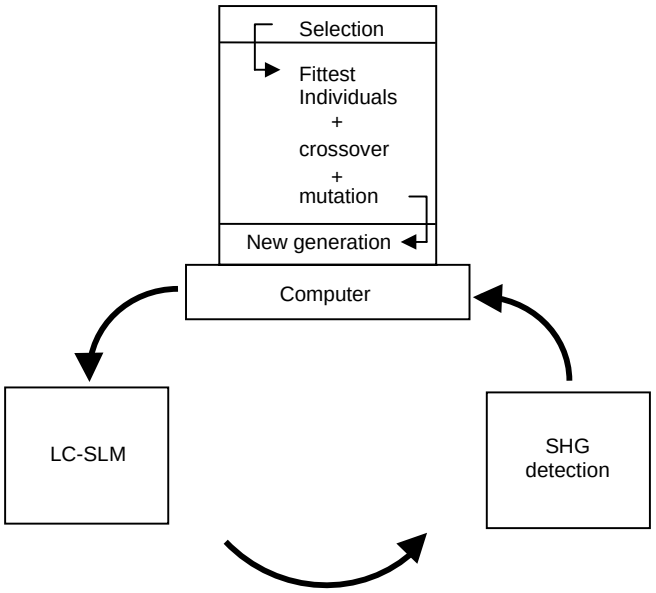

Figure 18: Schematic of feedback controlled SHG maximisation using an evolutionary strategy. A random seed pulse initiates the cycle, where by the power of SHG is measured of the shaped pulse. The fitness function is generated determines its survival out of a population. A new population is generated with characteristics of the fitness pulse shapes. The cycle carries on selecting and refining the best pulse shapes.

4.5.3 Optimisation of SHG

An optimisation algorithm was used to shape a pulse to increase second harmonic generation in a BBO crystal. This type of optimisation is a popular starting point for optimisation algorithms owing to it being a well known phenomenon[1]. The experimental set-up utilised two power meters to determine the fitness function. A power meter measured the power of the zero order diffraction from the grating which gave a reading for the unmodulated laser pulse and was used to monitor shot to shot variations in the power. The pulse shaper output, centred at 508 nm was focused into the BBO crystal as in the set-up described in section 4.4.10. The UV beam generated was measured with the final power meter. Within a Labview program the power of the fundamental beam was divided by the square of the SHG beam to provide the fitness. If the fitness was below zero a random number was generated. The program fed an external optimisation algorithm with the fitness which in turn generated a pair of 640 value drive counts between 0 and 4095. These were sent to the SLM directly resulting in both phase and

amplitude modulation. The algorithm was run as a blind optimisation to give a fixed hypothesis search space of $[0, 4095]^{1280}$. The fitness function obtained after 390 generation is shown below in figure 19. The function shows a characteristic steep ascent in fitness as it optimises an initial random pulse shape. The algorithm then levels of to a constant fitness.

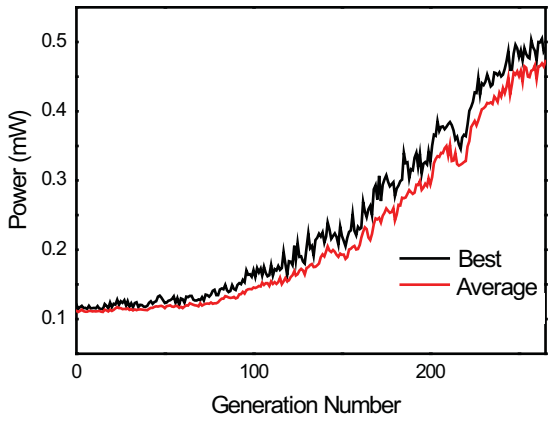

Figure 19: Blind optimisation of SHG in a BBO crystal. Both arrays of 640 pixels each with 4096 values were used by an evolutionary strategy to optimise a pulse shape. The second harmonic generation of the visible from the pulse shaping set-up was optimised by the algorithm by measuring the power generated.

4.5.4 Phase comb

To illustrate the capability of our pulse shaping setup we chose several useful phase modulations to generate pulse trains at varying times and wavelengths. For weak field coherent control experiments, the types of pulse shapes that are likely to be necessary are trains of pulses with the same wavelength but carefully timed to cause optimal constructive or destructive interference, or trains of different wavelengths to excite different modes at well-defined time-intervals.

Pulse replicas in the time domain can be produced by applying a π phase 'comb' to the pulse in the frequency domain, this is achieved by producing alternating groups of pixels with 0 and π phase respectively. Figure 20 shows four such pulse replicas with pulse separations, τ, of (a) 530 fs, (b) 760 fs, (c) 1600 fs, and (d) 2230 fs produced by comb

spoke widths of 21, 15, 7 and 5 pixels respectively. The raw XFROG traces can be seen in the bottom row of fig. 20, above them is the time domain electric field intensity (black) and phase (red) and at the top of the figure, the spectral electric field intensity (black) and phase (red).

The comb phase function causes holes, due to interference, in the spectrum at the points where the phase changes abruptly, and the overall result is a squared-comb spectrum. In the frequency domain this corresponds to a set of pulse replicas, composed of two main central peaks and outer satellite peaks, all equally spaced.

The spectral square-comb is smoothed by the doubling process (equation 4.25) and thus the set of pulse replicas becomes a pulse pair, with the smaller outer pulses reduced to less than 5 % of the intensity of the main pulses. In our data we are able to observe the outer small satellite peaks in some of the data, for example, in figure 20 (a) (ii) a sub pulse at 1.1 ps is clearly visible. The measured pulse separation times, τ, allow us to calibrate the wavelengths on the SLM pixels using the uncertainty principle relationship, $\tau = 1/P$, where P is the width of the programmed comb spoke on the SLM, P, in units of frequency, so that the comb widths on the SLM are 1.62, 1.13, 0.54 and 0.39 nm across the comb spokes for figure 20 (a)-(d) respectively. This provides an accurate measurement of the angular dispersion in the pulse shaper. The other points to note are that the temporal phase is flat, and the temporal duration of each of the replicas is similar. The spectral phase is linear over each of the "teeth" in the spectral comb. This is predicted by equation 4.25, from which it can be seen that the convolution of the spectral electric field produces a new field with a phase that is independent of the SLM modulation, because the modulation factor $e^{i\pi}$ is a real number.

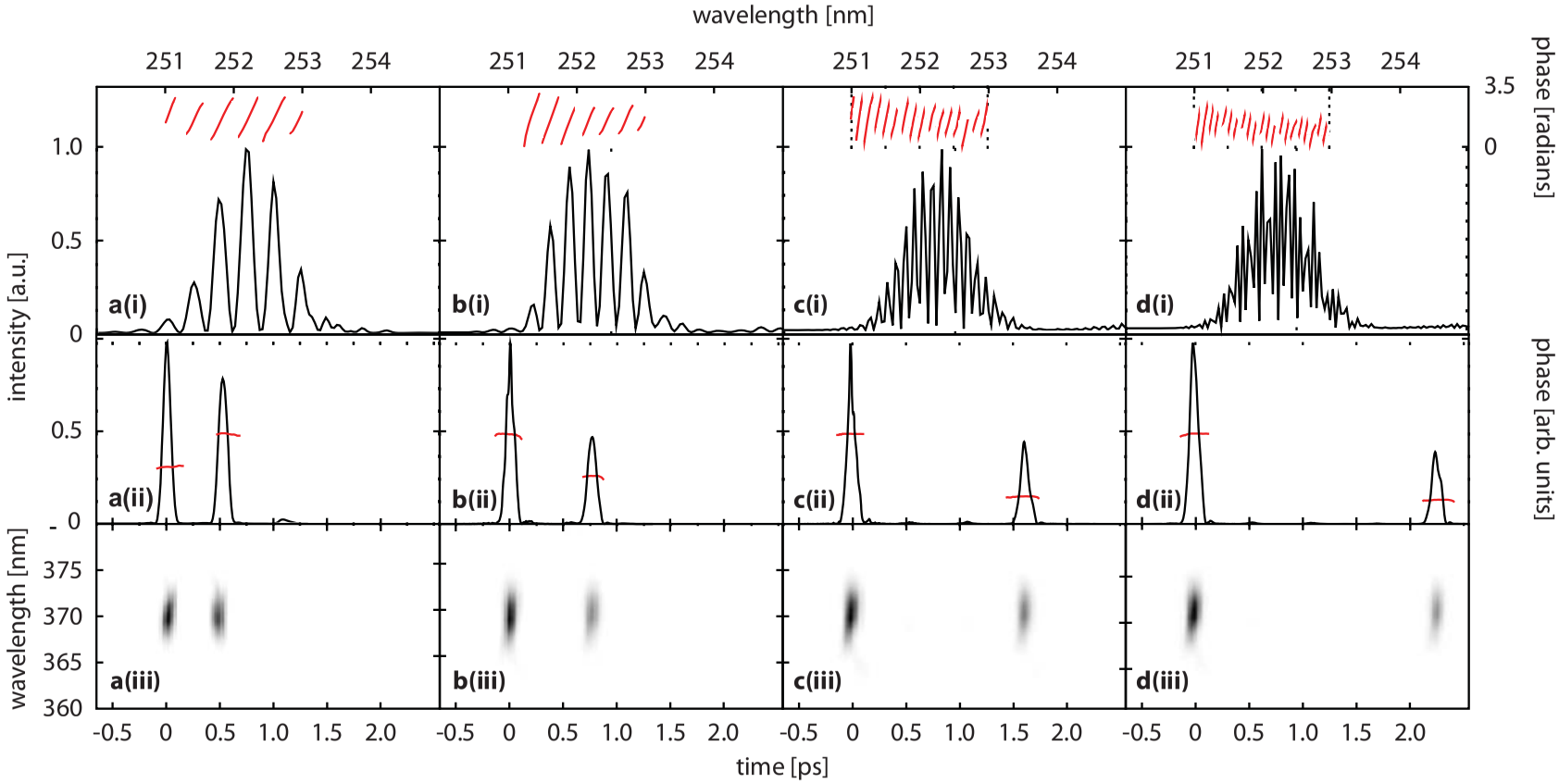

Figure 20: Pairs of pulses in the time domain generated from combs of alternating 0 and π phase. Each figure shows a raw XFROG trace (iii), the reconstructed temporal electric field intensity of the UV pulse (black) and phase (red) (ii) and reconstructed spectral intensity (black) and phase (red) (i) of the UV pulse

4.5.5 Triangular phase

In another scheme (figure 21), we created a pair of pulses with different central frequencies by applying a triangular phase mask to the SLM (figure 21 (a)). The results are shown in figure 21 (b)-(d). The raw XFROG traces can be seen in figure 21 (d), the time domain electric field intensity (black) and phase (red) are in 21 (b), and the spectral electric field intensity (black) and phase (red) are in 21 (c). The temporal separation of the pulses is determined by the difference in the group delays, τ_g, of the two pulses, which is defined by the difference in slopes of the two applied linear spectral phases: $\tau_g = -d\phi(\omega)/d\omega$. The two peaks are separated by 650 fs in the time domain (b). The pulse at 650 fs has a central wavelength 253.6 nm and is separated from the larger peak at 254.6 nm by 1 nm (c). The retrieved electric field of these two pulses are also shown in fig. 21. The retrieved spectral phase shows a clear change in slope at the central frequency of the spectrum, 254 nm, as programmed on the pulse shaper at the fundamental frequency, 508 nm. The frequency doubling process was most efficient at a slightly off-centred wavelength, around 254.6 nm, and thus the retrieved temporal intensity profile shows a bias towards the sub-pulse at this wavelength. This means that the upconverted spectrum is centred at 254.6 nm, and the retrieval algorithm has centred the retrieved electric field at the central wavelength and time of the stronger sub-pulse in the trace. Hence the slope of one of the spectral phases in the retrieved electric field is flat, corresponding to zero time delay, and one of the temporal phases of the two sub-pulses is flat, corresponding to zero wavelength shift from the new centre wavelength, 254.6 nm; thus, the spectral and temporal phases of the other sub-pulse show increases in the magnitude of the slope (larger group delay and spectral shifts, respectively), as would be expected. The time separation of the two pulses is predicted by the SLM phase mask function and the measured spectral dispersion as 665 fs. This is 15 fs greater than the observed experimental value, a discrepancy that is well within the error of the experiment.

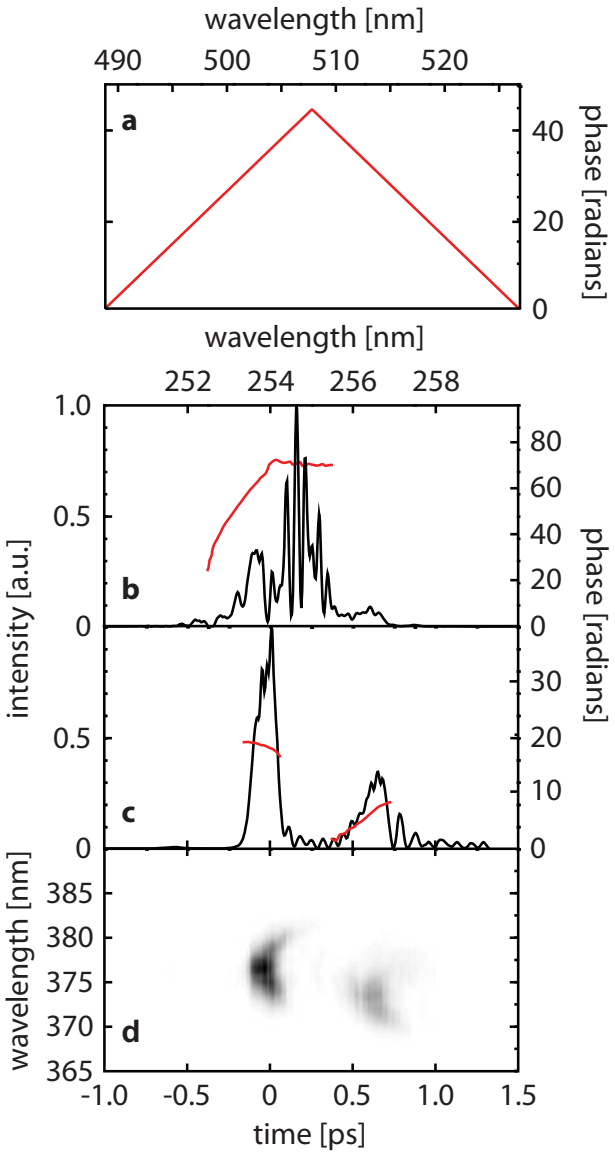

Figure 21: Pairs of pulses with different central wavelengths generated from a triangular phase mask. (a) Triangular phase mask applied by the SLM in the visible. (b) Spectral intensity (black) and phase (red) showing the central wavelengths of the UV pulses. (c) Time domain electric field intensity (black) and phase (red) of the UV pulse, showing two distinct subpulses. (d) Raw XFROG trace.

4.5.6 Sinusoidal phase

In the final scheme, shown in figure 22, a sine wave phase function is applied to the SLM, of amplitude 4, and 34 oscillations across the 640 pixels. The number of oscillations of the sine wave defines the temporal separation of the peaks in the pulse

train produced. The amplitude of the phase modulation determines the relative heights of the pulse train peaks. Here five pulses at -610 fs, 0 fs, 610 fs (very faint), 1220 fs and 1830 fs are produced, as shown in fig. 22. The raw XFROG traces are shown in 22 (c), above them is the time domain electric field intensity (black) and phase (red) and at the top of the figure, in (22 (a)), the spectral electric field intensity (black) and phase (red), in (22 (b)). In the time domain each peak has a Gaussian profile with a flat phase over each peak. The spectral phase shows a regular oscillatory structure, with several large jumps most likely due to the non-zero spectral intensity.

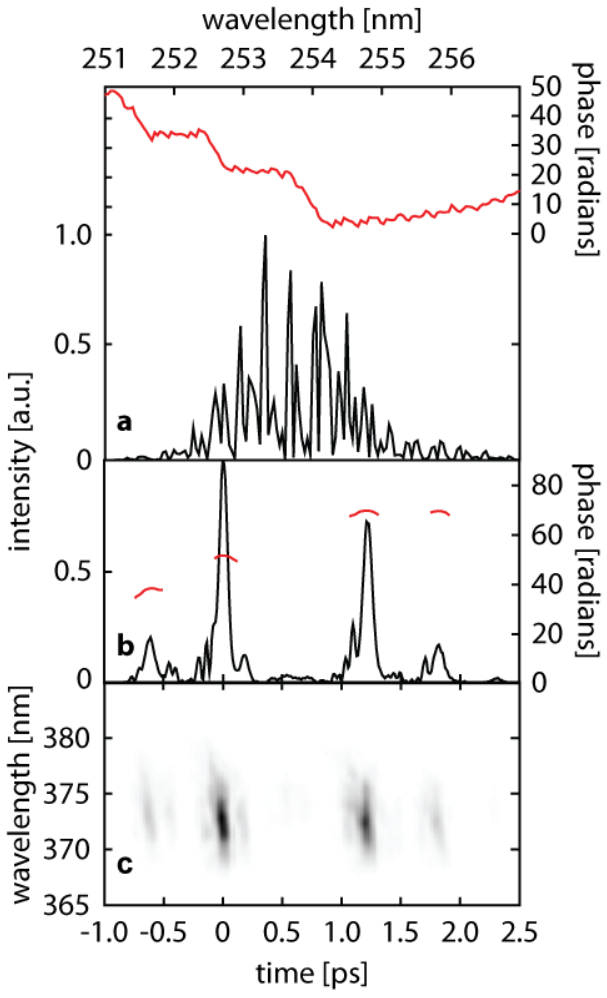

Figure 22: Pulse trains in the time domain generated from a sinusoidal phase mask. (a) The spectral phase (red) and intensity (black) of UV pulse. (b) Temporal electric field intensity (black) and phase (red) of the UV pulse. (c) Raw XFROG trace.

4.6 Conclusion

These results demonstrate that shaped light in the deep UV may be generated effectively by frequency doubling the output of a folded 4*f* SLM setup. Shaping the output of an OPA allows for the central frequency of the shaped UV pulse to be tuned, which is particularly beneficial to coherent control experiments, where the photon energies are of significance as well as their relative phases and amplitudes. The details of the pulse shapes required are not always *a priori* knowledge, but often require feedback from an experiment, and hence the utility of flexible SLM pulse shaping.

Changing the wavelength of the shaped UV pulses to 243 nm from 254 nm can be achieved easily by tuning the central wavelength from the OPA to 486 nm. With a change in wavelength, the only alterations to the shaping setup that are required are a slight adjustment to the grating angle to match the cylindrical mirrors and changing the BBO crystal angle to maximise the output signal.

Our results show several pulse shapes produced in the UV with varying pulse separations and central frequencies. Interestingly, the full characterisations and retrieved XFROG traces highlight that phase information is being transferred in all the pulse shapes presented through the type I SHG process. To investigate this effect further XFROG traces of the beam in the visible, before the SHG process, as well as afterwards would directly record the effect of upconversion on the spectral phase within a type I SHG process. Although we have not shown it here, our experimental setup could easily be adapted by adding a genetic algorithm with feedback from the spectrogram to achieve the exact pulse shape desired, irrespective of phase distortions in the input pulse or alignment. The closely spaced sequences of pulses centred at different central wavelengths should prove a valuable tool for controlling the nuclear dynamics of the excited electronic states of photochemical species.

4.7 References

1 A. Assion, T. Baumert, M. Bergt, T. Brixner, B. Kiefer, V. Seyfried, M. Strehle and G. Gerber, *Science*, 1998, **282**, 919-922.
2 R. J. Levis, G. M. Menkir and H. Rabitz, *Science*, 2001, **292**, 709-713.
3 M. Hacker, G. Stobrawa, R. Sauerbrey, T. Buckup, M. Motzkus, M. Wildenhain and A. Gehner, *Applied Physics B-Lasers and Optics*, 2003, **76**, 711-714.
4 B. J. Pearson, J. L. White, T. C. Weinacht and P. H. Bucksbaum, *Physical Review A*, 2001, **6306**.
5 F. Verluise, V. Laude, Z. Cheng, C. Spielmann and P. Tournois, *Optics Letters*, 2000, **25**, 575-577.
6 A. Monmayrant, A. Arbouet, B. Girard, B. Chatel, A. Barman, B. J. Whitaker and D. Kaplan, *Applied Physics B-Lasers and Optics*, 2005, **81**, 177-180.
7 K. Hazu, T. Sekikawa and M. Yamashita, *Optics Letters*, 2007, **32**, 3318-3320.
8 P. Nuernberger, G. Vogt, R. Selle, S. Fechner, T. Brixner and G. Gerber, *Applied Physics B-Lasers and Optics*, 2007, **88**, 519-526.
9 M. Hacker, R. Netz, M. Roth, G. Stobrawa, T. Feurer and R. Sauerbrey, *Applied Physics B-Lasers and Optics*, 2001, **73**, 273-277.
10 S. Shimizu, Y. Nabekawa, M. Obara and K. Midorikawa, *Optics Express*, 2005, **13**, 6345-6353.
11 C. Schriever, S. Lochbrunner, M. Optiz and E. Riedle, *Optics Letters*, 2006, **31**, 543-545.
12 M. Hacker, T. Feurer, R. Sauerbrey, T. Lucza and G. Szabo, *Journal of the Optical Society of America B-Optical Physics*, 2001, **18**, 866-871.
13 H. F. Wang and A. M. Weiner, *Ieee Journal of Quantum Electronics*, 2004, **40**, 937-945.
14 A. M. Weiner, *Review of Scientific Instruments*, 2000, **71**, 1929-1960.
15 A. M. Weiner, J. P. Heritage and E. M. Kirschner, *Journal of the Optical Society of America B-Optical Physics*, 1988, **5**, 1563-1572.
16 C. Froehly, B. Colombeau and M. Vampouille, *Progress in Optics*, 1983, **20**, 65-153.
17 M. Renard, R. Chaux, B. Lavorel and O. Faucher, *Optics Express*, 2004, **12**, 473-482.
18 A. Prakelt, M. Wollenhaupt, A. Assion, C. Horn, C. Sarpe-Tudoran, M. Winter and T. Baumert, *Review of Scientific Instruments*, 2003, **74**, 4950-4953.
19 T. Suzuki, *Annual Review of Physical Chemistry*, 2006, **57**, 555-592.
20 A. Monmayrant and B. Chatel, *Review of Scientific Instruments*, 2004, **75**, 2668-2671.
21 C. H. Gooch and H. A. Tarry, *Journal of Physics D-Applied Physics*, 1975, **8**, 1575-1584.
22 R. S. Judson and H. Rabitz, *Physical Review Letters*, 1992, **68**, 1500-1503.
23 D. Zeidler, S. Frey, K. L. Kompa and M. Motzkus, *Physical Review A*, 2001, **64**, art. no.-023420.
24 T. Hornung, R. Meier, D. Zeidler, K. L. Kompa, D. Proch and M. Motzkus, *Applied Physics B-Lasers and Optics*, 2000, **71**, 277-284.

25 T. Hornung, M. Motzkus and R. de Vivie-Riedle, *Journal of Chemical Physics*, 2001, **115**, 3105-3111.
26 C. Daniel, J. Full, L. Gonzalez, C. Lupulescu, J. Manz, A. Merli, S. Vajda and L. Woste, *Science*, 2003, **299**, 536-539.
27 N. H. Damrauer, C. Dietl, G. Krampert, S. H. Lee, K. H. Jung and G. Gerber, *European Physical Journal D*, 2002, **20**, 71-76.
28. Vaughan, J. Ultrafast pulse shaping. *www.physics.gatech.edu/frog/UFOBook/13-Ultrafast-Pulse-Shaping-Vaughan.pdf*
29. Mirkin, L. Cambridge research and instrumentation inc. *Private communication*.

.

Chapter 5

Summary and outlook

The molecular dynamics undertaken by benzene at the onset of channel 3 have been found to involve a movement of the wave packet to the triplet state on ultrafast time scales. A brief summary of this experiment is made as well as that of the development of the pulse shaping capability in which arbitrarily shaped pulses in phase and amplitude were obtained in the UV and fully characterised. We then move onto the outlook available from these experiments, which naturally sees the use of the pulse shaper in controlling excited state benzene.

5.1 Summary

5.1.1 Ultrafast intersystem crossing in benzenes channel 3 region

The ultrafast energy dissipation in benzene above 3000 cm^{-1} in the first excited state has been assigned to a multitude of decay mechanisms none of which have been satisfactorily confirmed. By using time resolved photoelectron spectroscopy in the gas phase we have been able to monitor decay dynamics of the excited state wave packet in this region of the spectrum. A simple decay scan of the total photoelectron signal as a function of time with two different wavelength probes yielded biexponential decays with differing total photoelectron counts. By scanning the probe wavelength between these regions a step function at 250 nm was found which illustrated a new ionization channel opening up with the higher energy probes. The difference in photoelectron counts between the high and low energy probe was concluded to hold information about the excited state processes that the low energy probe was not sensitive to. Further investigation of the total photoelectron signal due to the low energy probe found that by removing the biexponential decay component an oscillation with a period of 1.2 ps became visible.

Energy dispersed photoelectron spectra at 100 fs intervals were collected with both the high and low energy probes. Both TRPES plots showed no distinct features appearing or disappearing, which ruled out the possibility of photoisomerisation in that region. The TRPES of the high energy probe was analysed in box cars of photoelectron energy and 4 distinct features were observed. At high photoelectron energies two oscillations with a period of 1.2 ps were found which were in phase with that observed on the decay scan of the low energy probe. The oscillations were separated by 0.11 eV which corresponds to the breathing mode of benzene. In the middle energy region an oscillation was found with the same 1.2 ps period but out of phase. The two oscillations indicated that an excited state wave packet was being observed at either turning point of its oscillation. A fourth feature was found in the low energy photoelectrons, which showed a rise in photoelectron count after 600 fs.

The results fit the picture that the excited state wave packet moves to the triplet state, in 600 fs, most likely through an intersystem crossing in the prefulvene region of the

potential energy surface. An increased coupling constant between S_1 and T_2 ($^3E_{1u}$) has been found in this area by *ab initio* calculations. The T_2 ($^3E_{1u}$) state acts as a doorway state and couples strongly to T_1, which acts as a dense bath state, dissipating out the energy to a high number of vibrational states in that energy region. Part of the wave packet, however, does not couple well to the T_1 state and oscillates back and forth between the doorway state, T_2, and the excited state, S_1. The portion of the excited state wave packet that does couple to T_1 is monitored by the photoelectrons with low energy. It shows an increase in signal after 600 fs, the time it takes for the wave packet to access T_1. The remaining wave packet that does couple well with T_1 is monitored at its outer turning point of its oscillation in the photoelectrons with middle energy, and at the inner turning point of its oscillation by the two bands with high photoelectron energies. The initial 30 % of the photoelectron total decay was rationalised to be as a result of internal conversion, since the higher energy probe could not see this population after its decay, which energetically implies movement to the ground state.

The decay time is 240 fs which is on the time scale consistent with a conical intersection[1]. Calculations have found that a conical intersection exists in the prefulvene region of the potential energy surface in the same region as the proposed triplet singlet crossing. The internal conversion cannot however be counted as the dominant mechanism since 70 % of the wave packet is found to still be on the excited state surface which does decay but at much slower decay times of 1.7 ns. The mechanism was confirmed by calculations using the CASPT2 method by our collaborators. The observed ultrafast intersystem crossing in a hydrocarbon challenges the established rules of thumb that intersystem crossings do not exist with strong enough coupling to allow fast population transfer. Ultrafast intersystem crossing is therefore expected to exist in hydrocarbons more abundantly than previously believed.

5.1.2 Frequency doubling shaped visible femtosecond pulses to access the UV

Most coherent control schemes in the weak field one photon limit require photons with energy corresponding to the ultraviolet region. Unfortunately, existing pulse shaping technology cannot shape UV pulses because high energy photons damage the modulation device. To overcome this barrier a number of techniques have been

developed to convert the shaped frequencies from where they are efficiently shaped in the infrared to the ultraviolet region.[2, 3]

Our approach to the generation of UV shaped pulses involved shaping the output of a wavelength tuneable OPA system in the visible region and then frequency doubling it in a second harmonic generation crystal. This represents the simplest frequency conversion technique, far simpler to realise experimentally than sum frequency generation. Shaping the output of an OPA system allows for simple tuning of the wavelength which provides the versatility to tune the energy of the shaped pulse for use in different coherent control experiments. The wavelength could be shifted from 254 nm down to 243 nm with minimal alignment of the pulse shaping device.

The pulse shaping device used was a 640 pixel dual array liquid crystal spatial light modulator, set–up in a folded geometry and operated in reflective mode. The geometry chosen offered the most efficient alignment procedure, utilising the central optical line which the optical component assemblies rested on and a slit for dispersion alignment. The reflective mode, although of less resolution offered the easiest alignment procedure due to only half the optics used over conventional single pass mode. The pulse shaper was calibrated and Labview programs written for its operation.

To test the apparatus a cross correlation frequency resolved optical gating (XFROG) technique was used to make measurements of the pulses simultaneously in time and frequency. This technique provides a full characterisation yielding both phase and amplitude information in both domains. A variety of pulse shapes were applied and observed: (i) a comb in phase affording pulse pairs, (ii) a sinusoidal phase shape affording a pulse train, and (iii) a triangular phase shape giving two sub pulses separated in time and frequency. All pulse shapes were modelled and fitted well. It was found that the phase comb was an effective way of measuring the angular dispersion of the pulse over the liquid crystal array, which is often a difficult measurement to make with any degree of accuracy. The triangular phase function represents the most interesting of the shapes applied to the pulse shaper. In a time domain perspective, the excited state wave packet could be thought of as being given kicks over the potential energy surface by sub pulses with different central

frequencies. This allows for an intuitive wave packet view of the excited state dynamics. With access to the deep UV and the prospect of easy wavelength tuneability as well as full characterisation techniques make this apparatus ideal for a range of coherent control applications.

5.2 Outlook

5.2.1 Molecular dynamics

The dynamics of benzene in the channel 3 region as described in chapter 3 could be further investigated. The same pump pulse and therefore same dynamics could be further scrutinised by using an even higher energy probe. Currently the laser system can produce pulses down to 235 nm, this range could be increased by using a series of non linear processes such as second harmonic generation to reach down to 200 nm. The higher energy probe would increase the viewing window of the reaction coordinate and it may give an indication of the fate of the ultrafast decay in the first few hundred femtoseconds that has been attributed to internal conversion.

A vacuum ultraviolet source is currently being developed in this group and would provide a tool to observe dynamics on the ground state. Energy resolution may be an issue due to the wave packet being vibrationally hot when the ground state is accessed from the excited state. It does posses the energy to ionise the ground state population in a 1 photon process.

The potential energy surface around the channel 3 region could be explored more extensively by changing the pump wave length in small increments and conducting the same experiments to see how the dynamics change. With reference to high resolution data on the states in the energy region, the modes which are important in the intersystem crossing and the internal conversion could be found. Although increasing the pump energy generally increases the decay rate it is known that the ultrafast decay is mode dependent and is thought to depend on out of plane modes.[4-8]

5.2.2 Coherent control of benzene

The investigation into the dynamics of benzene in the channel 3 region as described in chapter 3 have brought about a number of possible coherent control schemes. These can be designed to achieve a new or optimise an existing photochemical outcome or can be used to further study the dynamics observed.

A pump dump scheme could be implemented in which the wave packet would be dumped to the ground state at its outer turning point. The corresponding ground state geometry may either correspond to a benzene geometry or to that of an isomer of benzene. To experimentally verify the ground state structure either a multiphoton ionisation or a VUV source could be used to ionise the ground state population after the outer turning point is reached.

The excitation pump pulse could be scanned with a gap in it in order to find which modes specifically are responsible for movement of the wave packet to the triplet state or which are responsible for decay to the ground state via the S_1/S_0 conical intersection. This would be achieved by blocking out certain frequencies of the excitation pulse. The success of the pump pulse shape could be determined by measuring the decay profile, specifically the ultrafast decay constant for the internal conversion or oscillation amplitude probe with the 260 nm probe for the intersystem crossing. The dynamics observed in this fashion could also be altered using other pulse shapes. A triangular phase profile could be used to give ‘kicks’ to the wave packet over the potential energy surface to access either a internal conversion or intersystem crossing in a more intuitive time domain scheme.

Our theoretical collaborators have investigated increasing the yield of fulvene a photoproduct seen in photolysis experiments[6]. Figure 5.1 shows a control scheme based on their findings. They were able to identify the modes that were advantageous and disadvantageous to moving the excited state wave packet into the conical intersection in the prefulvene region with a specific trajectory to access the fulvene ground state minimum. The proposed mechanism which yields fulvene is shown at the top of the figure. It was found that the vibrational modes exist in a region of the spectrum accessible by our pulse shaping apparatus and only separated by 0.6 nm

which is within the bandwidth of the pump pulse. The figure illustrates the pulse bandwidths for an unshaped pulse and for a shaped pulse. The phase relationship between the two modes dictates the quantum yield of fulvene.

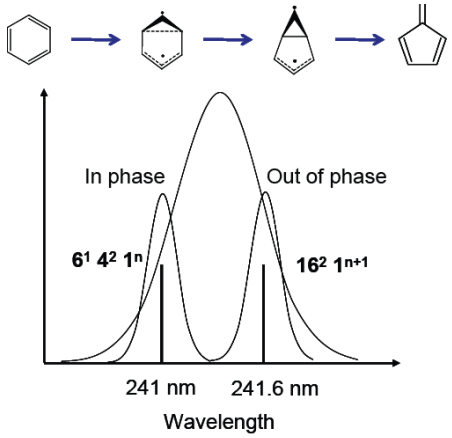

Figure 1: Diagram illustrating a control scheme proposed by our collaborators. The phase relationship between two frequencies could be manipulated in order to optimise the photochemical mechanism shown in the top of the figure. By altering the phase between the two modes shown the excited state wave packet will access the conical intersection with a specific trajectory to access the fulvene ground state minimum.

5.2.3 Investigation of pulse shape transfer in second harmonic generation

Although second harmonic generation is a widely used technique in many areas of science the phase transfer process for a shaped pulse is not yet fully understood. Currently there exist well made theoretical models that rely on convolution, which have been covered in chapter 2. These work well for documenting the spectral amplitude of the pulses with linear or quadratic phase profiles, where the phase shape can be seen to be transferred to the pulse in the new wavelength range[9]. With more complex pulse shapes such as cubic or sinusoidal phase profiles the spectral phase shape is seen to transfer to the spectral amplitude shape of the pulse[9].

Using the current pulse shaping and XFROG apparatus the phase transfer from the visible to the UV could be quantitatively investigated. This would be achieved by obtaining complete characterisations of the UV and visible pulses and comparing the phase profiles. Experimentally this can be realised by the addition of a flip mirror to direct the visible beam away from the UV pulse characterisation apparatus to that of a visible pulse characterisation apparatus. The path length of the visible would again need to be matched and directed into a nonlinear crystal cut to give an appropriate

signal from mixing of the visible pulse and the characterised infra red pulse. Knowledge of the phase effects of second harmonic generation in terms of spectral phase would complement the current knowledge of phase effects on spectral intensity.

5.3 References

1 S. Cogan, Y. Haas and S. Zilberg, *Journal of Photochemistry and Photobiology a-Chemistry*, 2007, **190**, 200-206.

2 C. Schriever, S. Lochbrunner, M. Optiz and E. Riedle, *Optics Letters*, 2006, **31**, 543-545.

3 P. Nuernberger, G. Vogt, R. Selle, S. Fechner, T. Brixner and G. Gerber, *Applied Physics B-Lasers and Optics*, 2007, **88**, 519-526.

4 D. Oconnor, M. Sumitani, Y. Takagi, N. Nakashima, K. Kamogawa, Y. Udagawa and K. Yoshihara, *Journal of Physical Chemistry*, 1983, **87**, 4848-4854.

5 M. Sumitani, D. V. Oconnor, Y. Takagi, N. Nakashima, K. Kamogawa, Y. Udagawa and K. Yoshihara, *Chemical Physics*, 1985, **93**, 359-371.

6 M. Sumitani, D. V. Oconnor, Y. Takagi and K. Yoshihara, *Chemical Physics Letters*, 1984, **108**, 11-13.

7 E. Riedle, H. J. Neusser and E. W. Schlag, *Faraday Discussions*, 1983, 387-394.

8 J. M. Smith, X. Zhang and J. L. Knee, *Journal of Physical Chemistry*, 1995, **99**, 1768-1775.

9 M. Hacker, R. Netz, M. Roth, G. Stobrawa, T. Feurer and R. Sauerbrey, *Applied Physics B-Lasers and Optics*, 2001, **73**, 273-277.